Integrated nanophotonic structures for mode conversion

mode coupling and filtering

By

Siamak Abbaslou

A dissertation submitted to the

School of Graduate Studies

Rutgers, The State University of New Jersey

In partial fulfilment of the requirements

For the degree of

Graduate Program in Electrical Engineering

Written under the direction of

Prof. Wei Jiang

And approved by

____

____

____

____

____

New Brunswick, New Jersey

October, 2017

ABSTRACT OF THE DISSERTATION

Integrated nanophotonic structures for mode conversion,

mode coupling and filtering

Dissertation Director:
Prof. Wei Jiang

Silicon, which is the second element of group IV of the periodic table, forms the backbone of the semiconductor industry, similar to how carbon is the pillar of the living world. Silicon processing has gradually become a mature technology in electronics industry. Therefore, the most economically viable way of achieving optoelectronic integration is to adopt the complementary metal oxide semiconductor (CMOS) infrastructure and use silicon technology for optical devices applications. Silicon photonics furnishes a great opportunity for reducing energy consumption in communication, at the same time resolving interconnect bandwidth density, which is becoming the performance bottleneck in integrated electronics.

A variety of fascinating physical phenomena and practical devices can be implemented by manipulating light in the nanoscale, where the decrease in waveguide dimension to subwavelength scale and precise refractive index engineering enable new

phenomena to emerge. However, the very first challenge of nanophotonic devices is coupling light in and out of a nanophotonic chip. Mode matched coupling devices are required to reduce the transmission losses between the optical fiber and the nanophotonic waveguides. We present a robust design for low loss, wide band grating coupler. The optimized fully etched two dimensional grating coupler can effectively couple the fundamental mode from a single mode silica optical fiber to a single mode silicon waveguide with 500-fold mode size difference. The device is fabricated through a single step E-beam lithography process on a silicon-on-insulator wafer. We characterize the mode converter device through the V-groove fiber array surface grating coupler measurement setup. The developed measurement setup and grating couplers serve as a platform to characterize optical and electro-optical integrated devices in our lab.

As a solution to different challenges, photonic crystals and grating structures comprise an important part of this thesis. Photonic crystal nanocavities can strongly confine photons in a small cavity on the wavelength scale. Exciting pure symmetrical modes in nanocavities is challenging. The second part of my thesis is dedicated to designing a high extinction ratio symmetrical-mode filter based on photonic crystal nanobeam cavities. Through carefully designing the cavity mode and the distributed bragg reflectors we have achieved high extinction ratio for the desired mode against the background transmission in the stop band region. The excitation of symmetrical modes with an even or odd symmetry is based on the design principles for a mode symmetry transforming Mach-Zender coupler. The designed device is fabricated and tested with the surface coupling setup.

Beam expanders or mode converters are widely employed in matching the modes of waveguides of different widths. Here we are interested in a beam expander that can effectively couple the fundamental mode from a narrow waveguide to that of a wide waveguide in a short distance. We find that as the taper length is shorter than the final waveguide width, the insertion loss increases almost exponentially. Designing a compact beam expander with low insertion loss is challenging. In the last part of this thesis, our goal is to design an ultra-compact on-chip mode size converter. This can be achieved through incorporating a composite adiabatic and non-adiabatic structure. We have utilized an evolutionary algorithm to design a beam expander. The fabricated device is characterized with our developed surface coupling setup.

Every Morn and every Night
Some are Born to sweet delight
Some are Born to sweet delight
Some are Born to Endless Night
We are led to Believe a Lie
When we see not Thro the Eye
Which was Born in a Night to perish in a Night
When the Soul Slept in Beams of Light
God Appears & God is Light
To those poor Souls who dwell in Night
But does a Human Form Display
To those who Dwell in Realms of day

— William Blake, Auguries of Innocence

Dedication

In memory of my dear father

Acknowledgments

First, I would like to thank my advisor Dr. Wei Jiang for his patient guidance and the help he provided throughout my doctoral study. I will always be thankful for the opportunities he provided for me to be part of the Rutgers nanophotonics group and the recognitions that would not be possible without his generous support. Specifically, I am grateful for the influences he had on me in the development of my understanding of the value of paying attention to details.

I am highly indebted to my friend and colleague, Robert Gatdula, who conducted most of the fabrication processing in our lab and Dr. Ming Lu and Dr. Aaron Stein for assisting our group with fabrication processes at the Brookhaven national lab.

I also thank my committee members, Dr. Yicheng Lu, Dr. Jaeseok Jeon, Dr. George C. Celler, and Prof. Leonard Feldman for their encouragement and insightful comments.

In so many ways, I am indebted to our former colleagues from the nanophotonics group, Dr. Jun Tan and Dr. Weiwei Song who helped me learn characterization techniques in the nanophotonic laboratory and guided me through fabrication processing at the MERL cleanroom.

In so many ways, I am indebted to Dr. Pavel Reyes and Dr. Wen Chung Hong who taught me the essence of working hard while being responsible.

I am so grateful to Dr. Yicheng Lu for all the insights that I received from him when I faced challenging situations. He is my role model as an advisor who truly cares about students.

I am very thankful to Prof. Zoran Gajic who always welcomes me and finds time for me when I need help.

I appreciate all the help that I received from Dr. Narayan Mandayam without whose kind support I would not finish my PhD. at Rutgers.

I would like to thank Prof. Sigrid Macafee whose sitting in her classes were among the best experiences during my time at Rutgers university.

I am thankful to Dr. Mehdi Javanmard and Dr. Paul Prucnal and their group from Princeton University whom I enjoyed collaborating and sharing experience with.

I would like to take the opportunity to express my gratitude to all the ECE department staff, John McCarthy, Noraida Martinez, Ora Titus, and Steve Orbine, who treated me like a family and provided me with continuous help in the past years.

I would like to thank all my colleagues and friends from our nanophotonics research group, including Amrita Banerjee, Prof. Yating Zhou and Minning Zhou. I am thankful to John Scafidi, Kilti Kodra, Yanbiao Pan, and Sourav Sogar, whom I enjoyed having discussion with.

Finally, special gratitude and love goes to my family for their unfailing support. I would like to thank my mother for being my role model and my sister for her kind support.

This work is supported in part by DARPA Young Faculty Award under Grant No. N66001-12-1-4246. This research is carried out in part at the Center for Functional Nanomaterials, which is a U.S. Department of Energy Office of Science Facility, at Brookhaven National Laboratory under Contract No. DE-SC0012704, in part by the Air Force Office of Scientific Research (AFOSR) under Grant FA9550-08-1-0394, and in part by the U.S. Department of Energy within the Center for Functional Nanomaterials, Brookhaven National Laboratory, Office of Basic Energy Sciences under Grant DE-AC02-98CH10886.

Table of Contents

List of Acronyms

FDTD …………Finite Difference Time Domain
FT …………….Fourier Transform
PBG …………..Photonic Band Gap
SOI ……………Silicon On Insulator
TE ……………..Transverse Electric
TIR …………….Total Internal Reflection
TM …………….Transverse Magnetic
DNB……………Dual Nanobeam
PHC…………….Photonic Crystals
GC……………...Grating Coupler
WDM………..…Wavelength Division Multiplexing
TDM…………..Time Divison Multiplexing
MDM…………..…Mode Divison Multiplexing
SWG ………..…Subwavelength Grating
ZB……………..….Zettabyte
EB……………..….Exzabyte
MZC………..…Mach Zehnder Coupler
BE……………..….Beam Expander
PSO…………....Particle Swarm Optimization
GA…………….Genetic Algorithm
ASE…………...Amplified Spontaneouse Emission

List of Tables

List of Illustrations

Chapter 1. Introduction

1.1 Background and Motivation

Due to the exponential growth of data traffic during last decade – the annual global IP traffic passed the zettabyte ([ZB] – 1000 exabytes [EB]) threshold at the end of 2016 – it was named the Zettabyte era by Cisco [1]. This has fueled the rapid development of high-speed optical communications ranging from long-distance fiber transmission links to short-distance access networks and even further to the shorter-reach of rack-to-rack and in future prospect the backplanes, chip-to-chip, and on-chip optical interconnects. As, the backbone of communication, the expansion of data centers and cloud computing demands higher data transfer speeds and higher bandwidth (100 GHz), as well as high-performance computing in which the interconnection networks bandwidth is emerging as the performance bottleneck. One immediate application for chip-to-chip optical communication would be in resolving the *processor–memory performance gap*, as off-chip bandwidth between the cores and memory is restricted, while the processor bandwidth develops exponentially for every new processor generation [2]. The performance of the multiprocessor chip is diminished by the resulting interplay between off-chip bandwidth and access latency. Photonic interconnects enable immense bandwidth scalability through advanced transmission techniques such as wavelength-division multiplexing (WDM) – where multiple wavelength-parallel optical data streams can be transmitted through a single optical wire. Furthermore, these networks have the potential to simultaneously incorporate different modulation schemes. These schemes include time-division multiplexing (TDM)

– where optical data streams are combined serially on the same wavelength channel to form higher bandwidths; and recently, mode-division multiplexing (MDM) – where the optical data is multiplexed in different modes of a multimode waveguide [3]. All these methods increase bandwidth densities far beyond the feasibility while utilizing conventional electrical transmission systems.

Low-power, low-cost photonic integrated circuits display potential for enhancing the density, reaching distance, and data rates for next-generation data center networks. They also provide a platform for new network architectures and applications that cannot exist with the electrical interconnects. Integration of high density, high performance optical transceivers are enabled through leveraging the compatibility with the CMOS foundry infrastructure [4]. Through the development phase, optical interconnects need to enhance the key factors of power consumption, integration density, reliability and cost.

1.2 Optical Interconnects

Although the development of single microprocessor performance has already slowed down, the performance of the chip is improved by increasing the number of microprocessor cores while keeping total power consumption to approximately 200 Watt due to limited total power budget [5]. In the current chip technology, this communication between cores is done through electrical interconnects, which is not scalable. It has been shown that the capacity of the wire cannot be increased by changing the system size [6]. The limit to the total number of bits per second of information that can flow in a simple digital electrical interconnection is established only by the ratio of the length of the interconnection to the total cross-sectional dimension of the interconnect wiring – the “aspect ratio” of the interconnection. This limit is largely independent of the design of the electrical lines. Additionally, it cannot be altered by either growing or shrinking the system because it is scale-invariant. Therefore, miniaturization of electrical interconnects will not help improve the bit-rate capacity.

Beside the scaling limitation, the signal wavelengths became centimeter scale and the interconnects have started acting as antennae that send and receive signals from nearby metal tracks as clock speeds in new microprocessors have reached the gigahertz regime. This has led to interference or crosstalk between the interconnects in such a way that higher signal power is required to the compensate for both losses of transmission and noise. Coupling between adjacent metal tracks also increased the signal propagation delay.

Optical interconnects do not have an aspect ratio limit because loss in optical media is essentially independent of the modulation bit rate, even in the terahertz regime. Long, thin single mode optical interconnects work substantially well [8].

Another major advantage that optical interconnects have over electrical ones as previously mentioned is the possibility of advanced modulation schemes like wavelength division multiplexing (WDM) such that the aggregate bandwidth can be well beyond the modulation rate on any single channel. This is impossible in electronic systems owing to interference effects. Unlike electrical signals, optical signals are free of the RC time constant and ohmic loss issues, which dominate the bandwidth loss and signal distortion in electrical interconnects.

The three key factors for future interconnect technology are bandwidth density, energy efficiency, and latency [9]. Current Optical links have tow benefits but require overcoming the energy efficiency to be incorporated effectively for on-chip communications and enable communication between multiple cores. Optical interconnects will become increasingly interesting as CMOS nodes continue scaling down, because at small enough nodes, the transistor capacitances become small enough to be directly operated by a photodetector, which can eliminate the trans-impedance amplifier and greatly reduce the power consumption of the receiving link [10]. Low power target furthers the involvement of interconnect technology from electronics (100 fj/bit) to optics (10 fj/bit). So, optical interconnect will become the bottleneck for computation on chip. Developments in the domain of optical interconnect such as the application of photonic crystals offer a platform to manipulate light in a sub-wavelength range, which not only shrinks the footprint of the elements, but also decreases the power dissipation.

The major concerns beside the energy efficiency in replacing electrical interconnects with optical interconnects are the production and integration cost of optical components with existing CMOS circuits and the size and power consumption of the optical components such as the optical source, the electro-optic modulator, and the photodetector [11]. Traditionally, devices used for optical communications have been manufactured with compound semiconductor materials such as gallium arsenide and indium phosphide and electro-optic materials such as Lithium Niobate. Optical components based on these materials have demonstrated excellent performance but suffer due to high cost and large size; these properties relate to complex processing, low yield, and difficulty of integration. Making a standard process to reduce the fabrication cost for optoelectronic integration is necessary as the common material platform for both electronics and optics is Silicon.

1.3 Silicon Photonics

The history of technological development proves that every transition from an established technology to a new one involves a cost. However, this cost can be minimized by maximizing compatibility of the new technology with the previously established one. Silicon processing has become a mature technology with its implementation for over five decades in electronics industry, such that all technological advances pertaining to CMOS microprocessor have been adopted based on its compatibility with silicon technology. Therefore, the most economically viable way of achieving optoelectronic integration is to incorporate the CMOS infrastructure and employ silicon technology for optical devices applications. This is the primary motivation behind conducting silicon photonics research, which began in mid-1980s, with the pioneering works from Richard Soref and has continued thereafter [12].

As an optical material, silicon is transparent at c-band telecommunication wavelengths around 1.53 to 1.565μm and possesses a high refractive index of around 3.45 that allows for sub-wavelength dimension waveguides with very tight bending radii when covered with air or silica (SiO_2) cladding. Therefore, it can be utilized to fabricate compact photonic devices compared to silica. Experimentally, the waveguide propagation loss is dominated by scattering and absorption at the waveguide sidewalls; propagation loss values as low as 0.3 dBcm^{-1} have been demonstrated [13]. Electrically, silicon is a semiconductor – electrons and holes induce a small change in the refractive index of silicon, which can be harnessed as an efficient and effective way to moderate and route light on chip [14]. Moreover, electronic logic circuits can provide added flexibility and reduced power consumption utilizing the real time active-feedback control in on-chip photonics. Besides, silicon has strong nonlinear effects as compared to silica, which can be find application in all optical switching [15], modulation, and routing. Furthermore, 3D integration of silicon photonic devices is advantageous to almost all systems based on silicon photonic technology, as it enables monolithic integration of photonic devices made of Si and Ge on an Si wafer. By introducing the third dimension for photonic device integration, these novel solutions introduce another degree of freedom for maximizing the performance of these photonic interconnection networks.

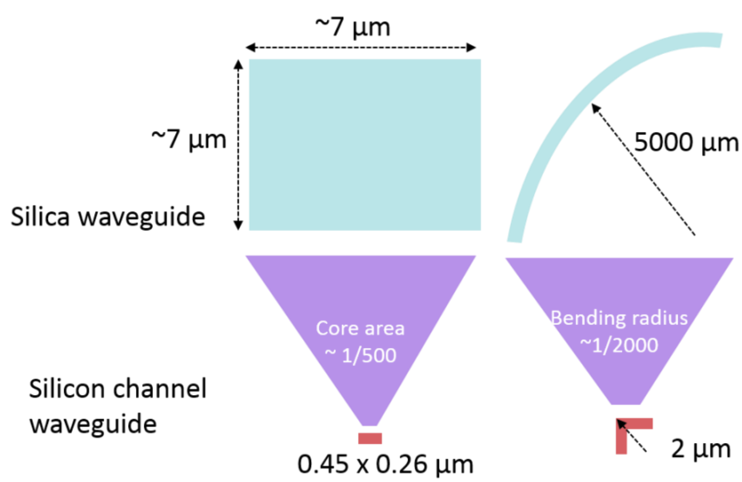

Fig. 1.1. Core size and Bending radius of conventional Silica waveguide and Silicon wire waveguide, reproduced from [10].

Among all features for integration, the compactness of Si photonics makes the largest impact. Cross sections and bending for a Silicon wire waveguide and conventional silica waveguide are shown in Fig. 1.1 for comparison. The silicon photonic wire waveguide has an extremely small core and bending radius and a very strong light confinement due to strong total internal reflection at the Si–silica interface. The silicon waveguide is a suitable platform to reduce the size of photonic devices and high-density integration. Compared to the conventional integrated technology, it has been predicted that employing discrete optical devices that utilize the Silicon photonic in data transmission systems can potentially increase both energy efficiency and integration density by approximately 100 times [10].

The focus on design standards is one key factor that determined the success of CMOS electronics for decades – highly customized and untested designs have been avoided. Standardization on one hand reduces the degree of freedom in designing devices and on the other, it enables a diverse user base to avail itself of libraries of mature and reliable design elements, which ultimately diminishes cost. Silicon photonics offer a similar capability, which makes it highly attractive for applications for the mass-market. One of these standards pertains to the availability of high-quality silicon-on-insulator (SOI) wafers, which is an ideal platform for building planar waveguide circuits. A schematic of an SOI wafer and planar channel waveguide fabrication process is presented in Fig. 1.2. An SOI wafer consists of three layers: a silicon substrate at the bottom for mechanical support, a buried oxide (BOX) layer with 2–3 µm thickness (in the middle) acting as the lower refractive index and the insulating layer, and a thin layer of silicon with 220–260 nm thickness (on the top) acting as the functional planar wave guiding layer for waveguide applications, which may vary in thickness up to 3 µm, ridge waveguide, for certain laser applications [16].

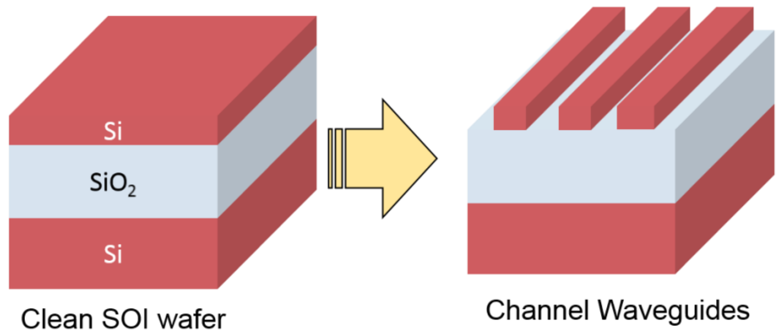

Fig. 1.2. Schematic of SOI wafer and channel waveguide that fabricated through single stage etching process

Silicon photonics are progressively taking over in shorter distance communication networks with the advantages of new advanced modulation techniques and applying advanced processing methods to reduce loss in interconnects. Luxtera announced the world's first 40 Gigabit Optical Active Cable (OAC) in 2007 [17]. Intel demonstrated their 4x12.5 Gbps CWDM silicon photonics link utilizing integrated hybrid silicon lasers in 2010 [18]. IBM unveiled the holey opto-chip that beat the one terabit per second transfer speed record in 2012 [19]. Acacia presented a single-chip 100-Gb/s coherent transceiver in silicon photonics in 2014 [20]. All these advancements show the potential of silicon photonics as a prospective solution for optical interconnects.

1.4 Photonic Integrated circuits

Silicon, which is regarded to be the workhorse of the semiconductor industry, is going to play a major role in optical circuits. In general, silicon photonics integrated circuits technology is categorized into five sub-technologies: waveguide systems, passive devices, modulators, detectors, and light sources. Unfortunately, there are no devices like transistors in optics yet. However, the range of passive optical components demonstrated to find application with silicon is very impressive and includes photonic crystal waveguides, array waveguide gratings, optical phase arrays, waveguide superlattice, grating couplers, mode converters, multiplexers, polarization control devices, filters, ring resonators, and so on.

The waveguide is the primary silicon photonic component that is used to carry high-speed optical data from one point to another [22]. Crystalline silicon photonic waveguides are capable of transmitting wavelength-parallel optical data with terabit-per second data rates through the entire chip [23]. Moreover, these waveguides can be bent [24], crossed [25], and coupled, creating regions where the optical signal can be passed from one waveguide to another. Ideally, the optical signal at a waveguide crossing is transmitted forward without optical power escaping sideways onto other waveguides (in the form of crosstalk), reflecting back from the interface (in the form of back-reflection), or dissipating into the substrate. Significant research efforts have been employed to minimize these losses. However, crystalline silicon waveguide crossings attribute significant power limitations when multiplied by tens, hundreds, or even thousands of instances even with a minimum insertion loss. This is potentially a major drawback for the complexity and scalability of single layer integrated photonic interconnection networks. Moreover, integration density of Silicon waveguides is restricted to 2 μm by the crosstalk between waveguides.

For waveguide systems, the propagation loss of silicon wire waveguides peaks around 1 dB per centimeter for waveguide with line edge roughness of less than 1 nm [26]. This is optimally low for the photonic integration on a Si chip with an area of a few square centimeters. The loss of coupling to an external fiber has also been constricted to less than 1 dB by employing a spot-size converter with an inverse taper [27].

Silica waveguide–based high-performance passive devices (such as wavelength filters) and inverse-taper spot-size converters (SSCs) work as an interface between Si and silica waveguides [28]. These devices are monolithically fabricated on a Si-on-insulator (SOI) wafer.

Chapter 2. Coupling light to silicon photonic chips

2.1 Introduction

Although silicon induces the benefit for large-scale integration, small feature size in waveguide results in the issue of optical mode mismatch between the glass fiber and silicon waveguide. The mode field size, as previously mentioned, is approximately 500 times larger for an optical fiber compared to a silicon waveguide. Therefore, a device that enables adjusting the mode-field diameter is required. Several approaches have been outlined to resolve the mode mismatch problem. One possible solution is edge-coupling employing spot size converters and lensed fibers. High efficiency coupling with insertion loss of 0.5 dB has also been demonstrated [29]. In butt coupling, the fiber mode is focused through a lensed fiber to an inverse taper waveguide – one benefit of butt coupling is that both TE and TM mode can be efficiently coupled with high-transmission bandwidth. However, this approach can be applied only at the edge of chips and implementation of this design requires fabricating extra-long waveguides and the complicated post-process of cleaving and polishing the edge of the chip and tediously optically aligning each side of the waveguide separately, which will increase the test and packaging cost.

Grating Couplers (GC) can be regarded as an alternative solution to resolve the mode mismatch problem. Comparing the butt coupling alignment procedure to grating couplers is much simpler. Additionally, optical alignment can be completed all at once for both input and output of waveguides if the multiple fiber bundle is used. On the other hand, fabrication of grating coupler doesn't need post-processing, and grating couplers can be placed anywhere on a chip, which provides design flexibility and increases device throughput. Grating couplers have been demonstrated to have an insertion loss as low as 1 dB [30], even though it may be difficult to design an efficient grating coupler for both TE and TM modes. Although using grating coupler for coupling light into waveguides may limit the bandwidth, it would be still compatible with most of the communication applications. Grating coupler can be divided into shallow etch gratings [31] and fully etched gratings [32] couplers based on their fabrication process. As the shallow etched grating couplers have larger design space, the insertion of these grating are generally lower while fabricating such grating is challenging. On the other hand, planar fully etched grating couplers on SOI are robust and can be fabricated through single exposure and etching step.

Besides coupling light in and out of the chip, grating couplers are specifically useful to design nano-antennas for one dimension [33] and two dimension [34, 35] off-chip beam steering applications utilizing optical phase arrays.

2.2 Design one dimensional grating couplers on SOI

A grating coupler is a periodic structure of high and low refractive index structures, which can diffract light from propagation in the waveguide to free space that can be used as an optical I/O to couple light through the optical chip. The cross-section diagram of a fully etched grating coupler design is presented in Fig. 2.1. The device is applied on an SOI substrate, which has a thin silicon layer and a buried oxide (BOX) layer. A top oxide cladding layer can be employed to protect the thin silicon layer. The period of grating is defined with Λ, W is the width of grating teeth, ed is the etch depth of the grating to realize

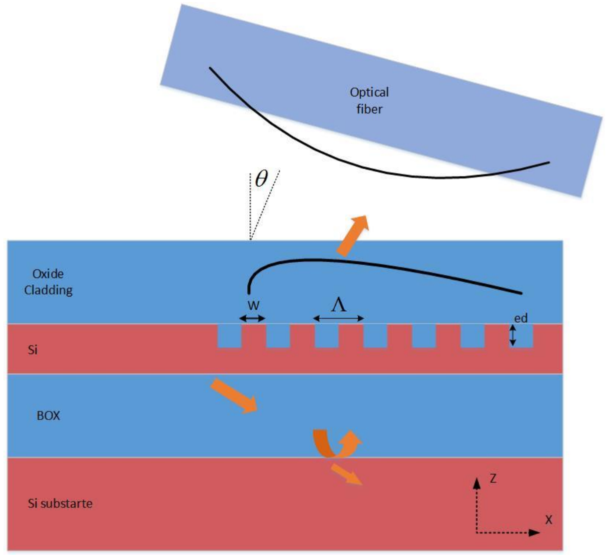

Fig. 2.1. Schematic cross section of a grating coupler, when the light propagating in the functional layer in x direction meets the grating, it partly reflected from the BOX layer and runs out of the grating (z-direction) with the mode profile that is shown in black and coupled substantially to the fiber mode.

the low index region, and in fully etched grating couplers *ed* equals the functional silicon layer thickness.

The performance of a grating coupler is defined by its coupling efficiency or insertion loss and back reflection and the 3dB coupling bandwidth. The insertion loss of the grating coupler is mainly determined by the overlap between the mode field from the fiber and the grating coupler, which is greatly affected by the thickness of the top silicon layer and the thickness of the BOX layer, because these two values impact the phase conditions of different wavelengths at the interface between the grating layer and the buried oxide layer.

A considerable amount of effort has been placed on enhancing the efficiency of grating couplers [36]. The three main elements that reduce the efficiency are as follows:

Penetration loss, in the case of shallow etched gratings, presents about 30% energy lost on the substrate and, in fully etched grating, this penetration loss can be beyond 50%. This can be improved by utilizing metal layer or a multilayer distributed Bragg reflector film that have to be used as reflectors imbedded in the substrate [37].

Mode mismatch loss is one in which about 10% of the light energy is lost due to mode mismatch between gating coupler and fiber; this can be improved by using more sophisticated grating such as apodized grating couplers [38].

Back reflection is normally as small as -30 dB for well-designed gratings. However, it can be as high as 30% in full etch grating.

Grating couplers are effective polarization filters, because the index of the propagating mode in the grating region is highly birefringent, resulting in largely differing radiation angles for TE and TM polarization. This poses a serious limitation for applications in which the input polarization state cannot be controlled, which is generally addressed with two-dimensional grating couplers to couple TE and TM modes individually [39].

The simplified one-dimensional grating couplers are the periodic structures that are described by the Bragg Law. The general from of Bragg condition can be expressed as:

$$\beta - k_x = m.K \tag{2.1}$$

Where k_x is the component of the diffracted wave in the direction of incident wave. Higher order diffractions are denoted by *m.K*. The periodicity of the grating is described by K=2π/Λ, where Λ is the grating period the diffracted wave is travelling in the cladding with and index of refraction n_c. The diffracted light has a wave vector of $k = 2\pi n_c/\lambda$.

Considering the difference between the wave vector of the diffracted light k, and the horizontal component k_x, the diffracted angle can be expressed as:

$$\sin\theta_c = \frac{k_x}{k} = n_{eff}\,\frac{\lambda}{\Lambda} \tag{2.2}$$

Thus, the Bragg condition for grating can be simplified to:

$$n_{eff} - n_c \times \sin\theta_c = \frac{\lambda}{\Lambda} \tag{2.3}$$

Performing the same analysis, the diffraction into the substrate can also be considered.

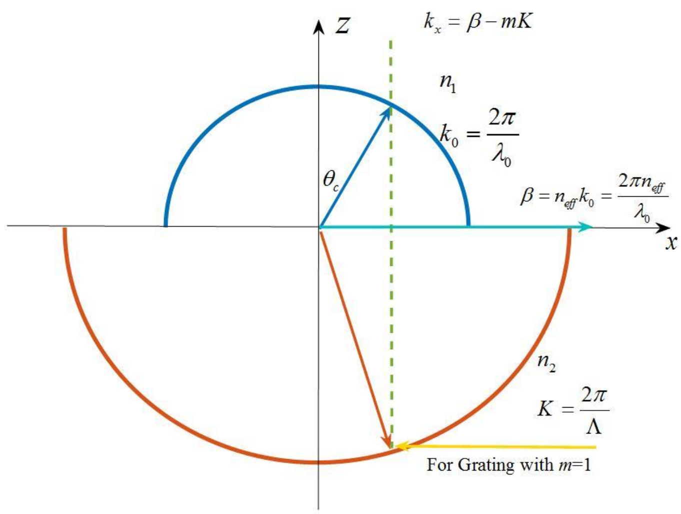

Fig. 2.2. Graphical representation of the Bragg condition for at the interface of grating coupler and top cladding.

The vectoral representation of the Bragg condition for one dimensional grating is illustrated in Fig. 2.2. In the diagram, the angle of light in the grating is closer to the surface normal in comparison with the top cladding with lower refractive index.

The next step in the design process is identifying the limitations of the fabrication process and establishing the design objectives. Subsequently, finding the analytical calculations from the Bragg condition followed by simulating the performance with 3D FDTD simulations. Now, we can simply design a one-dimensional grating coupler by calculating the effective index of high and low index silicon by calculating the refractive index corresponding to each thickness applying the effective index method. We calculated the effective index of the strip waveguide for different modes versus silicon with the Lumerical Eigenmode solver (Fig. 2.3) and different silicon thicknesses (Fig. 2.4) The dotted line presents the cutoff width for single mode waveguide.

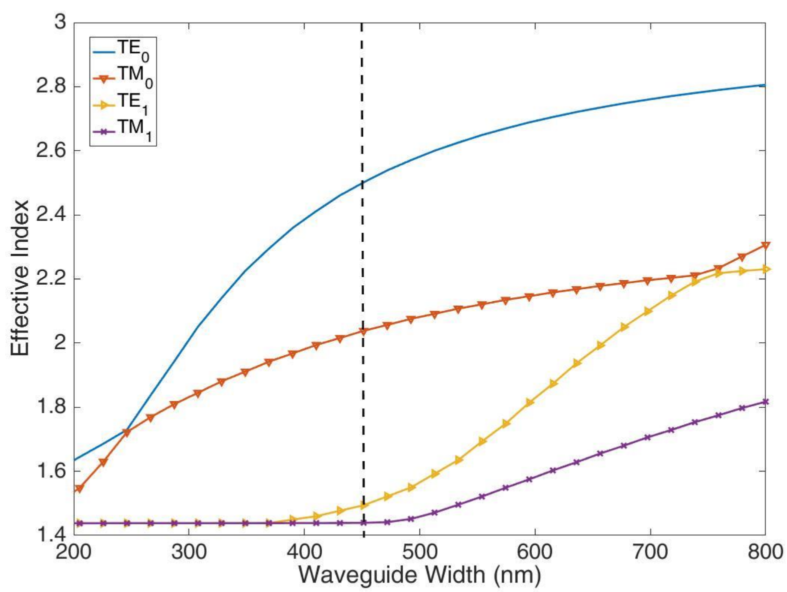

Fig. 2.3. Simulation of the effective index of the waveguide modes versus the width of a strip waveguide for a silicon thickness of 260nm at 1550 nm wavelength. The dotted line presents the single mode cutoff.

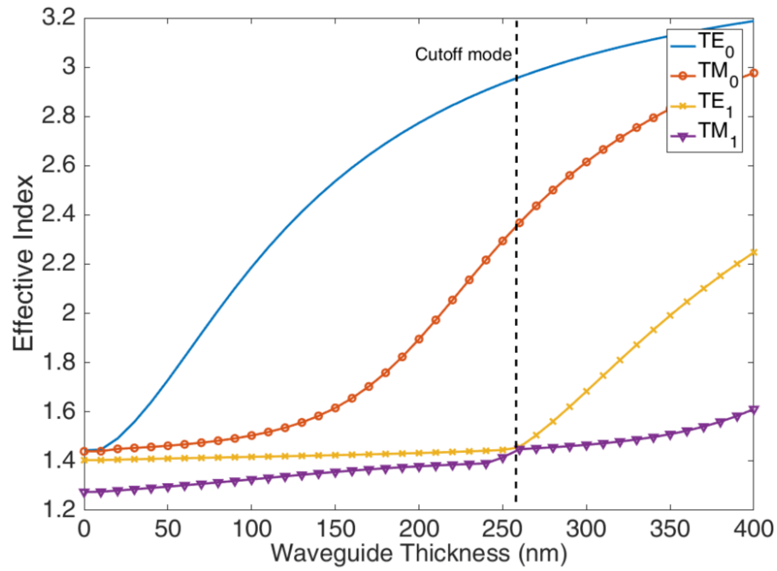

Fig. 2.4. Simulation of the effective index of a strip waveguide versus the thickness of Silicon at 1550 nm wavelength. The dotted line shows the single mode cutoff.

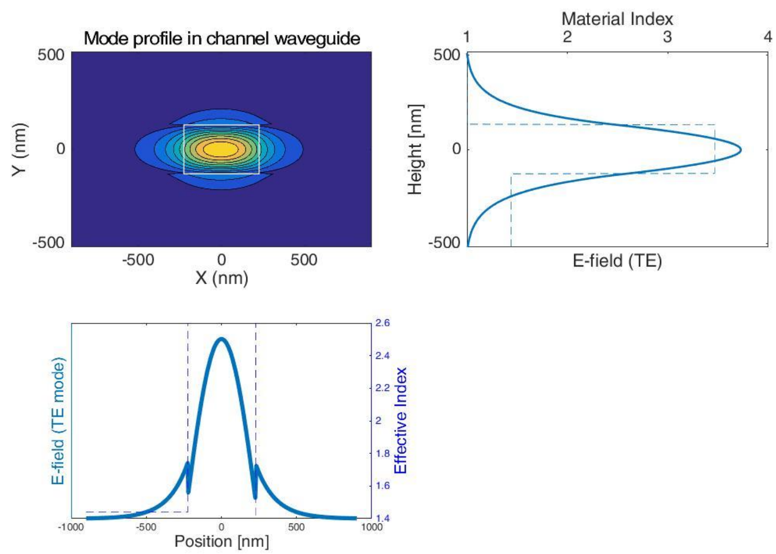

Fig. 2.5. Electric filed distribution in vertical and horizontal direction for a single TE mode strip waveguide with 260 nm height and 450 nm width.

Based on these plots for the single TE mode operation, the waveguide dimensions are suggested to be maintained at 450 nm wide and 260 nm thick. The E-filed distribution of such a waveguide is calculated on the basis of effective medium theory and graphed in Fig. 2.5.

In regular one-dimensional grating couplers, the mode of the fiber is coupled from 10 µm wide grating structure to a single mode waveguide. This grating with two refractive indices of high and low n_{Si} and n_{sub} is shown in Fig. 2.6. As a design example, in the calculations for a single TE mode operation, the thickness of the slab is about 260 nm and by selecting the filling factor of 50%, the effective index of 260 nm slab is about 2.95, and the effective index of 160 nm thick shallow etched region (n_{sub}) is about 2.45 (as represented in Fig. 2.4). Considering these values, the weighted average effective index of grating coupler N_{eff} would be 2.7. Subsequently from equation (2.3), the period of the grating would be approximately 670 nm if the Bragg condition is employed for the diffracted mode at a 15-degree angle.

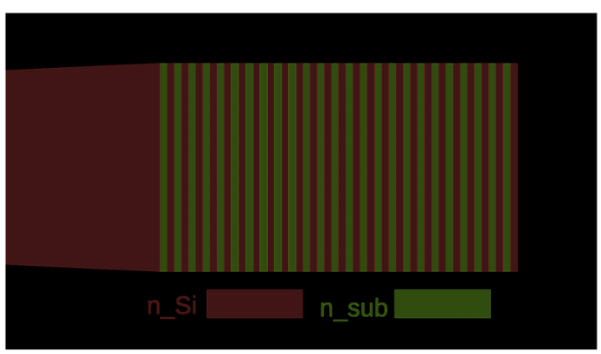

Fig. 2.6. Schematic of a one-dimensional shallow etch grating with n_sub as the etched region with lower index

This diffracted light that is coupled from the optical fiber to the grating coupler has a mode field width of approximately 8.5 µm. This mode needs to convert to a single mode waveguide with 450 nm width. One solution toward matching the modes between two waveguides is using long linear adiabatic tapers that gradually adopts the mode from the wide waveguide of the grating to the narrow single mode one. The long taper will gradually match the effective index of the fundamental TE mode between two waveguides. The effective index for these two waveguides at different wavelength are illustrated in Fig. 2.7. Employing nanostructured devices is the more sophisticated solution to effectively integrate the modes between waveguides that will be discussed at the final chapter.

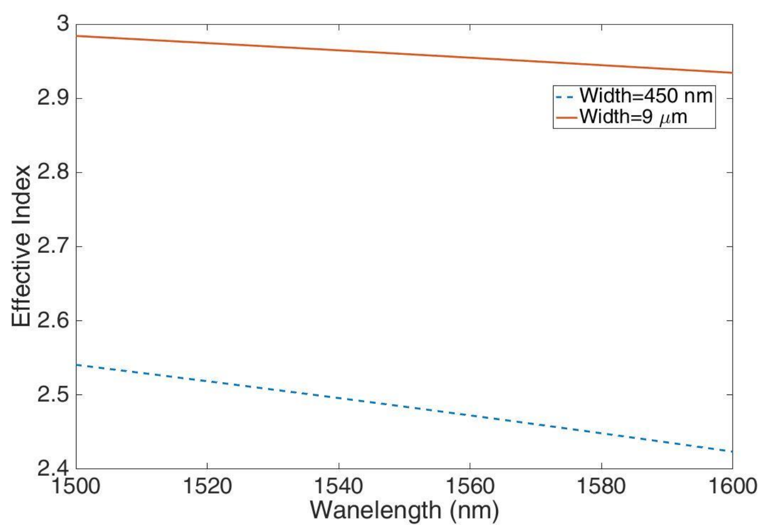

Fig. 2.7. Effective index versus different wavelength for the single mode waveguide and 9 µm wide waveguide.

2.3 Design two dimensional fully etched grating couplers

So far, we have designed a one-dimensional shallow etched grating coupler in which the desired effective index can be designed by selecting the etching depth. This simple design process has low tolerance to fabrication errors. The fabrication challenges for realizing shallow etch grating couplers after several trials lead us to increase the complexity of the designing by adding one more dimension to design space and make a fully etched 2D grating coupler. In fully etched grating couplers, the shallow etch region is replicated by a lateral grating that emulates the effective index of the shallow etch region instead of having one dimensional grating as illustrated in Fig.2.8(a) as compared to Fig. 2.6. Light is diffracted through the grating and coupled into the optical fiber in regular grating couplers. A small angle θ between the axis of the optical fiber and the normal of the wafer surface is generally included to avoid a large Bragg reflection [40]. The subwavelength dimension of the square-shaped holes and the period in the y axis, Λ_{sub}, for the lateral grating structure are smaller than the wavelength of the propagating light, which enables the effective medium theory (EMT) at the zeroth-order to be employed to approximate the structure using a groove with a refractive index n for both TE and TM mode described as below [41]:

$$\frac{1}{n_{TE}^{(0)}} = \left[\frac{f_y}{n_{hole}^2} + \frac{(1-f_y)}{n_{Si}^2} \right]^{1/2}$$
$$n_{TM}^{(0)} = \left[n_{hole}^2 f_y + n_{Si}^2 (1-f_y) \right]^{1/2} \tag{2.4}$$

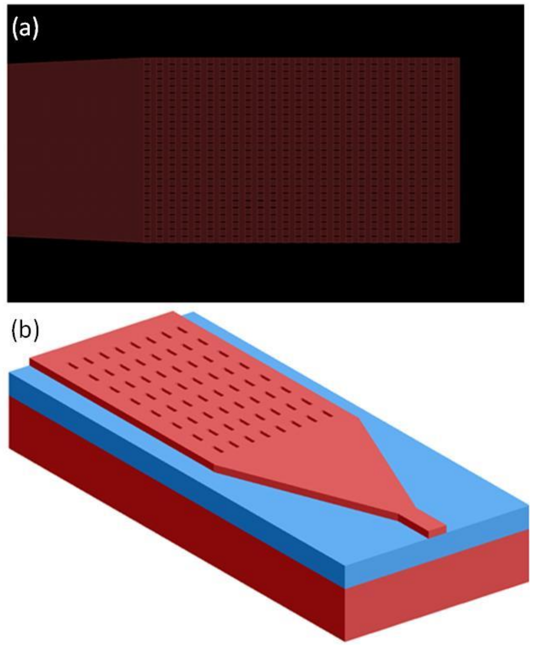

Fig. 2.8. (a) Fully Etched 2D grating coupler designed by the lateral grating, which emulates the effective index resulting from shallow etch process (b) two dimenstional grating coupler on SOI.

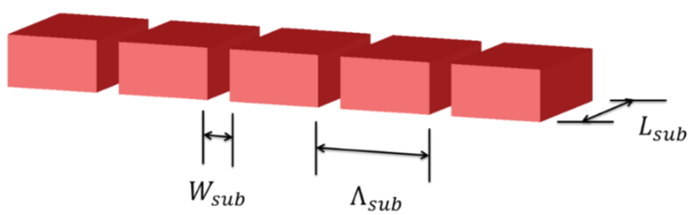

Fig. 2.9. The design parameters for the lateral grating

Where $n_{TE}^{(0)}$ and $n_{TM}^{(0)}$ are the refractive indices of the approximated groove derived by the EMT. n_{hole} and n_{Si} are 1.45 and 3.45 respectively. The lateral fill factor is denoted by f_y =1-W_{sub}/Λ_{sub}. This simple relation based on zero-order approximation is only accurate when the period to wavelength ratio, which is defined as $R = n_{si}\,\Lambda_y/\lambda$, is much greater than 1. More accurate approximations suggest that employing of the second-order EMT can be implemented if the lateral feature size is of the same order as the wavelength medium [42, 43]:

$$n_{TE}^{(2)} = n_{TE}^{(0)}\left[1+\frac{\pi^3}{3}R^2 f_y^2(1-f_y)^2(n_{hole}^2-n_{Si}^2)^2\times\left(\frac{n_{TM}^{(0)}}{n_{effTE}}\right)^2\left(\frac{n_{TE}^{(0)}}{n_{hole}n_{Si}}\right)^4\right]^{1/2}$$

$$n_{TM}^{(2)} = n_{TM}^{(0)}\left[1+\frac{\pi^3}{3}R^2 f_y^2(1-f_y)^2\left(\frac{n_{hole}^2-n_{Si}^2}{n_{effTM}n_{TM}^{(0)}}\right)^2\right]^{1/2} \tag{2.5}$$

Where $n_{TE}^{(2)}$ and $n_{TM}^{(2)}$ are the effective indices of the approximated groove driven by the EMT with second order approximation. These equations give more accurate results for the subwavelength grating coupler when the lateral feature size is insignificantly smaller than the wavelength.

To obtain further accurate calculations, we can derive the refractive indices of lateral grating for TE and TM by the effective mode theory without any assumption through the following equations [43]:

$$TE \ \ \text{mode}: \frac{\sqrt{n_{si}^2-n_{TE}^2}}{n_{Si}^2}\tan\left(\frac{\pi\sqrt{n_{si}^2-n_{TE}^2}\left(\Lambda_{sub}-W_{sub}\right)}{\lambda}\right) = \frac{\sqrt{n_{hole}^2-n_{TE}^2}}{n_{hole}^2}\tan\left(\frac{\pi\sqrt{n_{hole}^2-n_{TE}^2}W_{sub}}{\lambda}\right) \tag{2.6}$$

$$TM \ \ \text{mode}: \sqrt{n_{si}^2-n_{TM}^2}\tan\left(\frac{\pi\sqrt{n_{si}^2-n_{TM}^2}\left(\Lambda_{sub}-W_{sub}\right)}{\lambda}\right) = -\sqrt{n_{hole}^2-n_{TE}^2}\tan\left(\frac{\pi\sqrt{n_{hole}^2-n_{TM}^2}W_{sub}}{\lambda}\right) \tag{2.7}$$

Where n_{TE} and n_{TM} are the refractive indices of the lateral grating for TE and TM polarizations respectively, with no constraint on the grating dimension. In our design, the holes are pumped with air. Λ_{sub} is the period of the horizontal grating, and W_{sub} is the width of the rectangular air holes. The filling factor of the lateral grating is defined as $f_{sub} = W_{sub}/\Lambda_{sub}$. As the transcendental equations of (2.6) and (2.7) do not have an explicit analytical solution, we managed to solve them numerically. The plotted results of n_{sub} for the equations (2.4), (2.5), (2.6), and (2.7) versus f_{sub} are illustrated through Fig. 2.10. Although n_{sub} does not vary much with the zeroth-order or first-order approximations, these approximate values tend to deviate from the n_TE calculations from equation (2.6).

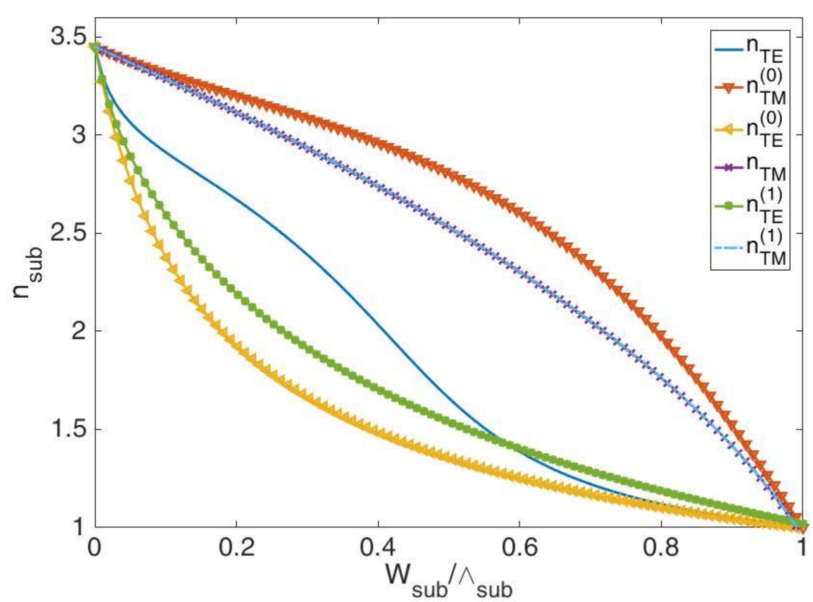

Fig. 2.10. Refractive index of the lateral grating for different filling factors, calculated by the EMT based on zero order, first order approximation, and without any approximations.

Designing 3D grating couplers is expensive in computational terms. We emulate the effective index of a lateral grating in fully etched 2D grating through one-dimensional shallow etch grating to simplify the problem. Now, we aim to find the etching depth that provides the highest coupling power. The eigenmode expansion method is utilized to calculate the effective index of the optimal etching depth. The optimal etching depth is calculated by performing multiple simulations for different grating pitch. The etch depth of the shallow etch grating coupler, the calculated transmission for a 1D grating with fiber angle of 17 degrees, and 2 um BOX layers are presented in Fig. 2.11.

The goal was to discover the corresponding parameters for maximum transmission. Based on Fig.2.11, we observe the optimal etch depth to be 160 nm that corresponds to n_{eff}=2.55.

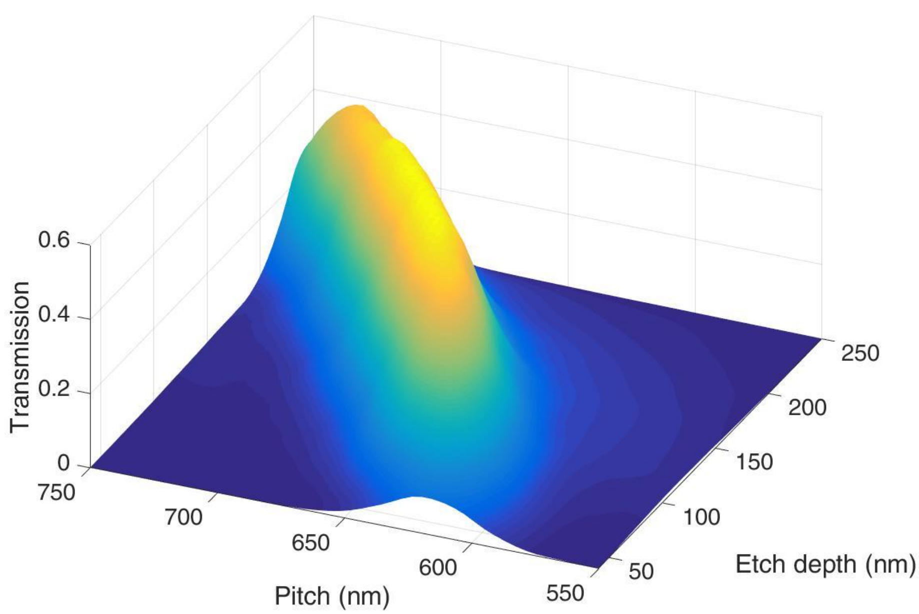

Fig. 2.11. Transmission calculated for different pitch and etching depth for a one-dimensional grating coupler considering fiber angle of 17 degrees and 2 um BOX layer.

Theoretically, any lateral grating with an effective refractive index of 2.45 may be employed to fill the low index regions of a periodic structure, which is a lateral grating in this case. However, the coupling efficiency heavily relies on n_{sub}. Therefore, a precise control of n_{sub} is crucial for achieving high coupling efficiency. As demonstrated in Fig. 2.10, the lateral grating is a good solution to provide precise control on the effective index. From the TE polarization calculation of effective index, the corresponding f_{sub} for n_{sub}=2.55 is 0.265 according to the numerical calculation of Fig. 2.10. Thus, Λ_{sub} reaches close to the wavelength inside the slab waveguide. The W_{sub} that can be fabricated considering all limitations with sharp sidewalls that are approximately 90 nm, which corresponds to Λ_{sub} of 340 nm. The total design parameters for 2D fully etched grating coupler is listed in Table 2.1.

Table 2.1. Fully etched 2D grating coupler design parameters calculated from the optimal effective index and solving Eqs. (2.6) and (2.7)

n_{sub}	Λ_{sub} **(nm)**	Λ_G **(nm)**	W_{sub} **(nm)**	L_{sub} **(nm)**	F_G	F_{sub}
2.55	340	680	90	340	0.5	0.735

We employed the 3D finite difference time domain (FDTD) software package by Lumerical to verify the optimized design values from the fully etched 2D grating.

The simulations are done for different filling factors of the lateral grating as well as optimizing the fiber angle position from 17 to 22 degrees as shown in Fig. 2.13. The optimal simulated values reflect peak transmission for W_{sub} at 90 nm and fiber angle 17 degrees.

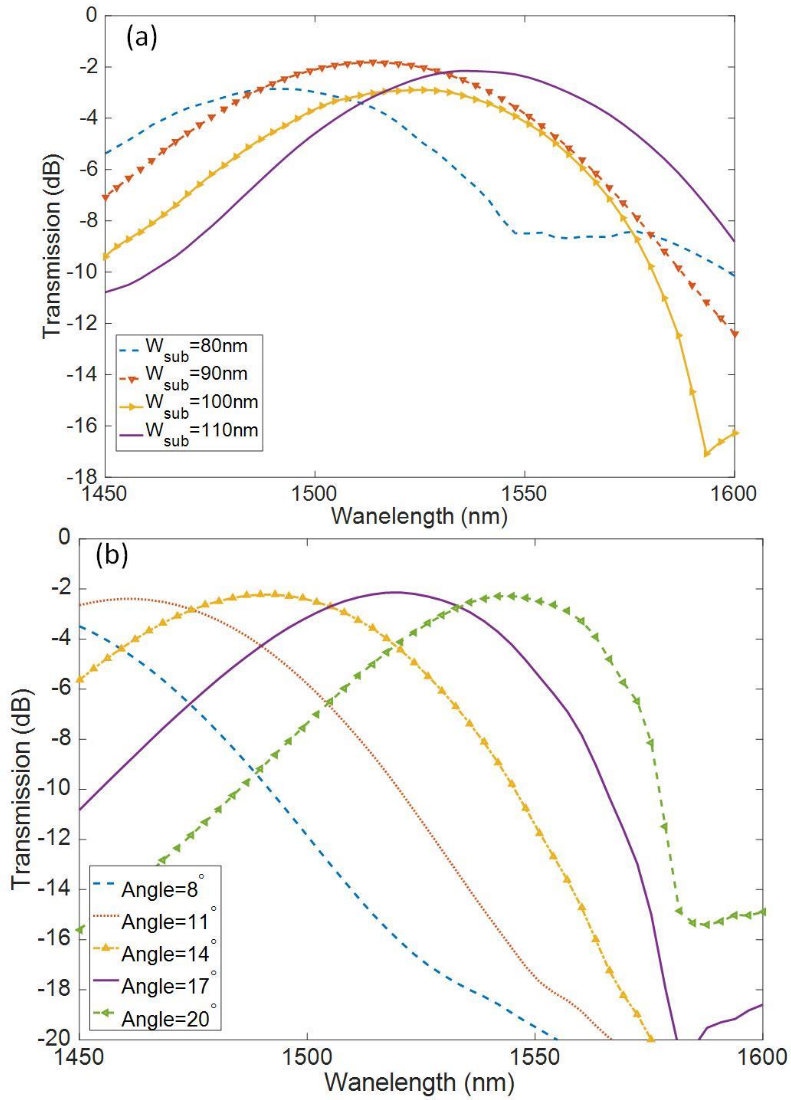

Fig. 2.12. (a) Numerical simulation for a single fully etched grating coupler for TE mode at different lateral grating hole width (b) and different fiber angle.

2.4 Measurement results and analysis

The measurement and characterization as well as the design and fabrication of optical chips are critical steps in checking the validity of the theory and design. We developed a robust, low loss measurement setup to speed up the optical and electrical measurement process to characterize the designed grating couplers – this provided consistent measurement results for various chips. The grating couplers structure is fabricated on an SOI wafer with a 2 µm buried oxide layer and a 260-nm top silicon layer. It is patterned employing a JEOL JBX-6300FS high-resolution e-beam lithography (EBL) system operating at 100 keV on a 120-nm-thick XR-1541-006 hydrogen-silsesquioxane (HSQ) negative e-beam resist. The pattern is transferred to the silicon layer via an Oxford Plasmalab 100 ICP etcher, using an $HBr+Cl_2$ based chemistry for vertical and smooth sidewalls.

The top view and the cross-view scanning electron microscopy (SEM) images of the fabricated grating are presented in Fig. 2.13(a). A cross section view of the lateral grating structure and magnified view of the air holes are illustrated in the Fig. 2.13(b) and (c) respectively.

Specially to characterize the high density integrated optical devices such as waveguide superlattices [44], we need to perform multiple alignment and measurements; to enhance the alignment speed, we incorporated the V-groove array fiber in the setup. We were able to align and measure up to 24 array waveguides implementing computer automated measurement procedures all at once [45].

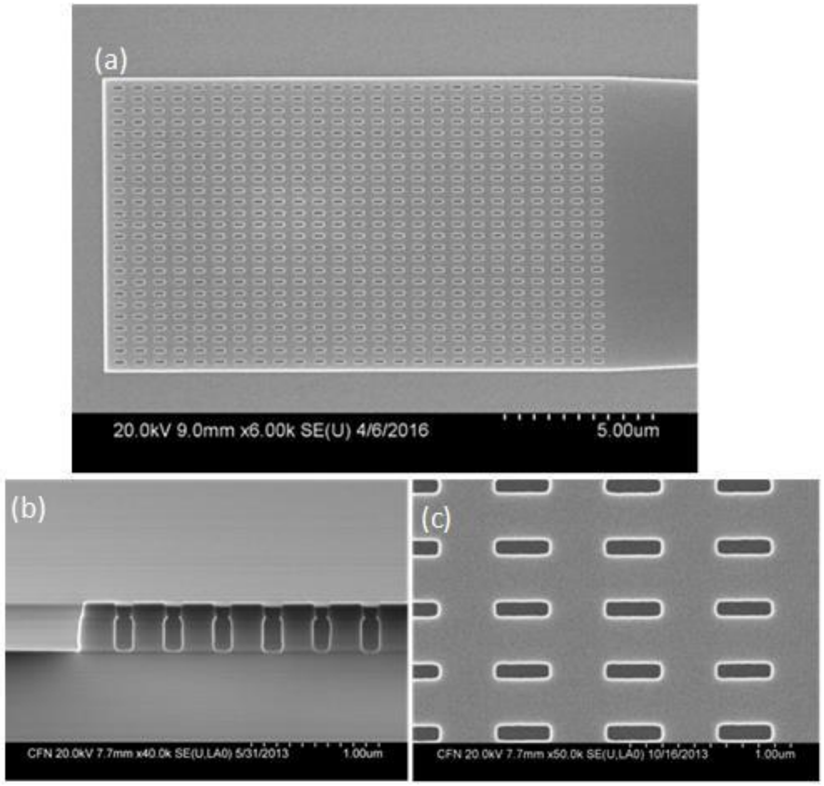

Fig. 2.13. Scanning electron micrograph of the fabricated 2D grating coupler on SOI, (a) fully etched grating of 17.1 µm long and 10 µm wide, (b) cross section of the fully etched lateral grating (c) zoomed in view of two dinesional grating.

The measurement setup is provided in Fig. 2.14. The input and output fibers are bundled together in a V-groove scheme, which are in turn mounted on rotating stages. The tilt angle can be moderated from 0 to 25 degrees. Both input and output fibers are tilted 17 degrees from normal incidence for this design. The fiber positions are controlled by one xyz translational stage. Two cameras are mounted – one on top to align the chip with the edge of the V-groove and the other at a 45-degree angle to visually aid the alignment. The input fiber is a polarization maintaining fiber (PMF), and the polarization is controlled via

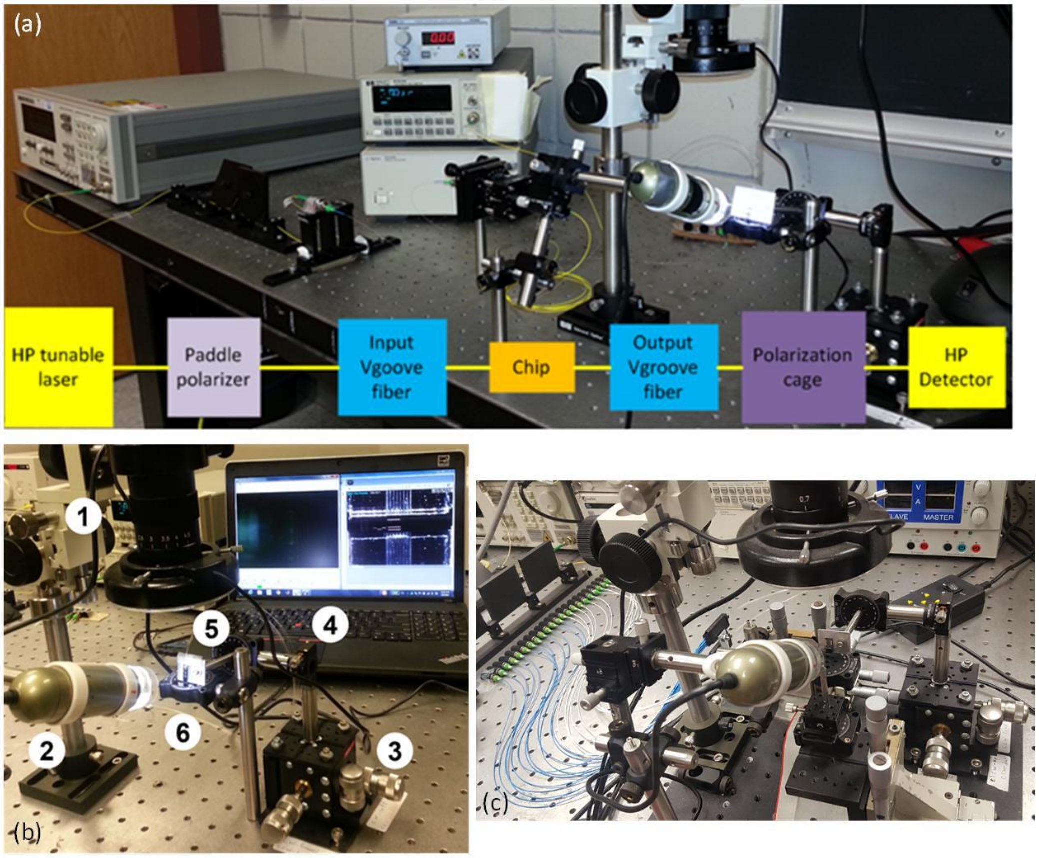

Fig. 2.14. Surface coupling optical measurement setup (a) Full setup connections. (b) (1) Top camera; (2) 45 degrees tilted camera; (3) xyz translational stage; (4) computer for controlling tunable laser and reading optical detector; (5) tilted V-groove mount; and (6) chip stage. (c) The enhanced surface coupling setup with 24 V-groove fiber arrays

a paddle polarization controller (PC). Light is coupled into a 500 µm long, 450 nm wide waveguide via a pair of grating couplers. The existence of higher order modes has negligible effects on the test results, as the fundamental mode contains most of the power. A pair of linear adiabatic waveguide tapers, each with a length of 120 µm, is utilized to convert the mode between the 10-um wide grating region and the single mode waveguide. The coupling efficiency is extracted, assuming equal coupling efficiencies for both gratings due to time reversal symmetry rule in passive waveguides. The transmission spectrum, as shown in Fig. 2.15 (a), is measured with the sweeping wavelength of a TE-polarized light from an HP 8168F tunable laser source and the transmission is measured through a detector. The peak efficiency is measured to be -2.98 dB. The peak wavelength shifts to 1551 nm probably due to fabrication inaccuracies. The 1dB and 3dB bandwidths are 26.1 nm and 47.7 nm respectively. The Fabry-Perot fringes near the peak wavelength are of a small magnitude, indicating low back reflection. The grating coupler transmission results from the measurement for different V-groove fiber angles as presented in Fig. 2.15 (b). The peak transmission loss as well as the 1 dB and 3 dB loss for each angle is listed in Table 2.2. The angle is tuned between 16 and 17 degrees to maximize the transmission due to fabrication imperfections.

Table 2.2. The transmission measurement from fully etched grating coupler

Angle [ϕ]	**Peak Insertion Loss [dB]**	**λ_0 [nm]**	**$\Delta\lambda_{1\text{-dB}}$ [nm]**	**$\Delta\lambda_{3\text{-dB}}$ [nm]**
14	-3.7247	1557	23.7	44.2
16	-2.9825	1551	26.1	47.7
17	-3.0007	1551	26.4	48.7
18	-3.9636	1540	24.4	44.0
20	-6.2879	1533	24.5	44.1

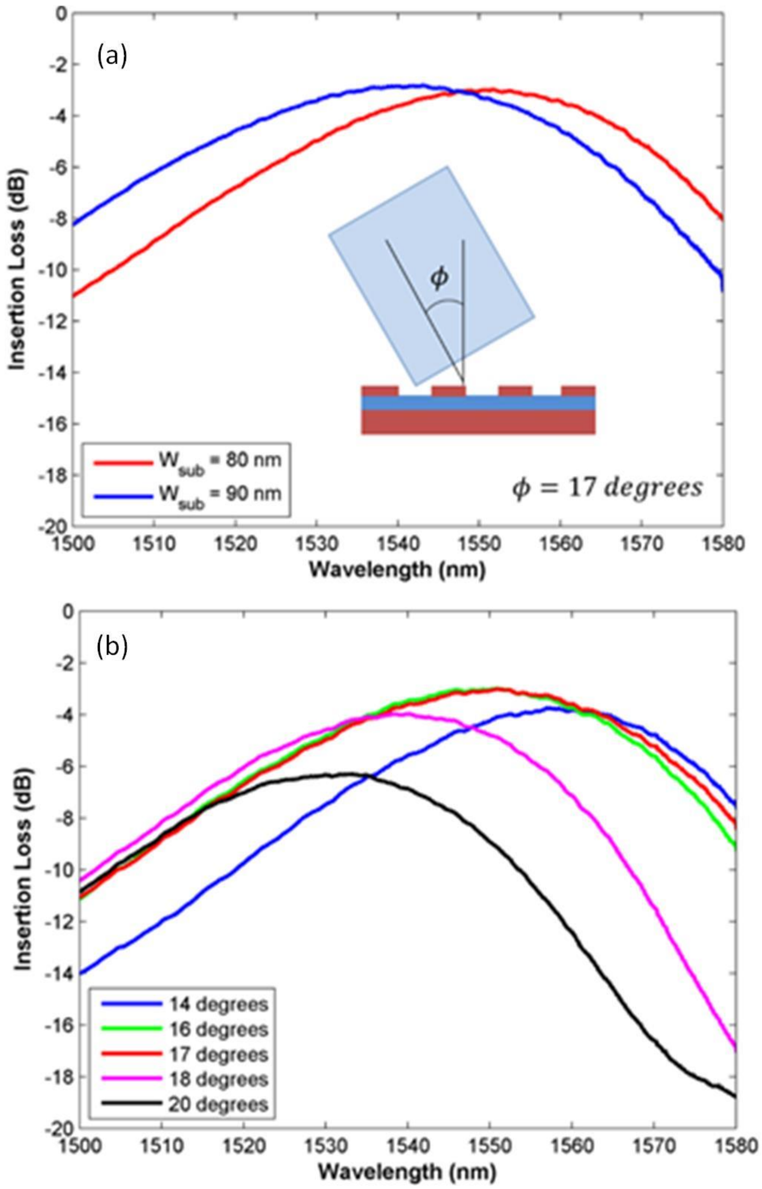

Fig. 2.15. Measurement results for (a) TE mode coupled to a single grating coupler with different lateral grating width and (b) Effect of fiber angle in transmission for a single grating coupler.

2.5 Conclusion

We aim to design a robust, low loss and fairly wide band fully etched two dimensional grating coupler, which enables coupling TE mode light from the chip surface to characterize integrated optical devices on SOI. The optimized design has -2.5 dB insertion loss. The device is fabricated through E-beam lithography process and single step etching process. The measured insertion loss of around 3 dB per grating and the fully etched grating has 48 nm bandwidth around c-band. We have developed a semi-automated measurement setup to conduct all the optical measurements through a V-groove optical fiber coupler scheme.

Chapter 3. Optical microcavities

3.1 Introduction

Optical micro-cavities are small cages that confine light by repeated reflections from the boundaries. The highly reflective boundaries make the light bounce back and forth into the cavity region that needs to be small in dimensions in spatial direction. A small cavity has large spacing in k-space based on the uncertainty principle, which applies to every wave-like system, so the resonance frequencies are sparse. Like the quantum well in condensed matter physics, the boundaries of bounded states inhibit the wavefunction to extend beyond spectral bands. Here, the absence of resonance modes in extended spectral bands can curb the emission from the source placed within the micro-cavity.

We have already acknowledged silicon as a viable candidate for integrated photonics due to the compactness of optical components. Reducing device size furnishes significant improvement in terms of integration density, energy consumption, and cost. Conversely, it increases the light-matter interaction through resonances; as a result, there is a growing interest in resonance-based devices for different optical components such as narrow band optical filters, modulators, multiplexers, and routers [46]. Resonance-based devices in integrated photonic circuits are implemented in a planar configuration utilizing coupled waveguide resonator architectures. Their wavelength selective nature further makes them compatible with dense wavelength division multiplexing (DWDM) applications. There are several key factors of an ideal waveguide-resonator, which can be summarized as the following:

• Small device footprint (to achieve high integration density and lower the cost)

• High-quality factor (for narrow band filtering and sensing operation)

• Low mode volume (for low power applications)

• High extinction ratio (to increase the system signal to noise ratio [SNR] and reduce modulation voltage)

• Low loss, include coupling and scattering loss (to reduce the power budget)

• Large Free Spectral Range (to increase channel scalability)

Therefore, an ideal cavity is the one that can confine light in a very small space and retain it forever, without loss, which should have resonant frequencies at precise values. Any deviation from the ideal lossless condition is described by the cavity quality (Q) factor. Reducing the losses to zero within a cavity is impossible in practical cavities at room temperature, so an efficient optical micro-cavity is one that can store a larger proportion of the light as compared to that lost during the cavity lifetime. The Q factor describes the energy stored in the cavity in relative terms to that lost by the cavity per round trip. The Q factor depends on various factor such as scattering loss inside the cavity, the coupling loss, absorption loss, and cavity size. The effective mode volume (V) of a micro-cavity, beside its Q factor, define the application of these devices.

In integrated photonics, two types of resonators are basically utilized: traveling wave resonators such as micro-ring or micro-disk resonator, and standing wave resonators such as Fabry-Perot resonator and photonic crystal cavity resonator. Both the resonator and the waveguide are monolithically fabricated on the same platform in traveling wave resonators, which owing to their compactness, high extinction ratio, and high-quality factor have drawn lots of attention of late [47]. However, their limited Free Spectral Range (FSR) bounds the scalability and restricts the number of channels that can be multiplexed when used in a WDM system due to their size limitation. On the other hand, ring resonators implemented for switching, filtering, and routing application display high sensitivity to fabrication tolerance and thermal drift [48]. Micro-disk resonators as against micro-ring one's present higher Q factor and larger free spectral range. The cavity in Fabry-Perot cavities is one that is sandwiched between two highly reflective mirrors comprising Distributed Bragg Grating reflectors (DBRs), which reflect light at some defined frequencies through total internal reflection from the walls of the cylinder on the basis of the mirror that comprises a subwavelength grating. Photonic crystal cavities are capable of strongly confining light in a subwavelength dimension by means of the photonic bandgap effect [49] in both space and time. The design process of silicon two-dimensional photonic crystal (PHC) cavities with ultra-low mode volume, ultra-high-quality factor, and large FSR is relatively mature [50]. Nevertheless, efficiently coupling light through the cavity is challenging due to their ultra-small mode volume, making the overall extinction ratio of such devices low for any practical applications. Other than that, considerable optical coupling loss is added due to the large refractive index mismatch between silicon waveguide and the optical fiber for all silicon based planar structures. For comparison, different photonic crystal cavities are shown in Table 3.1. The image of a ring resonator and disk resonator, as well as the Fabry-Perot resonator and a two-dimensional photonic crystal cavity are shown in Fig. 3.1.

Table 3.1. Integrated photonic cavities compared based on their Q and Veff and FSR for several experimental results

Geometry	FSR (nm)	Q	V_{eff} (λ/n)	Ref.
Fabry-Perot	81.7	27×10^3	large	[51]
Micro-disk	5.1	7×10^5	large	[52]
Micro-ring	2	8×10^4	large	[53]
1D PHC	large	7.42×10^3	0.025	[54]
2D PHC	large	1.2×10^7	2.35	[55]

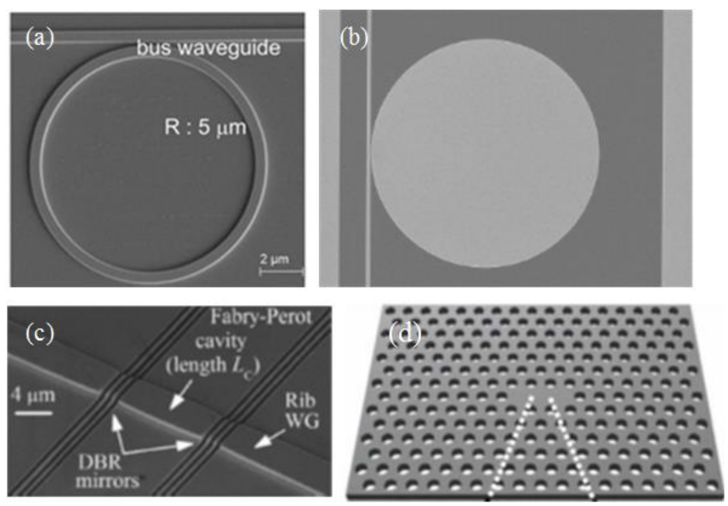

Fig. 3.1. SEM image of (a) ring resonator, (b) Disk resonator, (c) Fabry-perot resonator and (d) two-dimensional photonic crystal resonator from the refs listed in the table.

3.2 Photonic crystals and the idea of bandgap

To qualitatively study the light propagation in Photonic crystals, let us consider a simple general case of a one-dimensional periodic waveguide structure that consists of rectangles of refractive index n_1, which are spaced periodically at a pitch Λ at the boundary of two media with refractive indices n_2 as upper cladding and n_3 as substrate, which is presented in Fig. 3.2. Then, the duty cycle of the periodic structure is w/Λ, and the thickness of the core layer is H. As we have already introduced SOI waveguide in the first chapter as a solution for integrated optic, let us assume that the waveguide core material is silicon, $n_1 \sim 3.5$, the substrate can be silicon oxide or air, $n_3 \sim 1\text{-}1.45$, and the upper cladding can be silicon oxide, a polymer, or air, so that $n_2 \sim 1\text{–}1.6$, which results in sub-wavelength pitches of around $\Lambda \sim 300$ nm for a free-space wavelength around 1.55 μm.

Assuming the light incident is in the z direction, this periodic structure can function in three different regimes depending on the ratio between the structure's pitch and the free-space wavelength. First is diffraction, where the incoming beam is scattered out of waveguide plane in different orders. Second is reflection, where the incoming beam is reflected backwards. Third is sub-wavelength, where diffraction and reflection effects arising from the periodicity of the structure are suppressed.

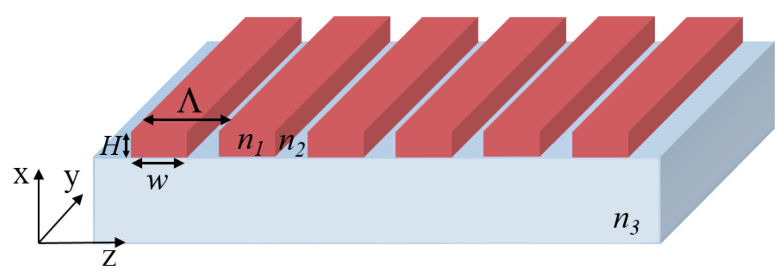

Fig. 3.2. Schematic of a z-periodic dielectric waveguide, with n_1, n_2, and n_3 being the refractive indices of the core, upper cladding, and substrate materials.

This one-dimensional structure displays periodicity only in the longitudinal z direction, but not in the transverse x and y directions. As shown in Fig. 3.2, when the light travels in the z direction through the periodic structure, the light rays tend to remain confined in n_1, as the core index is higher than the substrate and upper cladding ($n_1 > n_2, n_3$) due to total internal reflection. The light strikes the interface of the core to the substrate or the core to the upper cladding at such shallow angles that are wholly reflected based on Snell law – this is called index-guided in lateral *x* direction. Analogous to the semiconductor periodic lattice, this structure performs as a periodic waveguide and follows the Bloch–Floquet formalism [51]. Light propagating in a segmented waveguide adapts to the periodicity of Bloch modes in the periodic structure, with a mechanism that is similar to electron propagation in periodic crystals. Propagation of a Bloch mode through a z-periodic waveguide can be expressed as $E(x, z + \Lambda) = E_B(x, z) \exp(-\gamma_B \Lambda)$, where $E_B(x, z)$ is the Bloch mode field distribution within a single period, and γ_B is its complex propagation constant. In general, $\gamma_B = \alpha_B + jk_B = \alpha_B + j(2\pi/\lambda)n_B$, where α_B and k_B are the attenuation and propagations constants, and n_B is the effective index of the Bloch mode. As previously mentioned, the behavior of a periodic waveguide for a given pitch, Λ, is greatly dependent on the operating frequency, ω, or equivalently, the free-space wavelength. Fig. 3.3(a) shows a schematic k–ω diagram of this periodic waveguide [56]. The three different regimes demonstrated in the Fig. 3.3 are such that for low frequencies ($\omega < \omega_1$) in Sub-wavelength domain, the propagation constant (k_B) grows monotonically, indicating that the periodic waveguide behaves like a conventional waveguide. The electric field of light propagating through the periodic waveguide in this domain is illustrated in Fig. 3.3(c). In the frequency range corresponding to the photonic bandgap ($\omega_1 < \omega < \omega_2$), light is unable to propagate through the structure and Bragg reflection occurs as reflected in Fig. 3.3(d). In this domain, k_B is constant, $k_B^{Bragg} = \pi/\Lambda$.

Above the first bandgap, the light wouldn't have remained confined in the waveguide and the Bloch mode becomes leaky, so light is partially radiated out of the waveguide, as shown in Fig. 2.3(e).

To gain another perspective, it is useful to re-plot the k–ω diagram of Fig. 3.3(a) as the effective index of the Bloch mode, n_B, versus the wavelength to-pitch ratio, $\bar{\lambda} = \lambda/\Lambda$. When $\lambda >> \Lambda$ in the deep sub-wavelength regime, n_B is almost flat. As the bandgap is approached, n_B increases, and then closely follows the linear relation $n_B^{Bragg} = 0.5 \times (\lambda/\Lambda)$ within the bandgap. Although this linear behavior has been meticulously proven only for a two-layer periodic structure, most periodic waveguides of practical interest exhibit this approximately linear response within the bandgap. For lower values of $\bar{\lambda}$, light is diffracted out of the waveguide. Although not illustrated here to ensure simplicity, it should be noticed that higher order reflection and diffraction bands appear alternately for lower values of $\bar{\lambda}$.

In the diffraction domain, periodic waveguides can function as fiber–chip surface grating couplers as discussed in the first chapter [57], where the coupling efficiency from the planar waveguide to the optical fiber located above the chip can be optimized by carefully designing the grating geometry. The sub-wavelength regime is reached when the ratio of wavelength and pitch is high enough for the effective index of the Bloch mode to drop below the Bragg threshold: $n_B < 0.5 \times (\lambda/\Lambda)$. In this case reflection and diffraction effects are then suppressed, and the structure functions in the sub-wavelength domain. Light propagates through the periodic

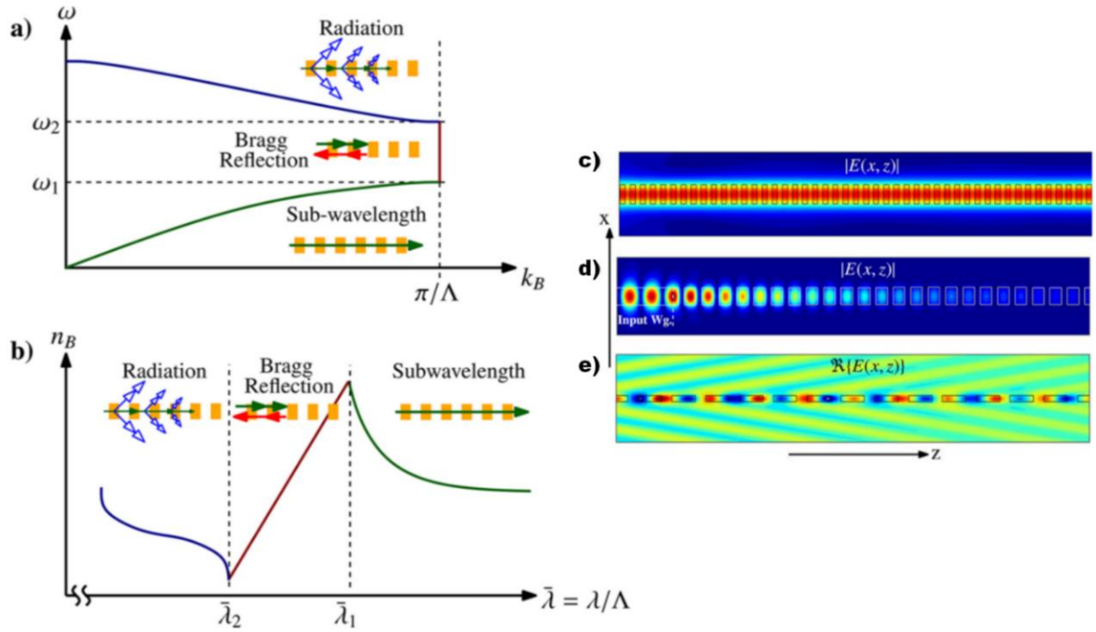

Fig. 3.3. (a) Schematic dispersion diagram of a periodic waveguide with propagation along the z axis. (b) An equivalent representation of the Bloch mode effective index of the periodic waveguide as a function of the wavelength-to-pitch ratio $\bar{\lambda} = \lambda/\Lambda$. Higher order diffraction and reflection bands are not shown. (c) Propagation of light through a periodic waveguide with symmetric vertical structure in the sub-wavelength regime. (d) In the bandgap light is reflected back into the uniform input waveguide. (e) For wavelengths comparable to the pitch of the structure, light is radiated out of the waveguide, reproduced from [56].

waveguide without losses despite the multiple discontinuities along the propagation direction. If the grating extends indefinitely in the x and y directions and $\lambda \gg \Lambda$ (deep-sub-wavelength regime), it can be modeled as an equivalent homogeneous medium with a refractive index given approximately by Rytov's formula, $n^2 = \frac{a}{\Lambda} n_1^2 + (1 - \frac{a}{\Lambda}) \mathrm{n}_2^2$, for light polarized parallel to the interfaces between the media (along the x or y axis)[58]. This is similar to discovering the equivalent bandgap of compound semiconductor materials. This approach furnishes a qualitative description of the behavior of sub-wavelength grating structures, which is of utility in a preliminary stage of the design process. However, the actual structure does not extend infinitely in the x and y directions; waveguiding effects need to be considered, and the model of the subwavelength grating will depend on the properties of the Bloch mode propagating through it at the interface of the waveguide and the periodic structure. An accurate analysis of the sub-wavelength grating waveguide requires the application of advanced numerical tools optimized to analyze periodic structures, such as Lumerical [59] or COMSOL [60]. Note that it usually cannot be modeled with simple equivalent materials if there are several modes propagating through the periodic structure.

3.3 Nanobeam Photonic Crystal Cavity

We have already discussed that in one-dimensional periodic structures, the light propagation in one direction can be blocked. In theory, three-dimensional structures with a high level of index contrast is required to open a “complete band-gap” or a continuum of energies where photons are not allowed to exist inside the photonic material to fully inhibit the emission of photons. The preliminary trials to fabricate a three-dimensional photonic crystal was not promising owing to fabrication complexities; the crystal has several defects. Continuing that was a search for more integrable alternatives that would be easier to implement. The outcome of several research studies resulted in a planar two-dimensional photonic crystal and one-dimensional photonic crystals slabs. These structures maintain a periodic structure in a smaller number of dimensions. However, they use the natural confinement of index contrast in the remaining dimensions. Its desirable for certain applications to have special frequencies propagate within the bandgap, which is realized by carefully adding designed defects in the one-dimensional photonic crystal structure.

In one dimensional segmented waveguide, light trapping was achieved in the system via a combination of Bragg scattering in longitudinal direction and total internal reflection in two transverse directions like the one-dimensional periodic structure, resulting in an optical resonance. For the first photonic crystal nanobeam design, the theoretical value of *Q* was calculated to be 280, whereas the experimentally measured value was 265. Such a low value of *Q* arose from the fabrication imperfections and sub-optimal design, as the defects in the fabrication process induce significant waveguide sidewall roughness, as well as stigmation in the circularity of the holes, and a variation in the width of the waveguide width due to the etching process. Even in a flawless fabrication of similar design, it would not have a high Q due to mode mismatch between the pure waveguide mode and Bloch modes of the photonic crystal as its clear from the calculation results.

Let us consider how light that is launched into a waveguide reacts when it encounters a band-gap. Fig. 3.4(a) illustrates that a substantial amount of scattering occurs. However, if the light is gradually introduced to the photonic crystal, which we can effectuate by tapering it in with smaller holes, then we see that this scattering loss can be eliminated to a great extent. So, light scattering at the interface between the Bragg mirror and the central cavity region is mainly because of the mismatch in the effective mode indices of waveguide and photonic lattice. Therefore, tapering can be viewed as gradually altering the cross-section of the mode, so that the overlap mismatch becomes insignificant. The *Q* values depend strongly on the precise cavity length, which is due to dependence of scattering loss on the cavity length. This can also be considered as an effect for satisfying the Fabry-Perot cavity resonance condition. In this case, high precision fabrication quality for making similar shaped holes is required for the realization of ultra-high *Q* cavities. Similarly, the cavity can be viewed as a wavelength-scale Fabry-Perot cavity with photonic crystal mirrors, which reflects and thus traps the nanobeam waveguide mode as the cavity mode penetrates some distance into the mirror. It is crucial that the fields do not abruptly conclude at the mirror boundary, as this would result in considerable scattering loss. It is necessary to taper the propagating mode of the cavity region into the exponentially decaying mode of the Bragg mirror in order to increase the *Q* of the cavity. This mode matching, analogous to the impedance matching problem in electronics, can be achieved implementing a multi-hole taper towards the cavity [61]. The waveguide effective mode index can slowly be reduced to match the Bragg index by doing so, which significantly diminishes the scattering and provides exponential increase in cavity *Q* at the expense of slight, linear, increase in the cavity mode volume. As an adiabatic taper, near adiabatic conversion between the two modes can be achieved by increasing the number of holes and gradually evolving the modes. The cavity in the photonic crystal is realized by placing two such engineered, tapered mirrors back to back.

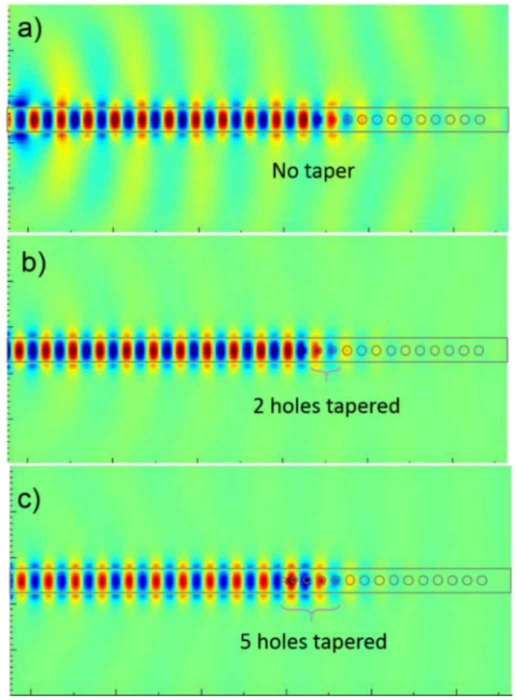

Fig. 3.4. Light scattering at waveguide-mirror interface. Effect of tapering on scattering from photonic crystal. In (a), (b), and (c), a mode is launched from the left toward a photonic crystal. Because of the band-gap this light either scatter or reflect.

Following the mode matching for one-dimension silicon nanobeam cavities, quality factor of nearly 7.5×10^5 is measured at a small mode volume of $V=0.39\ (\lambda/n)^3$ has been demonstrated by detecting the scattered light with a top out plane on a multimode cavity [62]. As Q defines the cycles that are required for the energy stored in the cavity to diminish by a factor of e^{-1}, to achieve higher Q, it is always prudent to have a cavity that has a minimal number of modes to trap. As per the Fourier relationship between time and frequency, this translated as interaction with a large band of frequencies adjacent to the central resonant frequency. Therefore, its desirable to have a single mode cavity to increase the quality factor further. While it is not always advantageous to have an enormous Q for integrated optical communication applications, a Q of at least 10 K is generally preferred.

As previously mentioned, the confinement method is index guiding in the strip waveguide in transverse direction, which is due to total internal reflection. There is a fundamental limit to this confinement. When a given dimension becomes less than $\lambda^2/2n$ in this so called "diffraction limit", the light leaks out with the evanescence tailing the dominant location for the energy. However, one-dimensional or two-dimensional strip photonic crystals can be utilized to develop extremely strong partial band-gaps as long as the diffraction limit is respected. We can create a place where light that would not be allowed to exist in the periodic region can be trapped, in some cases, quite effectively by introducing a point defect or a gradual change in the periodicity of the structure.

Strong coupling requires not only the coupling of light from the waveguide to the photonic nanobeam cavities, but also that the primary channel of coupling be the dominant form of coupling. Several mechanisms interplay when light to enter or exit a photonic nanobeam cavities – in ways such as the scattering loss out of the waveguide into free space or the substrate. Another possibility is absorption loss, where the material of the photonic nanobeam cavity absorbs photons to generate excitons or phonons. The goal is to suppress these non-waveguide loss channels in most cases. In this scenario, any photon entering the cavity from the waveguide will also exit the waveguide and high transmission can be achieved at cavity mode. The scattering and material losses need to be lowered to maintain strong coupling as the waveguide losses are limiting factor to achieve a higher Q. So that at a Q of 10 K, strong coupling can be implemented, but at a higher Q this becomes challenging.

3.4 Design nanobeam photonic bandgap

We need to determine the critical parameters for the application of photonic crystal cavity such as wavelength, the number of resonances in the cavity, or the cavity size, the extinction ratio, and the desired Q depending on the required application. Another particularly interesting point in the design approach is locating the energy of the cavity in the air-band or the dielectric-band. The dielectric band refers to the field confined inside the high index dielectric as suggested by the name, whereas the air-band refers to a significant amount of the mode confined in the low index material. We begin with the width and thickness of the waveguide in order to determine a cavity's resonance. For instance, we used channel waveguide in a 260-*nm*-thick silicon SOI wafer. The width is maintained at 450 nm to satisfy the single-mode limit of waveguide [63]. Subsequently, the hole-radius and periodicity are used to find the band-edge modes. We want to ensure that the frequency of either the air or dielectric bands at the edge of the Brillouin zone are as close as possible to the desired resonance.

Once we have found a suitable hole size, then it merely entails either pulling the dielectric band to higher wavelength through an appropriate taper. This is achieved by reducing the hole radius linearly as one moves away from the center of the nanocavity tapering down. The holes are tapered down over a large distance when an extremely high Q is required. In this cavity, due to long tapering of both sides, the effective size of cavity is large and the cavity becomes multimode [64].

On the other hand, at the expense of reducing the Q factor, a cavity has lesser modes confined in the bandgap if the holes are tapered down in the middle to build the cavity, as the effective length of the cavity is smaller compared to the previous case. The cavity can be considered single mode as the other mode is not fully confined in the cavity. The cavity is composed of five holes tapered down on each side of nanobeam, the transmission and mode profile of single nanobeam cavity is shown in Fig. 3.5.

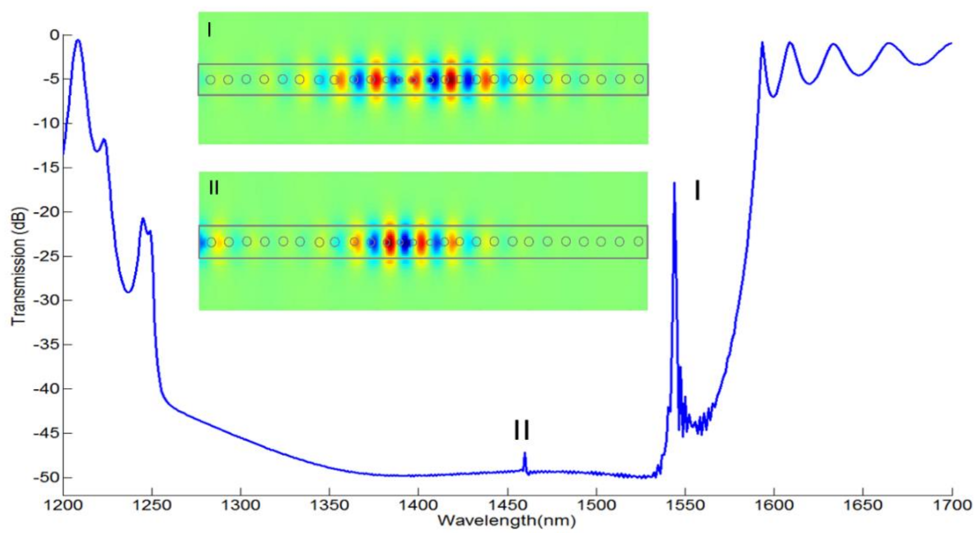

Fig. 3.5. The dielectric band is pulled up into the band-gap by short tapering of hole size in the middle to generate a cavity with λ1= 1543.28 and λ2=1459.29.

3.5 Dual nanobeam photonic crystal cavities

Photonic crystals have introduced abundant opportunities for the manipulation of light. Particularly, photonic crystal nanobeam cavities offer an ideal structure foundation for filtering, switching, and signal routing in optical interconnect applications due to their high-quality factors, small footprint, compatibility to VLSI processing, and scalability [65, 66]. Nanobeams have been incorporated in devices such as photonic crystal nanobeam lasers [67] and LEDs [68] operating at room temperature, electro-optic modulators with comb-like diode structures [69, 70], high sensitivity refractive index sensing [71], all optical switches [72], optomechanics [73, 74], add/drop filter [75], and reconfigurable optical filters [76]. In these devices, nanobeam structures have demonstrated their capability in achieving high Q factors [77] and enhanced light–matter interaction due to their ability to contain photons in wavelength-scale volumes for long optical cycles, which also makes them an intriguing platform for cavity quantum electrodynamics [78].

Dual nanobeams (DNBs) separated by a narrow air slot cause two cavity modes to strongly inter-couple, generating two modes possessing an even and odd symmetry [79, 80]. Accurate control of the mode symmetry and modal wavelength spacing is mandatory in all-optical (Kerr) modulation, filtering, and switching applications. In principle, symmetry shall offer the selection rules that will enable unambiguous separation of modes of different symmetries. Experimentally though, attaining high-purity even and odd modes has been challenging.

However, high-purity modes are required for application in the practical use of nanobeam structures. For example, a typical scheme may employ a pump laser tuned at one mode (e.g. even mode) to modulate or switch to the other mode (e.g. odd mode) in the ultrafast all-optical modulation [81] filtering [82, 83] and switching [84]. An approach for selecting even or odd modes with high purity can be crucial to the device extinction ratio, which is important in all practical applications of optical modulation, switching, and filtering.

3.6 DBR design criteria for nanobeam cavities

Similar to the single nanobeam resonator, the Fabry-Perot resonator in each nanobeam comprises two reflectors or "mirrors". The goal is to design mirrors with high contrast of the resonant mode against the background transmission. There is a trade-off between the quality factor,

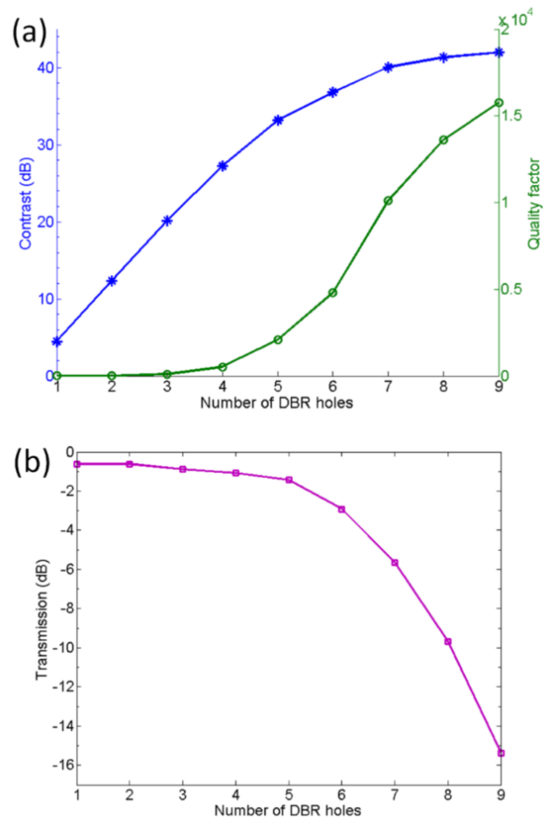

Fig. 3.6. calculated (a) Contrast and Quality factor and (b) Transmission of a 5-hole tapered cavity by the number of DBR holes.

contrast, and transmission of the DNBs. Let us begin with a single nanobeam resonator; the contrast and quality factor for different numbers of DBR holes are calculated based on a simple Fabry-Perot mirror analysis [85] as presented in Fig. 3.6(a). The reflectance for the corresponding mode increases as the number of holes increases, which results in a cavity with higher Q factor and contrast increases. Conversely, it becomes more difficult to couple light into the cavity due to the scattering of imperfect holes and reflection. Thus, the transmission of the defect mode reduces drastically, which is shown in Fig. 3.6(b). Therefore, based on this simple calculation, for a single nanobeam 8 DBR hole is required to have approximately 40 dB contrast and -10 dB transmission for the cavity mode.

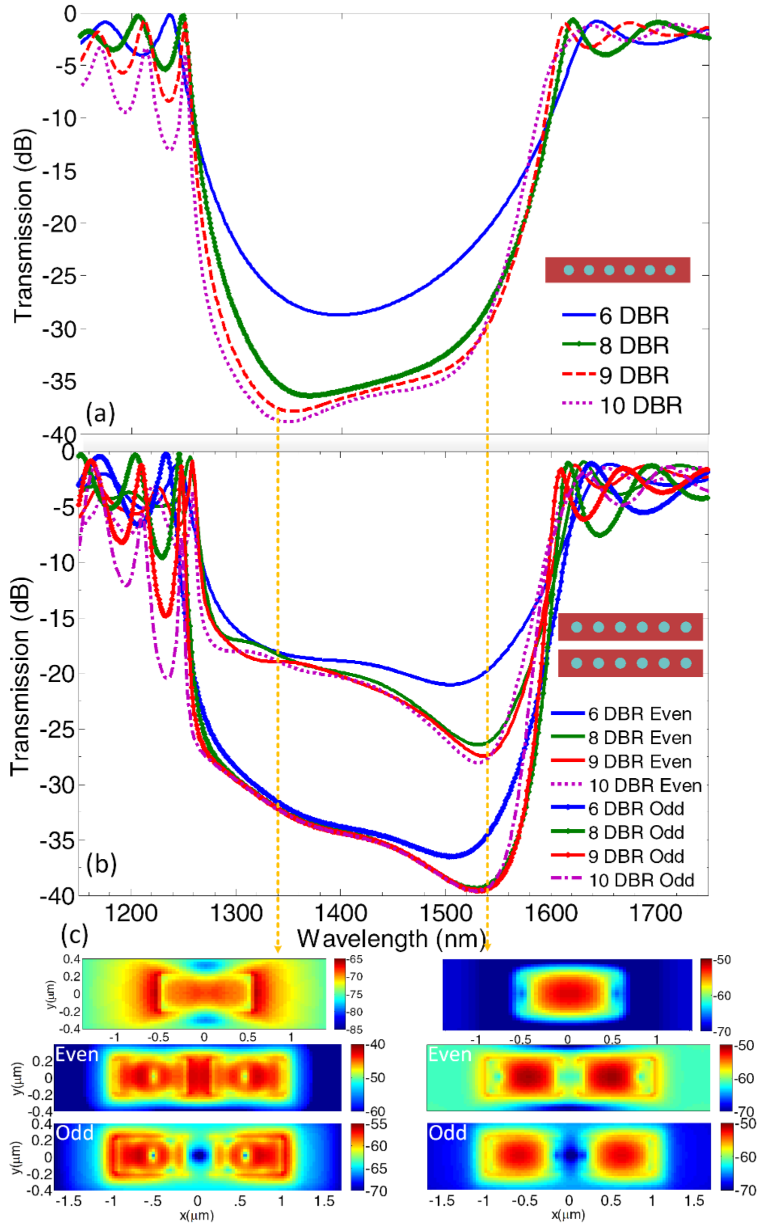

Fig. 3.7. Numerical simulation results for (a) single and (b) dual nanobeam for even and odd modes based on different number of mirror holes. (c) The Poynting vector profile at 1320 nm and 1520 nm shown for single and dual nanobeams for even and odd modes.

This situation is moderately different for dual nanobeam resonators, as in dual nanobeam, due to interaction of the evanescent mode between two resonators, two new resonant frequencies of an even and odd mode emerges [86]. These modes can be excited through mode transforming Mach-Zehnder couplers [87].

For single beams, the reflectance of the corresponding mode in the stop band increases and improves the contrast as the number of holes increases as can be seen in Fig. 3.8(a). This contrast improved more from the air band edge as compared to the dielectric band. The transmission of single and dual nanobeams for different number of DBR holes are calculated and presented in Fig. 3.7(a). This situation is different for DNBs that comprise two similar single nanobeams of the same design. For DNBs, increasing the number of Fabry-perot holes induces a leaky transmission mode near the air band edge; refer to Fig 3.7(b). This leaky transmission in the DNBs can impact the contrast in the stop band in a way such that the contrast reduces from the dielectric band to the air band edge. To comprehend this, we plot the Poynting vector profile at two edges of the stop band for DNBs and single beams for comparison as shown in Fig. 3.7(c). In DNBs, the energy is more confined in the air slot region for an even mode at 1320 nm close to the air band edge, while the energy is held more at the outer interface of DNBs and the air in the odd mode at 1320 nm. While at 1520 nm, for even and odd modes, the energy is confined in the center of DNBs close to the dielectric band edge.

To minimize the effect of this leaky mode, which diminishes the contrast, we designed the cavity in a manner such that it has a resonant mode near the dielectric band – upper edge of stop band. Similar to the single nanobeam, by increasing the number of holes, coupling light into the cavity becomes more difficult due to increased scattering of the imperfect holes. By increasing the number of DBR holes, the transmission of the resonant mode decreases, which eventually diminishes the extinction ration of each resonant mode by reducing the peak transmission versus the background noise. To attain high-purity modes, we need to design mirrors with high contrast of resonant modes against the background transmission. The Q-factor increases as the number of holes increase. However, it becomes increasingly difficult to couple light into the cavity. A moderate number of 26 holes are employed, 9 mirror holes for each side, and 8 tapered holes for the cavity to balance the needs for the large Q-factor and sufficient transmission of the cavity mode.

3.7 Principle of design and fabrication of high extinction ratio DNBs

We created two parallel nanobeams of 450 nm width, each supporting a single TE mode around 1550 nm wavelengths, in a silicon-on-insulator (SOI) wafer to design the structure. The Fabry-Perot resonator in each nanobeam comprises two distributed Bragg reflectors (DBRs) or "mirrors". Each DBR comprises a one-dimensional photonic crystal having holes arrayed to create a stop band around 1550 nm. The photonic crystal mirror pitch, a=360 nm, is linearly tapered over a four-hole section to a=260 nm on each side of the nanobeam center to create a resonant transmission mode at around 1550 nm with a 220-nm-long cavity at the center. The hole radius is given by r=0.25a and a moderate number of 26 holes are employed, 9 mirror holes for each side and 8 tapered holes for the cavity.

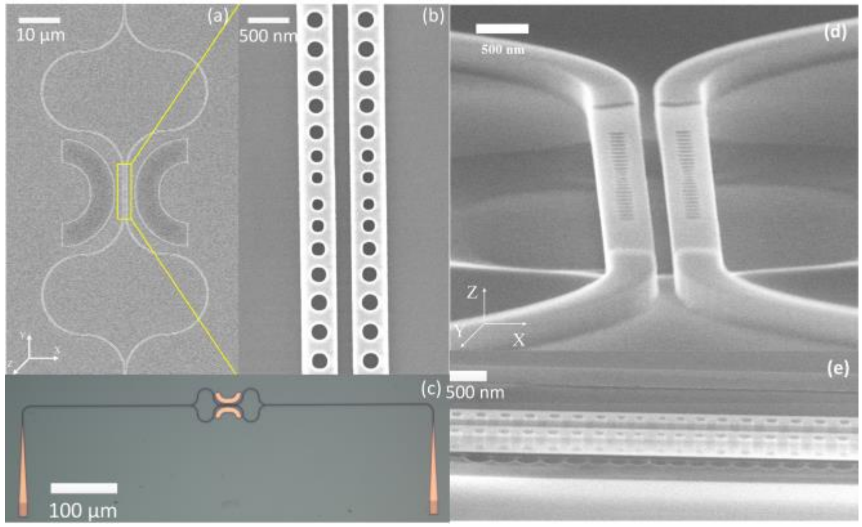

Fig. 3.8. Scanning electron micrographs (SEM) of (a) DNB resonator with mode-symmetry transforming MZCs, and (b) close-up view of the center part of DNB showing tapered hole array with defects/nanocavities at the center. (c) Optical microscope image of the device showing input/output grating couplers and MZCs. (d) Scanning electron micrograph of suspended DNB. (e) Zoomed side view showing the central portion of the DNB with the etched buried oxide (BOX) layer.

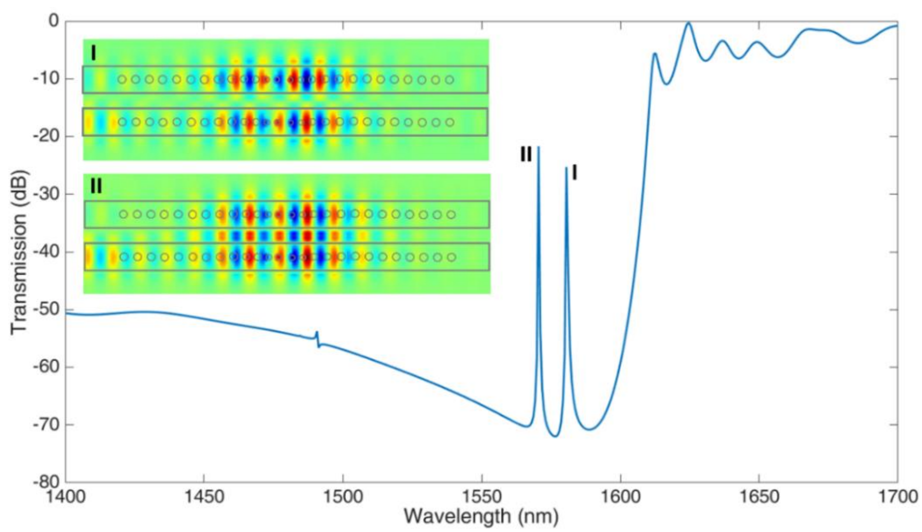

Fig. 3.9. DNB transmission calculated for mixed mode excitation due to coupling between the two nanobeams Even mode with λ=1580.54 and odd mode λ=1570.51 nm

The excitation of symmetrical modes with an even or odd symmetry is based on the design principles for mode symmetry transforming MZCs [87]. The SEM images of the nanobeams and two MZCs are shown in Fig. 3.8(a-c). The nanobeams are suspended, as shown in Fig. 3.8(d-e). Each MZC is a branched Y-junction splitter. We begin with a MZC to excite the even mode of the DNB. Here, we simply design the arms to have a length difference $(\Delta l) = 0$, so there is no phase variation. We set the arms to have a length difference $(\Delta l)_{\pi} = \lambda/2n_{eff}$ for exciting the odd mode, where n_{eff} is the effective index of the silicon wire waveguide at 1550 nm. This induces a phase of π, which excites the odd mode of the DNB.

To excite the mixed-mode or a mixture of even and odd modes, we set the length difference $(\Delta l)_{3\pi/2} = (3/2)\ (\Delta l)_{\pi}$, which induces a phase difference of $3\pi/2$. Numerical simulation applying a 3D finite-difference time-domain method (FDTD) is utilized to ascertain the mode profile and spectral characteristics of even, odd, and mixed modes in the DNB resonator. To verify the designed cavity at the edge of stop band we simulate DNB resonator in mixed mode configuration which is shown in Fig. 3.9. As it shown in the DBR the leaky mode in the stop band is responsible for the increased transmission at lower wavelength, the mode profile of the corresponding modes shown in the inset. The simulation results corresponding to the fabricated DNB resonators for even, odd modes are shown in Fig. 3.10(a) and the mixed mode in Fig. 3.10(b). The different mode profiles for even and odd modes are shown in the inset. Due to the short cavity length (220nm), each nanobeam has only one cavity mode that displays no node (E=0 point) in the cavity. Note that the segments of tapered holes are carefully designed to avoid introducing additional resonant modes. The two modes in the two nanobeams interact to generate even and odd modes. The even mode has a lower frequency and is the fundamental mode.

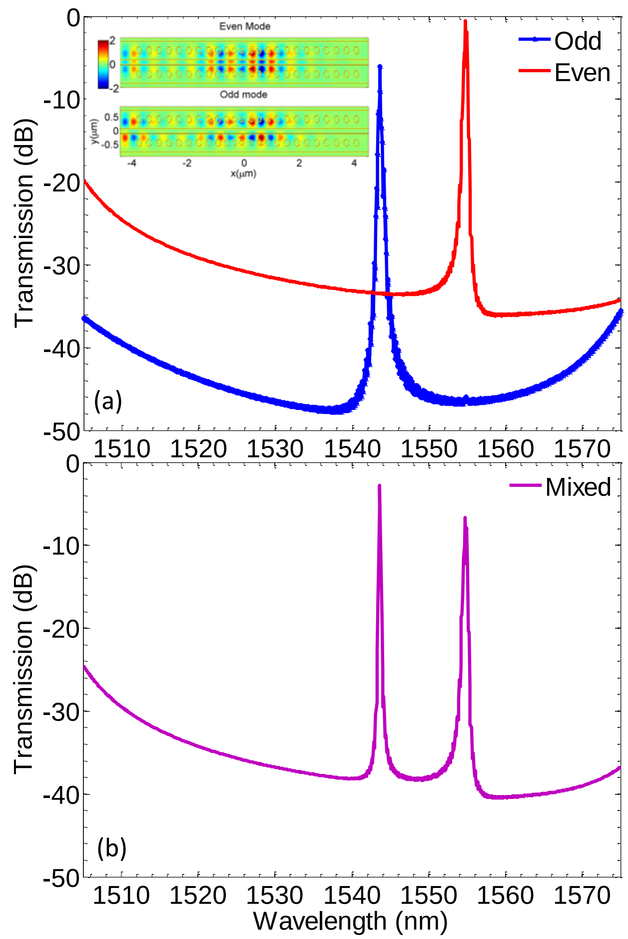

Fig. 3.10. Numerical simulation results of (a) odd and even modes, and (b) mixed modes for nanobeam spacing d=150 nm and cavity length D=220 nm. (inset) The simulated mode profiles for the even and odd modes are shown.

The DNB structure is fabricated on an SOI wafer with a 2 µm buried oxide layer and a 260-nm top silicon layer. It is patterned using a JEOL JBX-6300FS high-resolution e-beam lithography system operating at 100 keV on a 120-nm-thick XR-1541-006 hydrogen-silsesquioxane (HSQ) negative e- beam resist. The pattern is transferred to the silicon layer via an Oxford Plasmalab 100 ICP etcher, utilizing an HBr and Cl_2 based chemistry for vertical and smooth sidewalls. An etching window to define the suspending DNB is patterned via a Karl Seuss MJB-3 optical lithography system on 1.4 µm of a AZ5214E positive photoresist. Through this window,

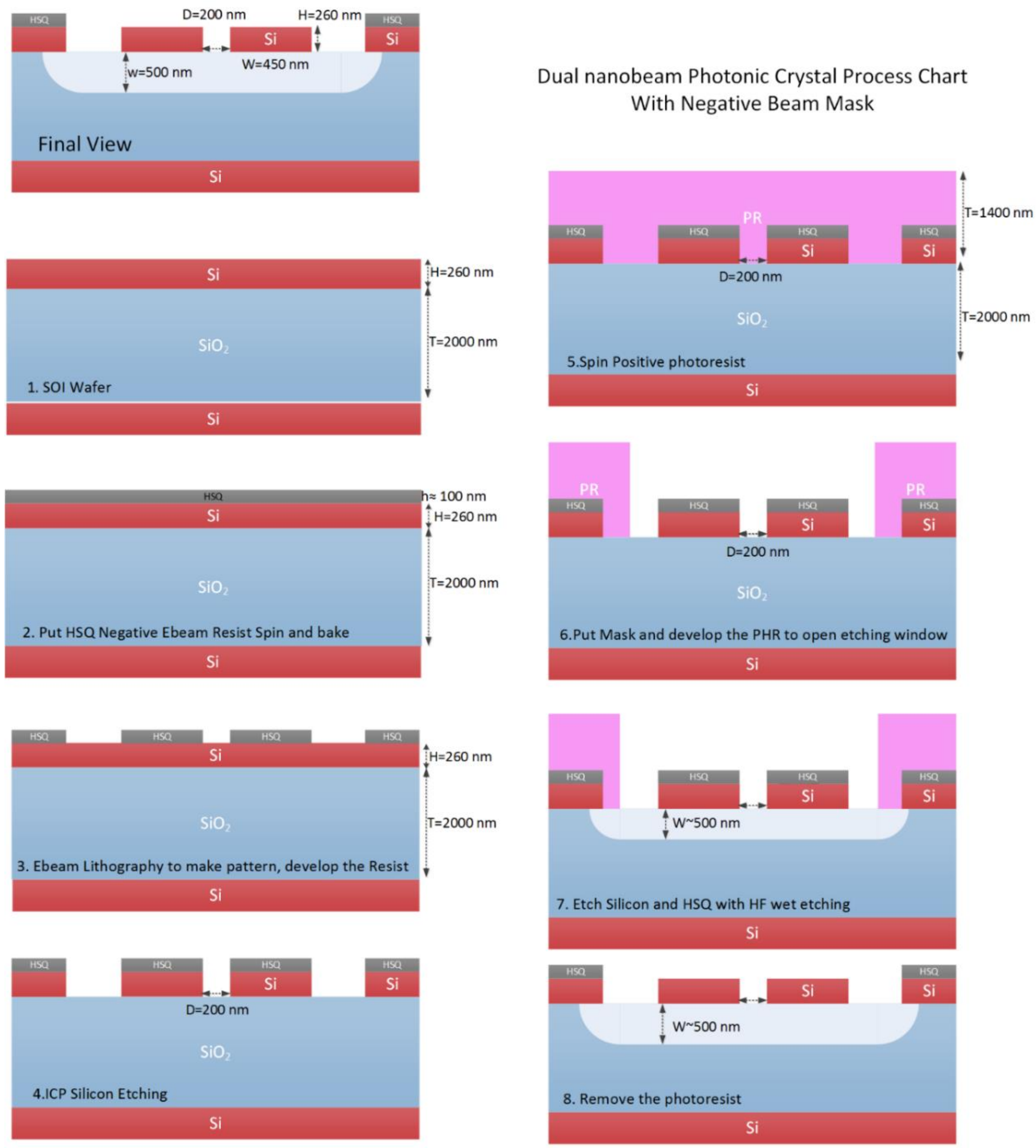

Fig. 3.11. The DNB fabrication process start with SOI wafer and E-beam lithography and etching process. Photolithography is used for doing undercut and etching the BOX layer.

approximately 1 μm of oxide is etched using a buffered oxide etch (BOE) solution. The undercut post processing procedure is shown in Fig. 3.11 and the detail of each step is listed in Appendix A.

We use the surface grating coupler setup that we developed in our lab to measure the transmission spectra of the fabricated DNB. The measurement is performed by coupling TE-polarized light from an HP 8168F tunable laser in which its polarization is controlled by the paddle polarizer controller via a single-mode polarization maintaining (PM) fiber array into sub-wavelength grating couplers that deliver light into the in-plane waveguide structures. The transmission at each wavelength is recorded via an HP 8153 photo-detector controlled through GPIB ports with the MATLAB software. The schematic of the measurement setup is illustrated in Fig. 3.12.

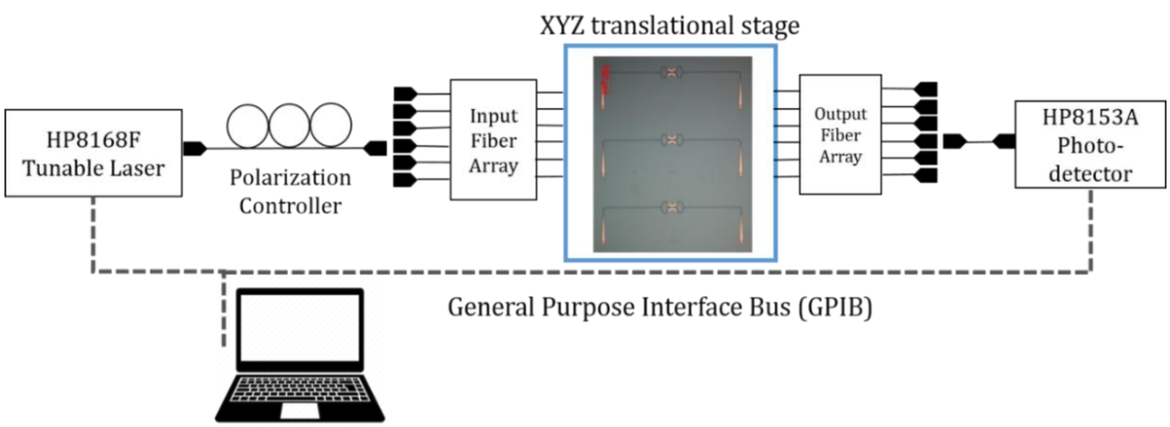

Fig. 3.12. The semi-automated measurement setup which consist of a manual translational stage and a fiber array which transfer the tunable laser source into the chip and receive the light from the device to the detector.

3.8 Measurement results and analysis

The spectra are normalized by the transmission spectrum of a reference waveguide on the same chip with input and output grating couplers after measuring the device. The measured spectral responses for even, odd, and mixed modes for the DNB is presented in Fig. 3.13. Essential features of the modes agree well with simulation outcomes. In these simulations, the wavelength splitting between even and odd mode peaks for the nanobeam spacing $d = 150$ nm is $\Delta\lambda = \lambda_e - \lambda_o = 10.03$ nm, where $\lambda_e = 1552.23$ nm and $\lambda_o = 1542.20$ nm, and quality factor $Q_e \approx 9.7 \times 10^3$ and $Q_o \approx 19.0 \times 10^3$. In the measured devices, we find $\Delta\lambda = 11.2$ nm, where $\lambda_e = 1553.65$ nm and $\lambda_o = 1542.45$ nm, with $Q_e \approx 7.6 \times 10^3$ and $Q_o \approx 12.0 \times 10^3$. The E-field for the even mode as seen in the inset in Fig. 3.12 penetrates substantially into the central air gap, which directly connects to the surrounding air and tends to leak light. This may diminish the Q factor. In contrast, the E-field of the odd mode is restricted largely in silicon nanobeams. Light is less probable to leak out to the air and the quality factor is higher, as the light tends to stay in higher index materials. The measured Q-factors are lower than the simulation results due to the scattering caused by sidewall roughness for the waveguides and holes as well as light loss from other structural imperfections (e.g. not perfectly vertical sidewalls). The contrast of the selected modes versus the background or undesired modes is significantly high. For the even mode excitation given by the red curve in Fig. 3.13(a), the contrast against the background is approximately 30.9 dB. For the odd mode excitation given by the blue curve in Fig. 3.13(a), the contrast of the odd mode against the background is approximately 31.2 dB and over the residual even mode is around 27.8 dB, which is reasonably high compared to photonic crystal resonators [83] and is also comparable to ring resonators.

To analyze the dependence of peak wavelengths of two modes on the nanobeam spacing *d*, we examined the spectral characteristics of mixed-mode excitation with varied nanobeam spacing. As illustrated in Fig. 3.14, the general trend is that $\Delta\lambda$ decreases as the nanobeam spacing increases. The evanescent fields of nanobeams have less coupling as they further separate from each other, therefore reducing the wavelength splitting due to their coupling. Note that as the spacing *d* increases, both λ_e and λ_o decrease. According to the fundamental electromagnetic theory, decrease of the mode wavelength implies that the field moves further into the low-index region (air slot in this case). For the even mode, a substantial portion of the field is in the slot (see Fig. 3.14 (a) inset). The portion of the field in the slot increases substantially as the slot width increases, so the decreasing trend of λ_e is significantly strong. For the odd mode, only a minute portion of the field

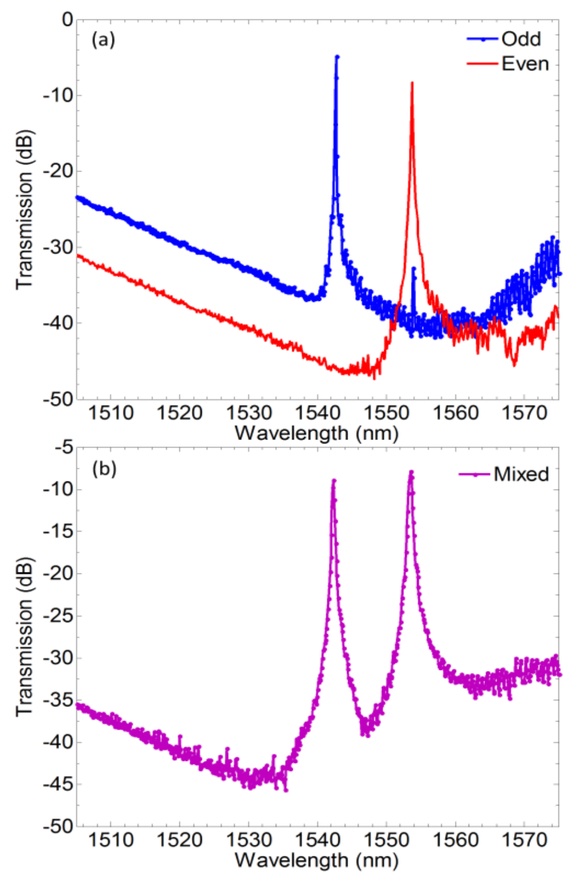

Fig. 3.13. Experimental measured spectra of (a) odd and even modes, and (b) mixed modes for nanobeam spacing d=150 nm and cavity length D=220 nm.

is in the slot, because the field must vanish at the slot center line. The decreasing trend of λ_o is very weak. Additionally, fabrication processes tend to create small variations in the hole sizes between various structures. The peak wavelengths of the modes should vary more smoothly with the spacing d without this non-ideal effect. We have extracted the actual shapes of the holes and nanobeams from SEM micrographs and simulated this actual shape to obtain the simulated peak wavelengths to verify that the fluctuation of the peak wavelengths with d is due to small variations of hole sizes, which is provided in Fig. 3.14(b). The simulated results agree fairly well with the experimental results, reflecting similar fluctuation in the peak wavelengths. Small discrepancies remain between the simulated resonant wavelengths and the measured values in Fig. 3.14(b). These are attributed to the random sidewall roughness.

In Fig. 3.14(c), the peak wavelength divisions obtained from experiments are compared with the peak wavelengths separation of the ideal design (assuming all structures have the same set of hole sizes but varying separation). One finds that the difference $\Delta\lambda$ remains close to the ideal design value even though the variation of hole sizes in fabricated structures tends to cause noticeable fluctuations of the λ_e and λ_o from the ideal values. This may be useful in some applications where the device performance depends heavily on the wavelength separation but is relatively insensitive to small wavelength variation of each mode.

The high contrast of modes against the background and the undesired mode obtained here is crucial for the practical use of nanobeam devices in all-optical modulation/switching and filtering applications. For example, practical applications in a pump-probe configuration often require blocking the relatively high-power pump light and keep the probe signal only at the output, where the pump and probe lasers couple toward the even and odd modes respectively (through a mixed-mode MZC at input, for example). A high-purity odd mode MZC is crucial to practical devices in this case. It is possible to further increase the number of holes in the DBR to further suppress the background transmission and increase the quality factor of the cavity. However, scattering loss due

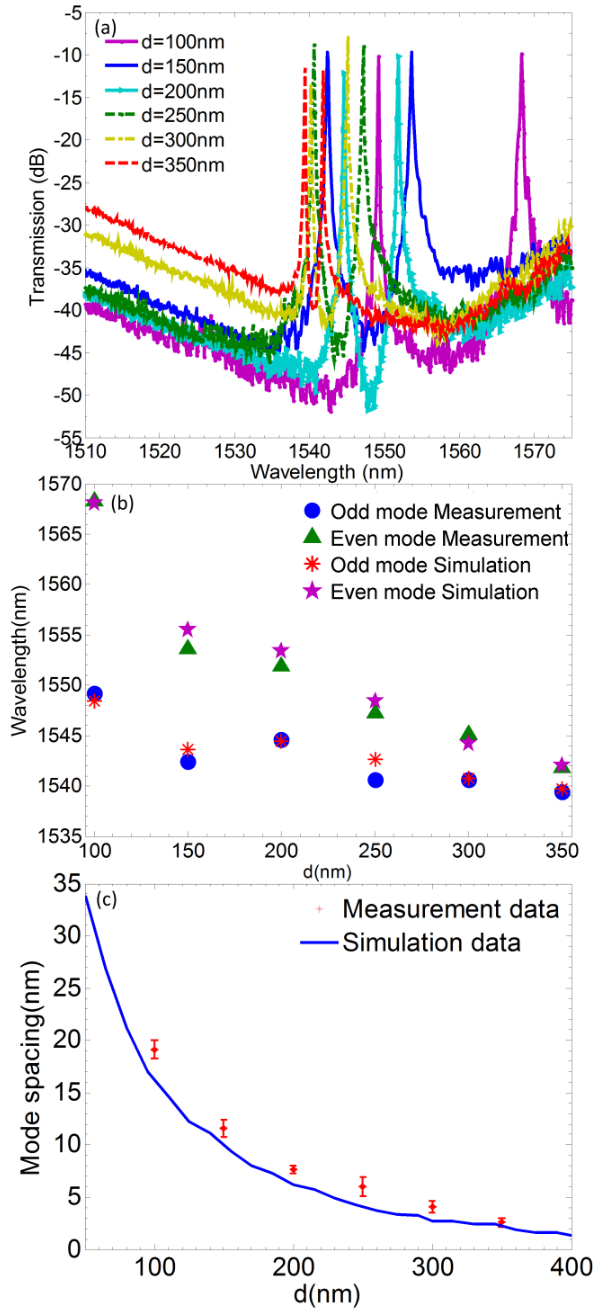

Fig. 3.14. (a) Measurements of mixed-mode excitations in different slot spacing configurations, showing the trend of bimodal response as the nanobeam spacing between nanobeams increases. (b) measurement and simulation results of resonant wavelength for even and odd mode. The structures used in the simulation are extracted from the SEM images of fabricated structures. (c) mode spacing for different nanobeam spacing.

to small structural imperfections (e.g. roughness) increases as the number of holes increase, which decreases the peak transmission of the cavity mode. Note that each DBR is essentially a one-dimensional photonic crystal waveguide. In such a waveguide, the loss is enhanced by the slow light effect [87].

For a specific application scenario, the number of holes in the DBR is determined by the trade-off between the peak transmission and other parameters, including the quality factor and background transmission. Minute asymmetry always exists in fabricated devices between two nanobeams and between two arms of the MZC due to structural imperfection (e.g. sidewall roughness) arising from fabrication processes. This can effectuate the phases, mode profiles, and other characteristics of two nanobeams or MZC arms to slightly digress from the design. Such digressions are random (causing weak unbalance between two nanobeams) and may be distributed over many parts (e.g. over every hole of the nanobeams). This can sometimes engender a very weak residual mode of the opposite symmetry [refer to Fig. 3.13(a)]. The insertion loss of the resonant modes in Fig. 3.13 can be contributed toward by the scattering loss due to sidewall roughness of the outer nanobeam edges and holes and by the small insertion loss of the Mach-Zehnder coupler. The former is subjected to some fluctuations due to the non-specific nature of roughness. Small fluctuations of input/output grating coupler loss may also moderately affect the loss shown in Fig. 3.13. The background transmission under 1530nm increases as the wavelength decreases. Generally, as the wavelength λ decreases, an optical mode tends to have large shares of its field moving into the lower-index region. Here, as λ decreases, the modes responsible for background transmission will penetrate further into the slot. Photonic crystal holes are less effective in blocking light within the slot as they do not extend into the slot. This contributes to the increase of background transmission at short wavelengths.

Note that the two-photon absorption and free carrier generation effects are negligible as the laser employed in our measurements has a low power (30 µW). Therefore, the thermo-optic effect due to free carrier generation may also be neglected. The low power also reduces any optomechanical effects. In this work, the *Q*-factor refers to the total *Q*-factor, which includes the effect of coupling to the waveguides. Note that the inter-coupling of two nanobeams causes even and odd mode fields to restructure around the slot. The fields at the two outside edges (and outside air-cladding) face very little perturbation due to inter-coupling. The fields there have almost identical magnitudes (opposite sign) for the even and odd modes. Their contributions to the *Q*-factor also present little difference. Scattering loss due to sidewall roughness is generally lower than the other losses of the resonator with careful fabrication, hence it imposes a reasonably weak effect on *Q*.

3.9 Conclusion

We have demonstrated an approach toward designing high contrast dual nanobeam mode symmetry filter by controlling the cavity mode and DBRs. The side coupling scheme is used for precise control of the mode symmetry in DNB resonator structures utilizing mode symmetry transforming MZCs that allow us to excite modes separately into even, odd, or a mixture of the two modes. We measured 30.9 dB for the even mode and 31.2 dB for the odd mode contrast against the background.

Chapter 4. Mode coupling and mode converters

4.1 Introduction

In photonic chips, the combination of different waveguide types varying both in geometry and in guiding principle can coexist. A possible example of the coexistence of various waveguide types is the use of photonic crystal waveguides which enables sharp lossless bends besides TIR waveguides for the stretches between these bends. Different waveguide geometries can appear together when a monomodal wire is applied in a bend, but somewhat broader multimodal waveguides, having less loss, in the delay lines or connection lines of a photonic chip or using different waveguide width for multiplexing purpose as mode division multiplexing scheme. But also in the connection of an optical chip to the outside world, light modes with different sizes and geometries have to be coupled, like as mentioned in the second chapter the coupling between an optical fiber and a planar waveguide or between a semiconductor laser diode and a planar waveguide.

Generally, tapers classified in two categories of adiabatic, or lossless, and nonadiabatic which induce attenuation to the optical mode during the mode conversion process. To couple optical waveguides with different cross sections and different modal sizes, smooth linear taper can be used [89]. However, in order to become adiabatic or lossless, these tapers need to be sufficiently long. The taper profile can impact the insertion loss, for regular adiabatic tapers parabola is the best shape. The minimum taper length needed for adiabatic operation has been calculated by the ray model with the following relation [107]:

$$L = \frac{(w_L^2 - w_0^2) \times n_{core}}{2\alpha\lambda_0} \tag{4.1}$$

In which W_L is width if the wider waveguide and W_0 is the width of narrow waveguide and α is a factor which is less than one. The derivation of this formula shown at Appendix B. So assuming the light is coupling from the 9 µm wide waveguide into single mode waveguide with w=450 nm (with 20:1 ratio) at least a parabolic taper profile of 90 µm length is required. In more realistic adiabatic taper (α=0.7) this length is around 140 µm, these calculations shown in Fig. 4.1.

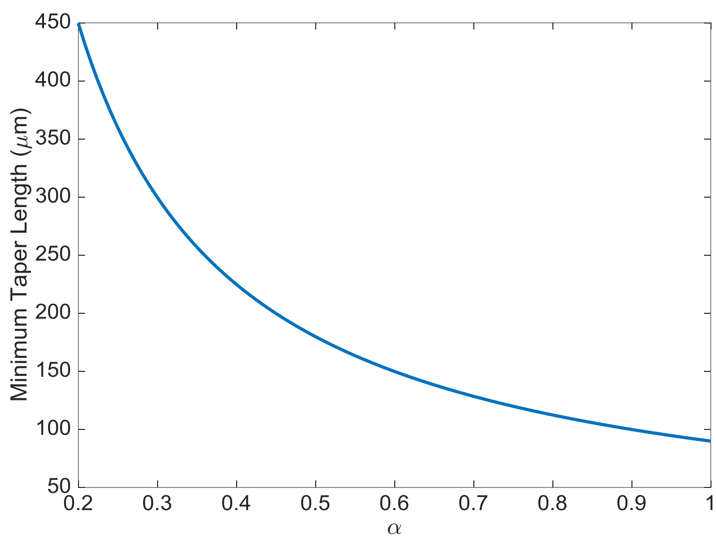

Fig. 4.1. Minimum adiabatic taper with parabolic profile for coupling between 9 µm wide waveguide and 450 nm for different α.

Compact Beam Expanders (BE) are essential components in integrated photonics. They are widely used in matching the modes, shaping the wavefront of waveguides of different widths [90,91]. Simply spreading optical power of waveguide modes from a narrow waveguide to a wider waveguide can be readily achieved through certain taper shapes if one does not care about the higher-order modes excited in the process. However, many applications require that the width transformation to preserve the light in the lowest order mode after the transition. Furthermore, the recent trend of silicon photonics towards ultra-compact devices demands such mode-order-preserving width expansion to be completed in an ultra-short distance. Generally, such mode-order-preserving expansion requires a very slow or adiabatic taper with a length substantially larger than the final width of the waveguide. It has been challenging to reach 1:1 ratio for the expansion length and the final width. To couple optical waveguides with different cross sections and modal sizes, slowly varying linear or parabolic tapers can be used. However, in order to minimize the loss and satisfy the adiabatic taper condition, the taper length has to be sufficiently long ($L_{taper} > 70\ \lambda_0$), which is greater than the mode beating length satisfied by the parabolic slowly varying taper [89]. In non-adiabatic short tapers ($35\ \lambda_0 < L_{taper} < 70\ \lambda_0$) the power from the fundamental mode substantially couples to the second order mode. Whereas, in the rapidly varying taper ($L_{taper} < 35\ \lambda_0$) the input power can couple not only to second but also to higher order modes increasing the insertion loss exponentially regardless of the taper profile. The insertion loss of the rapidly varying tapers (20:1 waveguide width ratio) with linear, parabolic, exponential and Gaussian profiles are shown for 1550 nm wavelength in Fig. 4.2. It is observed that in nondiabetic regime the parabolic taper is not acting as efficient taper profile compared to linear and exponential tapers. In nonadiabatic tapers, the rapidly varying sidewalls, causes multiple scattering and coupling of light to higher order modes, which consequently decreases the power delivered to the fundamental mode. This effect is strongly related to the taper length which affect the wavefront shape and doesn't depend strongly on the wavelength. In integrated photonic circuits, every component should be designed in a way to reduce the material, processing, and packaging costs. Therefore, shorter innovative coupler designs are needed.

Optical tapers can be used to mediate the modes between different waveguide width. From their geometry tapers can be roughly divided in two major groups of planar tapers (2D) [92, 93] and three-dimensional (3D) tapers [94, 95]. Where the former have to change a spot geometry in two dimensions, like transforming a circular mode into a rectangular one, the latter only changes the spot size in one direction, for example coupling between the narrow and the broad planar waveguides. In lateral tapers, the width of the guiding layer is changed. These tapers are easy to fabricate, but the disadvantage is that they need a sharp termination point of the upper waveguide, making the process complicated. In vertical tapers, the thickness of the guiding layer is altered along the (length of the) device, however, the application of theses tapers is limited due to the critical variations of the thickness.

The planar mode size converters can be classified into multimode interference (MMI) based mode size converters [96], segmented tapers [97-99], and photonic crystals [100]. Mode size converters based on MMI excite several modes, and the waveguide is terminated in such a way that interference between these multiple modes yields to maximum coupling. Although, these classes of mode size converters are much shorter, they are less flexible and only allow a limited expansion of the spot size. The segmented tapers are similar to MMI mode size converters, but instead they are optimized based on each segment length. Although they are more flexible compared to MMI mode size converters, they have limited expansion and suffer from low fabrication tolerances.

Photonic crystal spot size converters can be relatively short and efficient but they have relatively low bandwidth [101]. Non-adiabatic mode size converters have been studied in shallow etched lens-assisted focusing taper which has 1 dB loss for TE mode in 20-μm-long taper [102]. By using genetic algorithm (GA) optimization [103] 1.4 dB loss for 15.4 μm-long taper for 18:1 waveguide width ratio has been demonstrated [104]. Also, a segmented-stepwise mode-size converter designed via particle swarm optimization (PSO) for a 20-μm-long taper demonstrated -0.62 dB loss for 24:1 waveguide width ratio [105]. The idea in the optimized mode converters is to divide the taper length into digitized segments and maximize the coupling to the end waveguide. The transformation optics approach has also been used to design reflection-less tapers [106, 107].

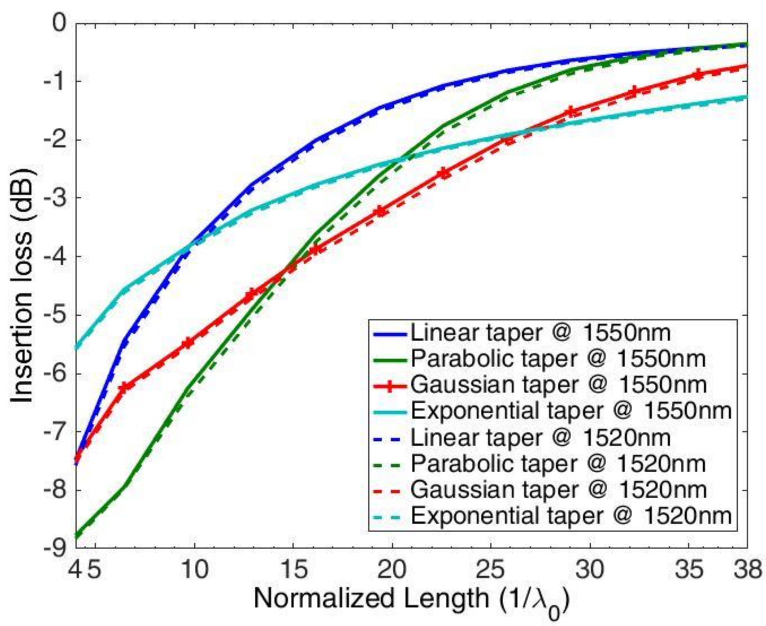

Fig. 4.2. Transmission efficiency for non-adiabatic linear and parabolic, Gaussian and exponential taper profiles with a waveguide width ratio of 20:1 at two different wavelengths.

4.2 Design Integrated lens structures

In free space optics, laser beam expander is designed to increase the diameter of a collimated input beam to a larger collimated output beam. With similar analogy, optical telescopes, which have been used in free space optic to view distant objects such as celestial bodies in outer space, one of these refractive telescope is a Galilean telescope which consists of a positive lens and a negative lens that are also separated by the sum of their focal length which is shown in Fig. 4.3(a) the idea of Galilean telescope can be adopted to design integrated beam expander/ focuser as shown in Fig. 4.3(b) in which the taper section play the role of the negative lens, and the planar sub-lens structure works a s a positive lens in Galilean telescope.

So the challenge of designing a compact, efficient beam expander is translated into finding a proper taper and an integrated sub-wavelength planar lens structure. There has been lots of effort dedicated on designing aberration free focusing planar lens structure as well as integrating a planar waveguide with a vertical lens such as Luneberg lens [108]. The Luneburg lens is a rotationally symmetric thick lens with a spatially varying refractive-index profile that focuses light on the rim of the lens. The focal point lies in the direction of the incident light; the lens thus turns the direction of a light ray into the position of the focus. Our goal was to design a refractive index in planar waveguide by using photonic crystals in such a way that the effective index of the structure provides the luneberg lens profile. The effective index profile of a Luneburg lens with the radius a can be expresses as:

$$n(\mathrm{r}) = \sqrt{2-(r/a)^2} \quad for \;\; r \le a \tag{4.2}$$

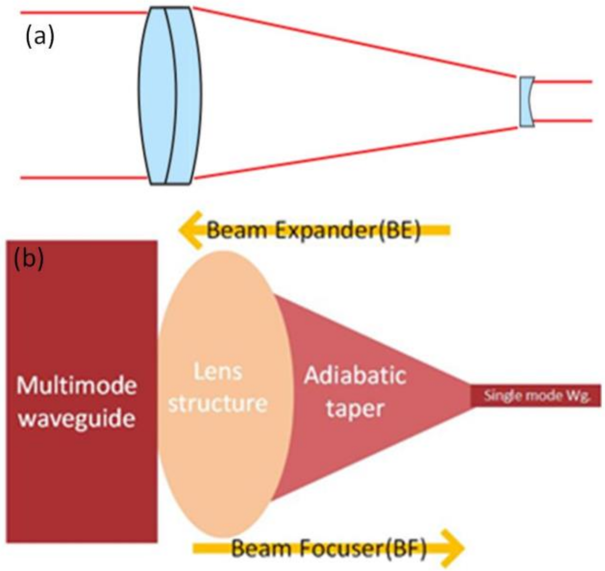

Fig. 4.3. Schematic of a (a) Galilean telescope with the red lines as light rays and (b) the integrated Beam Expander/Focuser

The Luneberg lens profile is implemented by adding radial through holes with different radius on a 5 µm diameter waveguide, followed by a 3 µm length taper structure we designed a beam expander, shown in Fig. 4.2. This beam expander converts the mode from the 9 um wide waveguide to 450 nm waveguide width within 8 µm length. The device schematic and the E-filed distribution has been shown in Fig. 4.4.

From the E-filed schematic it's clear that the diffracted light at the end of the planar circular Luneberg lens. The coupling efficiency of less than 50% which is due to reflection at the interface between taper and the lens structure as well as the lens and the output waveguide. The Fabry-Perot induced reflections cause 10% ripples in the transmission spectra (Fig. 4.5). Also, diffraction and coupling to higher order modes contribute partly in reducing the transmission. For very short nonadiabatic taper the Luneberg lens couldn't effectively convert the mode from the taper to the wide waveguide.

In 1951 A.L. Mikaelian proposed a gradient structure whose refraction index changes with the radius in the form of a hyperbolic secant [109]. This structure is widely used in information optics due to its focusing effect and is called Mikaelian's lens. Many studies have been made on ML's focusing properties [110]. Mikaelian's lens can be used as a coupler between waveguides. The gradient Mikaelian lens operates by focusing all the rays parallel to the optical axis and incident perpendicularly to its plane surface in a point on the opposite plane surface. We have incorporated a 3 μm long mikaelain lens. The refractive index of such an axisymmetric gradient lens is related to the radial coordinate (r) as

$$n(\mathrm{r}) = n_0 \left[\cosh\left(\frac{\pi r}{2L} \right) \right]^{-1} \tag{4.3}$$

where n_0 is the refractive index on the optical axis and L is the lens thickness along the optical axis. To make this refractive index we circular PHCs in which their radius is varied in the radial direction. After optimizing the profile for such a 5 μm long taper and a 3 μm lens structure shown in Fig. 4.6(a) we use 3D FDTD to simulate the electric filed profile shown in Fig. 4.6(b). The E-filed profile shows less diffraction compare to Luneberg PHC lens structure and less back reflection which enables this beam expander to have higher transmission up to 70% and less than 8% ripples (Fig. 4.7). Compare to Luneberg lens the new beam expander could convert the mode with less reflection but still the diffraction pattern is clear at the wide waveguide which shows coupling to higher order modes.

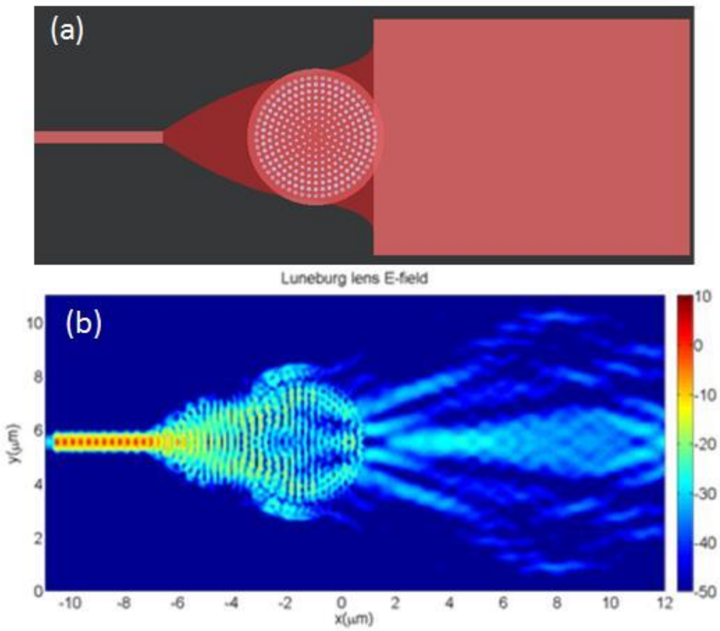

Fig. 4.4. The schematic of (a) beam expander with integrated Luneberg PHC lens (b) E-filed profile at 1550 nm wavelength

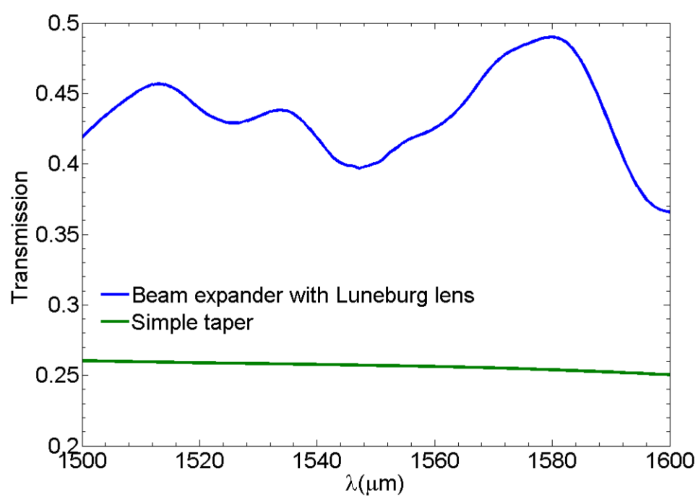

Fig. 4.5. Transmission efficiency of a beam expander with Luneburg PHC lens compared with linear taper of the same length.

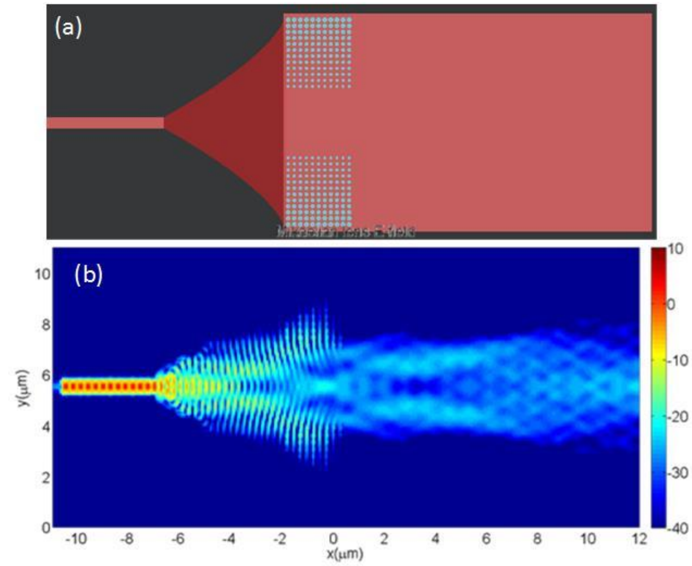

Fig. 4.6. The schematic of (a) beam expander with integrated Mikaeleian PHC lens (b) E-filed profile at 1550 nm wavelength

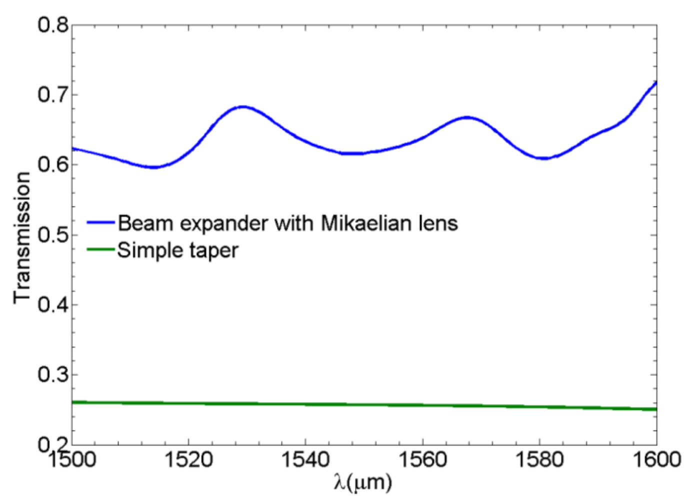

Fig. 4.7. Transmission efficiency of a beam expander with Mikaelian PHC lens compared with linear taper of the same length.

4.3 Optimized waveguide mode converter

By the analogy from Galilean telescope, the low loss, beam expander (BE) is composed of an integrated lens structure as well as a taper which need to be designed concurrently. We have applied an evolutionary optimization procedure, in combination with 3D FDTD for calculating the optimal structures. Most of evolutionary techniques have the following procedure [111]:

1. Random generation of an initial population

2. Reckoning of a fitness value for each subject. It will directly depend on the distance to the optimum.

3. Reproduction of the population based on fitness values.

4. If requirements are met, then stop. Otherwise go back to 2.

Particle swarm optimization (PSO) showed a great capability in optimizing critical passive devices with like Y-junction couplers [112] compared to other methods such as junction matrix method [113] or GA optimization [98]. PSO shares many common points with GA. Both algorithms start with a group of a randomly generated population, both have fitness values to evaluate the population. Both update the population and search for the optimum with random techniques. And both systems do not guarantee success on finding the optimal point. However, PSO does not have genetic operators like crossover and mutation. Particles update themselves with the internal velocity. They also have memory, which is important to the algorithm. Compared with genetic algorithms (GAs), the information sharing mechanism in PSO is significantly different. In GAs, chromosomes share information with each other. So the whole population moves like a one group towards an optimal area. In PSO, only the best generation gives out the information to others and it is a one-way information sharing mechanism which only looks for the best solution. Compared with GA, all the particles tend to converge to the best solution quickly even in the local version in most cases. Particle swarm optimization algorithm has this three following advantages:

- PSO have no overlapping and mutation calculation. The search can be carried out by the speed of the particle. During the development of several generations, only the most optimist particle can transmit information onto the other particles, and the speed of the researching is very fast.

-The calculation in PSO is very simple. Compared with the other developing calculations, it occupies the bigger optimization ability and it can be completed easily.

- PSO adopts the real number code, and it is decided directly by the solution. The number of the dimension is equal to the constant of the solution.

To design the taper and lens structures with PSO algorithm we divide the taper and semi-lens section into multiple segments in which each segment has a smooth curvature with discontinuities at the boundaries between each segment. Numerical exploration for finding the best profile fit for our criteria confirmed a structure which consists of a rapid taper and semi-lens structures. When a beam propagates through rapid varying tapers, the wavefront get distorted due to the interaction from sidewall reflections. Any deviation from wavefront propagation determined by ideally shaped components may be called scattering. In terms of waveguide modes, this wave-front deformation is considered to cause coupling to other modes. Therefore, the deformed beam is described as a superposition of the fundamental mode and higher-order modes [114]. Correcting the ripples in the wavefront can reduce the scattering as well as coupling to the higher order modes. To optimize the structure, we aim to increase the coupling to the end waveguide by reducing wavefront deformation, which can improve the sphericity of the wavefront and correct the aberration [115].

This type of semi-lens structure is known as an aspheric lens [116]. The geometry of each segment is defined through the following relation

$$w_i(x_i) = (w_i - w_{i+1})\left|\frac{x_i - L_i}{L_i}\right|^{m_i} + w_{i+1} \tag{4.4}$$

In which w_i , L_i , m_i are the width, length and curvature of the i^{th} segment and $x_i = x - \sum_{i=1}^{j-1} L_j, i = 1, 2....6$. The curvature ($m_i \geq 0$) provides the freedom inside each segment to make either linear convex or concave sidewalls. We optimized the BE design with 6 segments, corresponding to a total of 18 parameters.

The first attempt to design BE the segment the six sections length set to be constant and the total length of BE optimized for 8 µm.

After coupler of iterations the Beam Expander profile is shaped as Fig. 4.8(a) which if we look through it from left to right has an input taper, lens structure and an output inverse taper. The output inverse taper is critical as it reduce reflection from mode transition to the wider waveguide.

The e-filed profile of the beam expander shows focusing the mode in the center waveguide and shows much less diffraction (Fig. 4.8(b)) compared to the linear taper of the same length (Fig. 4.8(c)). By reducing the diffraction and reflection effects the design Beam Expander transmission average is 82% with less than 4% ripple in the spectra (Fig. 4.8(c)).

In attempt to reduce the backscattering and loss due to coupling to higher order modes, the power delivered to the fundamental TE mode of the output waveguide is optimized in such a way that the width of each section in beam expander is optimized as well. The calculations are done by finding the average of the overlap integral over 1520 nm to 1570 nm bandwidth range. The design parameters for BE are listed in Table 4.1.

Table 4.1. Design parameters for different BEs

Parameters	Values
m_1, m_2, m_3, m_4, m_5, m_6	3, 1.1,0.01, 3, 0.32, 2.55
W_1, W_2,W_3, W_4, W_5, W_6	1.7, 3.3,9.06, 10, 3.19, 9
L_1, L_2, L_3, L_4, L_5, , L_6	1.0, 3.61, 0.05, 0.7, 3.11, 1.03

For the 9.5 µm long optimized BE design, the average -0.85 dB insertion loss has been calculated for the wavelength range displayed in Fig. 4.10. The 0.5dB bandwidth of the transmission spectrum is 69nm. Linear taper with the same length has -3.9 dB insertion loss shown for comparison. In the optimized design, the first half of the BE's length works as a rapid taper and the rest as the semi-lens. To demonstrate the improvement in the wavefront deformation and correction of the optimized BE comparing to the linear taper, the amplitude and the phase of the E_y field profile are displayed in Fig. 4.11. In the BE, [Fig. 4.11(a)] the ripples of the amplitude profile diminish after propagation through the semi-lens creating a flattened wavefront in the phase plot [Fig. 4.11(c)]. However, in a linear taper with the same length [Fig. 4.11(b)], due to scattering, the amplitude profile is more distorted. This distortion expands through propagation, thus, the phase exhibits a curved wavefront [Fig. 4.11(d)], implying coupling to higher order modes and loss.

The shape of the sub-lens is critical in flattening the wavefront. In case the structure is not designed precisely the semi-lens cannot correct the wavefront effectively and light may couple to higher order modes, as well as the fundamental mode, affecting the device

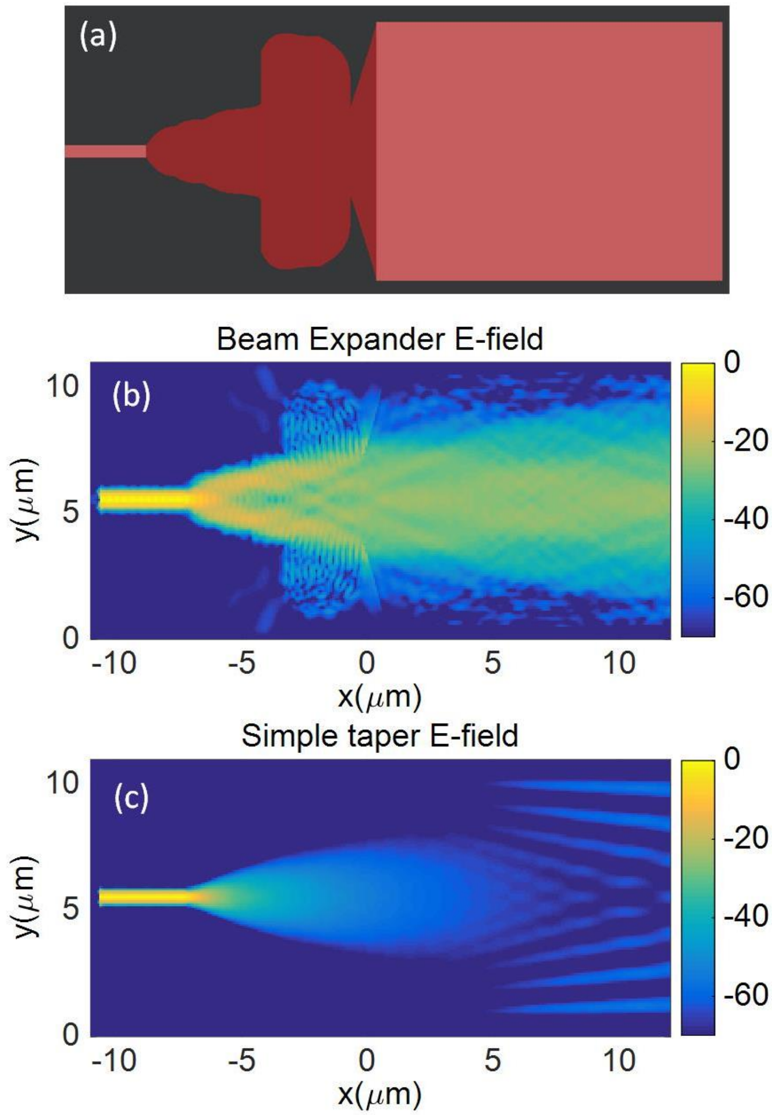

Fig. 4.8. (a) Schematic for an optimized 8 µm BE (b) E-filed profile of the structure at 1550 nm wavelength (c) E-field profile of the linear taper shown for comparison the diffraction pattern of the linear taper is clear.

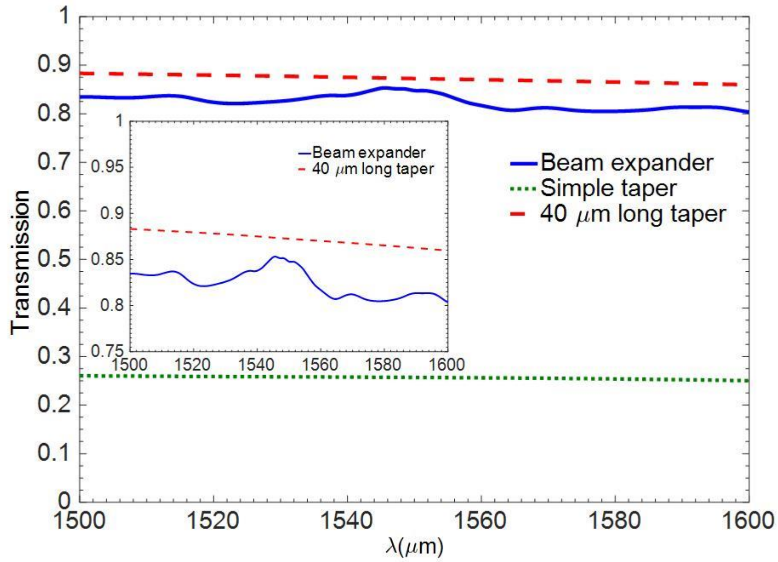

Fig. 4.9. The insertion loss for the 8 μm BE compare to the linear taper of the same length and 40 μm taper has 3% ripples which shown in the inset.

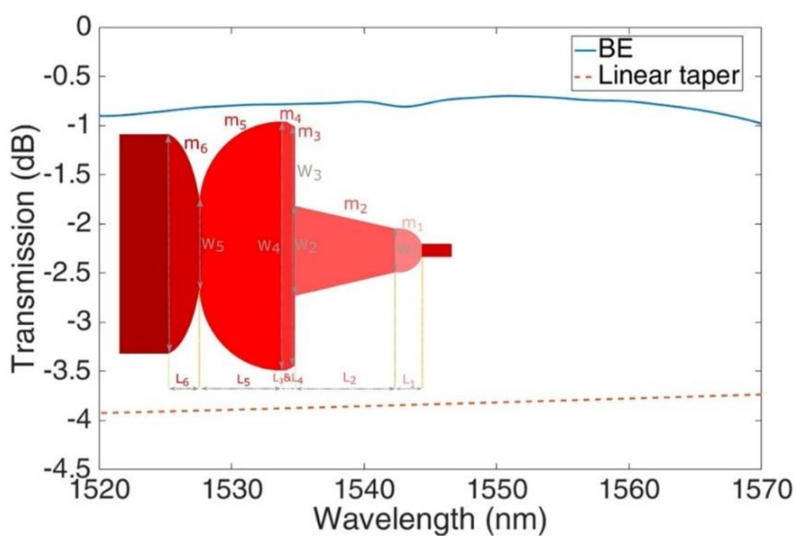

Fig. 4.10. Transmission calculated for the BE and a linear taper with the same length and waveguide width ratio of 20:1.

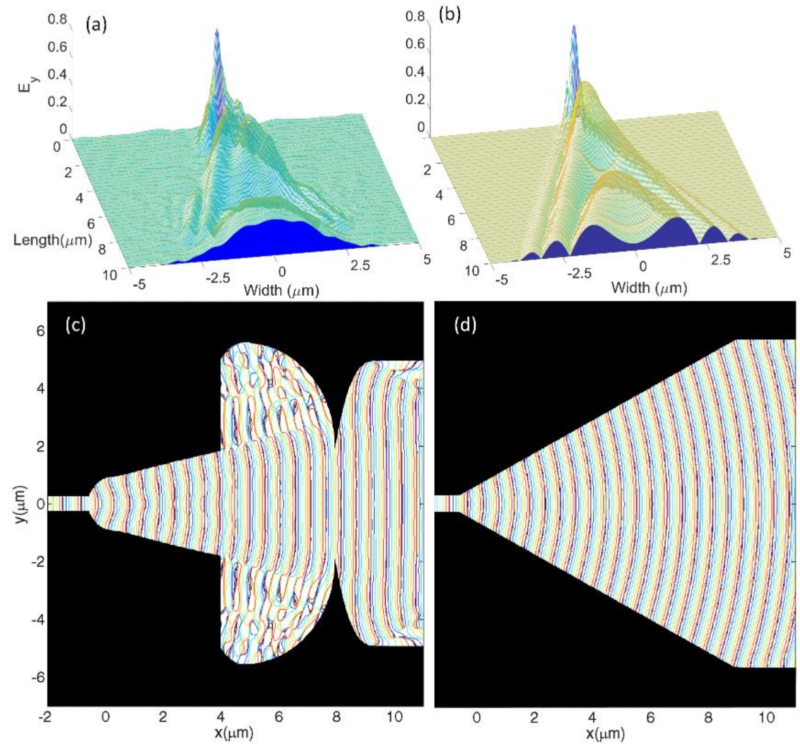

Fig. 4.11. Electric field intensity profile for (a) the designed BE compared with (b) linear taper, Electric field phase profile for (c) the designed BE compared with (d) linear taper.

performance. The sub-lens structure can be defined through relation (4.3) by setting proper width and curvature values.

Another critical feature of the structure that emerges unexpectedly from optimization is the abrupt change of the width at segment 3, which practically breaks the width continuity. Before this segment, the structure looks like an adiabatic taper, afterwards it enters a totally different regime. To understand why such an abrupt change shows up, we study how the BE performance changes with the width (w_3) and curvature (m_3) of the segment as shown in Fig. 4.12(a). The variation of transmission is relatively slow for $w_3 > 4\mu m$ (peaked at the optimal value), which does not offer a clear clue of the abrupt width increase to 9μm. Interestingly, if we look at the trend for the next

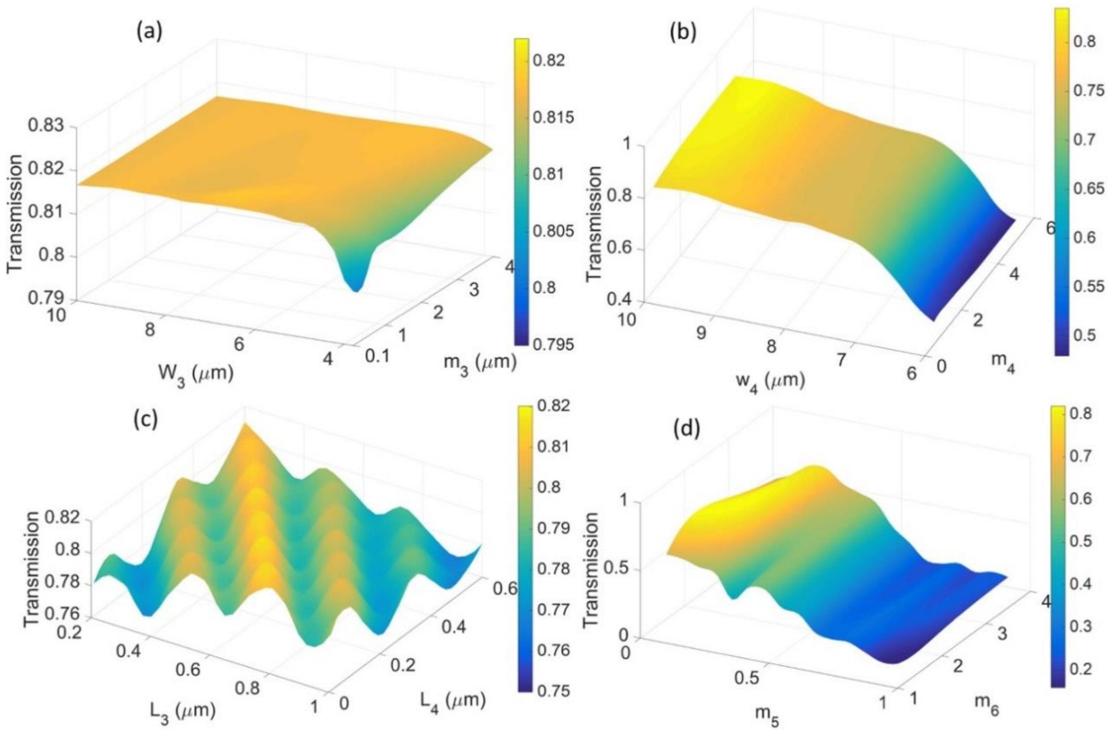

Fig. 4.12. BE performance by variation of BE performance with structure parameters

(a) (w_3, m_3); (b) (w_4, m_4); (c) (L_3, L_4); (d) (m_5, m_6).

segment shown in Fig. 4.12(b), the transmission shows a much steeper increase as the width w_4 increases. This seems to suggest that although the abrupt width apparently emerges at segment 3, explanation of its effect has to take segment 4 into account as well. Furthermore, looking at the optimal BE shape, the abrupt change of width changes at segment 3 requires both a sudden increase of w_3 and a very short L_3. Considering the potential correlation between segment 3 and segment 4 revealed in Fig. 4.12(a) and (b), we simulate the transmission variation with both L_3 and L_4 in Fig. 4.12(c). Clearly, along the line L_3+L_4=constant, the variation of transmission is quite small. Normal to this line, the transmission drops evidently. Combining Fig. 4.12(a)-(c), the emergence of the abrupt increase of width at segment 3 can now be understood: generally, there is a need for the non-adiabatic transition from the adiabatic taper part (segment 1 and 2) to the lensing part (segment 5 and 6). This non-adiabatic transition requires a short length and large width change. In the optimal design, this non-adiabatic transition is completed through collaborating effort of two segments (segment 3 and 4). It is possible to slightly increase L_3 and decrease L_4 and the transmission will degrade somewhat, but not substantially. The optimization result suggests that an adiabatic taper is inherently incapable of expanding the beam in less than 10μm length, the emergence of at least one non-adiabatic segment is inevitable. Segments 3 and 4 together allow the beam to freely propagate and expand to attain a large lateral width beyond the capability of adiabatic tapers.

Finally, the semi-lens segments help to flatten the wavefront to match to the output waveguide mode. The dependence of the transmission on the curvature m5 and m6 are shown in Fig. 4.12(d). Note that for structure compactness, the width of all segments is constrained to no greater than 10μm in our optimization. In most parts, this constraint has no effect because the optimal width is far below 10mm. Even for the widest part w_4, Fig. 4.12(b) shows that the transmission almost saturates for $w_4 > 8$μm.

To investigate the coupling of different modes, mode propagation based on the scattering matrix technique [105] is employed. The fundamental TE mode (TE_0) is used as the input, we consider coupling to the first four higher order even modes (TE_2, TE_4, TE_6 and TE_8), and ignore the higher order even modes as their coupling ratios are negligible. Because of the symmetry, the overlap integrals between fundamental TE_0 and odd TE modes are zero.

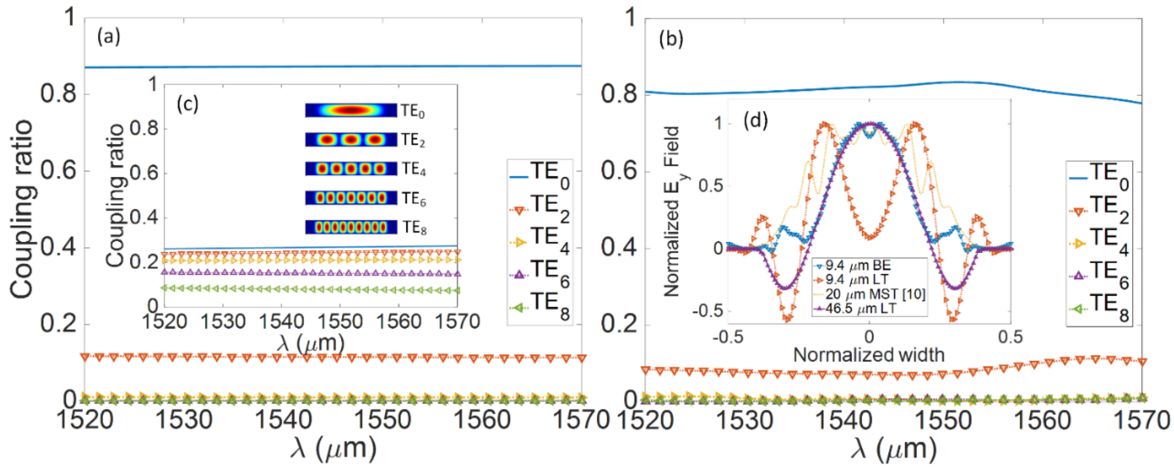

Fig. 4.13. Coupling ratio of five different modes in the output waveguide, for different cases: (a) $30\lambda_0$ linear taper, (b) $6\lambda_0$ BE and (c) $6\lambda_0$ linear taper. (d) shows electric field profile at the output waveguide for different cases. Inset of (c): the 2D mode profile of different modes.

Three different structures are considered. First, a $30\lambda_0$ long linear taper [Fig. 4.13(a)], in which light is mostly confined in the fundamental mode, less than 10% coupled to the TE_2 mode and a relatively negligible portion is coupled to all the other modes. The second structure is a $6\lambda_0$ long BE [Fig. 4.13(b)] with a comparable performance to $30l_0$ long linear taper. Finally, the third structure is a $6\lambda_0$ long linear taper [Fig. 4.13(c)], with a very low coupling to the fundamental mode. Figure 4.13(d) displays the electric field as a function of the lateral coordinate at the output end for the three aforementioned structures. Qualitatively, the power coupled to each mode is directly related to the overlap integral. Thus, more overlap to the output fundamental mode can increase the overall coupling efficiency [119]. For the BE, the back-reflection is calculated below -26 dB by the scattering matrix method. Back-reflection play insignificant role in BE insertion loss, for BE the back-reflection is below -26 dB and in a linear taper of the same length back-reflection is below -40 dB.

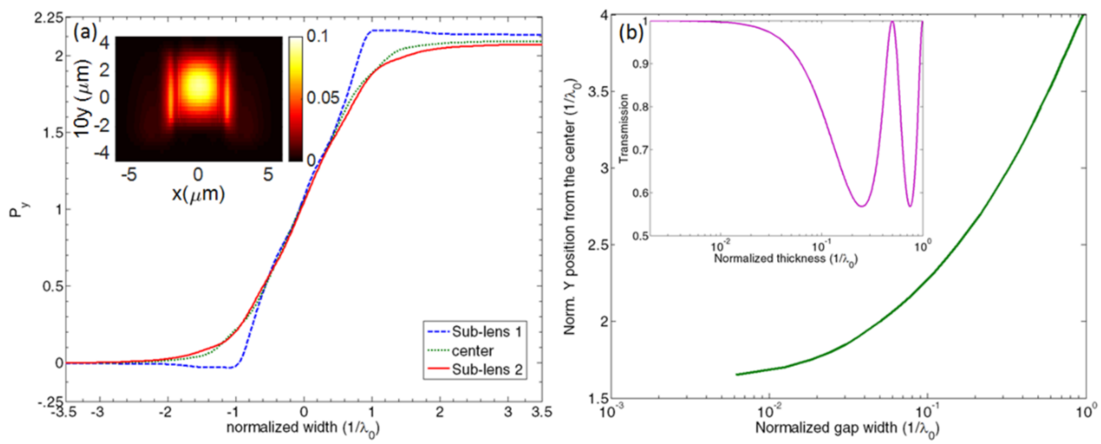

Fig. 4.14. (a) poynting vector integral in vertical direction for three different points in the sub-lens structure, The Electric field at the center is shown in the inset., (b) the gap spacing profile between the two sub-lenses from at the center point. The tranmission of the thin film for different gap spacing is calculated and shown in the inset.

In fast varying sidewall tapers, the dramatic wavefront deformation does not allow the use of the Fresnel or paraxial approximations–leading to the mode coupling theory in attempt to explain the observed phenomenon. Instead, the Rayliegh-Sommerfield diffraction formula or fully vectorial Maxwell equations with no approximation need to be solved.

Instead, of solving the Rayliegh-Sommerfield diffraction formula we loooking into Poynting vector integral and power distribution from the vertical direction of the sub-lens to gain some insight. Based on the calculations in the semi-lens structure [Fig. 4.14 (a)], most of the power is focused in approximately $2.2\lambda_0$ of the sub-lens width consistent with different positions of the semi-lens. The gap between two sub-lenses is shown in Fig. 4 .14(b). At the $2.2\lambda_0$ value, the gap width is below $0.1\lambda_0$, which corresponds to approximately 80% transmission based on the calculated thin film transmission for different width shown in the inset of Fig. 4.14 (b). Therefore, we can conclude that even at the smallest gap width of the semi-lens located in the center, approximately 80% of light is transferred to the second sub-lens. The electric field profile at the center of two sub-lens is displayed in the inset of Fig. 4.14(a). Moreover, the difference between the pointing vector integral values at different positions of the semi-lens [Fig. 4.14 (a)], shows some light leakage at the air-gap which has negligible effect on the mode transmission.

4.4 Measurement results and analysis of designed BE

The transmission is measured by coupling TE-polarized light from an HP 8168F tunable laser via a single-mode polarization maintaining fiber array into sub-wavelength grating couplers that deliver light into the in-plane silicon waveguide structures. The scanning electron microscope image of the device is depicted in Fig. 4.15(b). The transmission at each wavelength is recorded

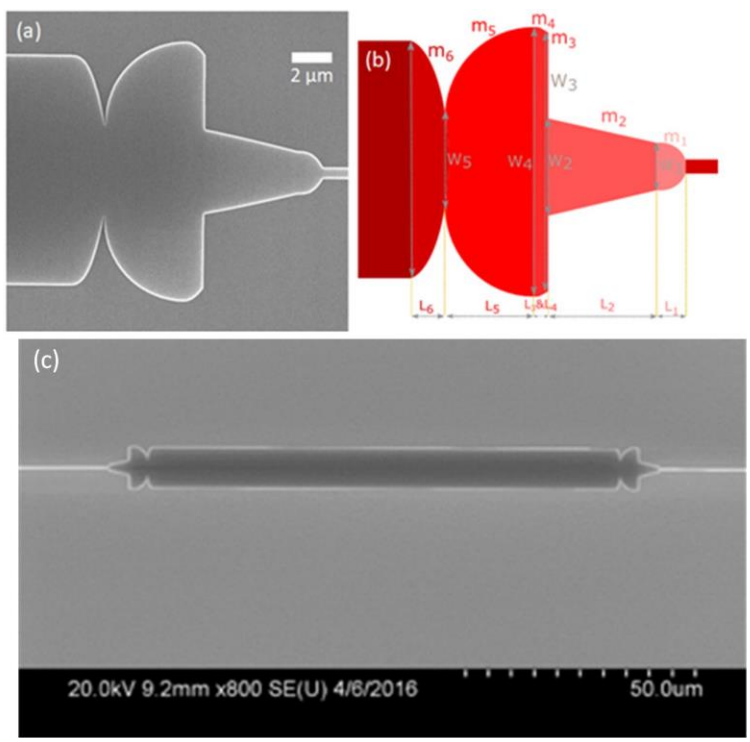

Fig. 4.15. (a) Scanning electron micrographs of beam expander and (b) schematic of different segments (c) Two grating coupler connected with 100 µm wide waveguide

via an HP 8153 photo-detector. The normalized transmission spectra are displayed in Fig 4.16. We use a reference waveguide without BEs to cancel out all the coupling and waveguide loss effects. The average insertion loss measurements for multiple BEs are shown in Fig. 4.17(a). The results for the linear tapers of the same length are shown in Fig. 4.17(b) for comparison According to the measured results, the BE has -0.85 dB and the corresponding linear taper has -4.2 dB insertion loss on average over 50nm bandwidth.

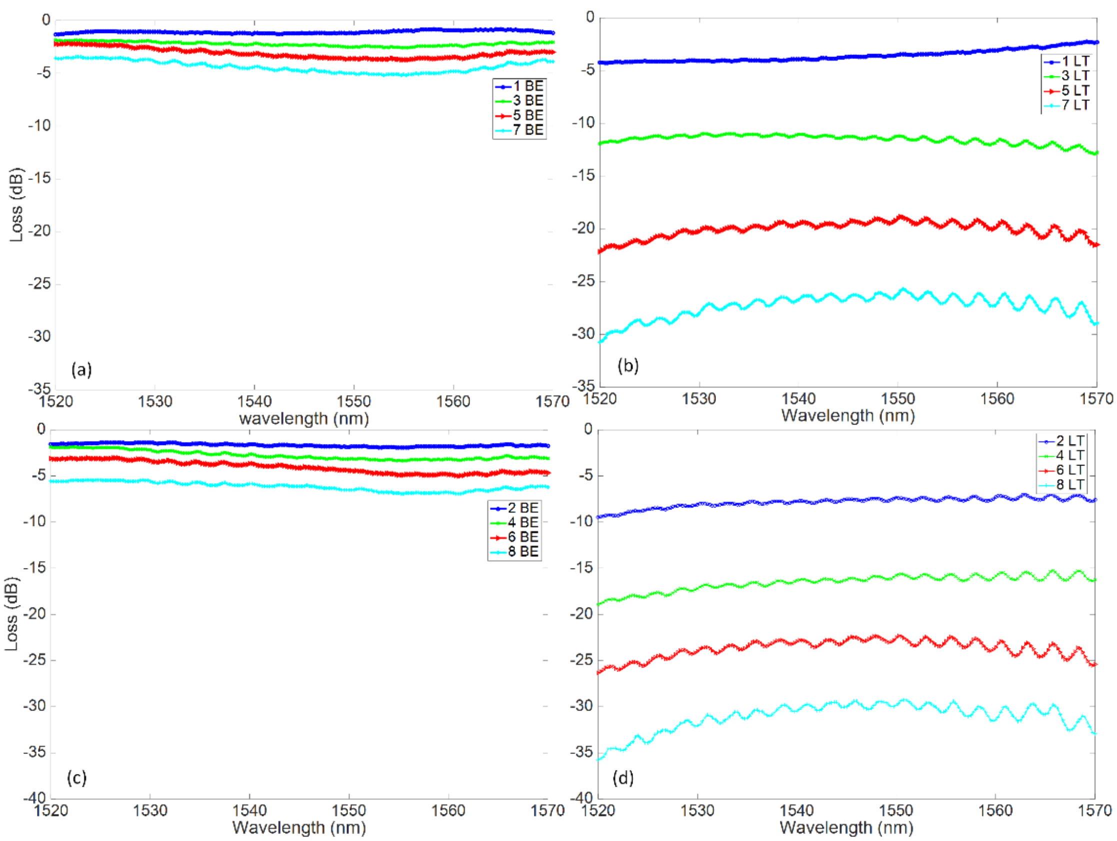

Fig. 4.16. Normalized Transmission spectra measured for (a) Evev number of BE (b) Even number of LT,(c) Odd number of BE and (d) Odd number of LT devices.

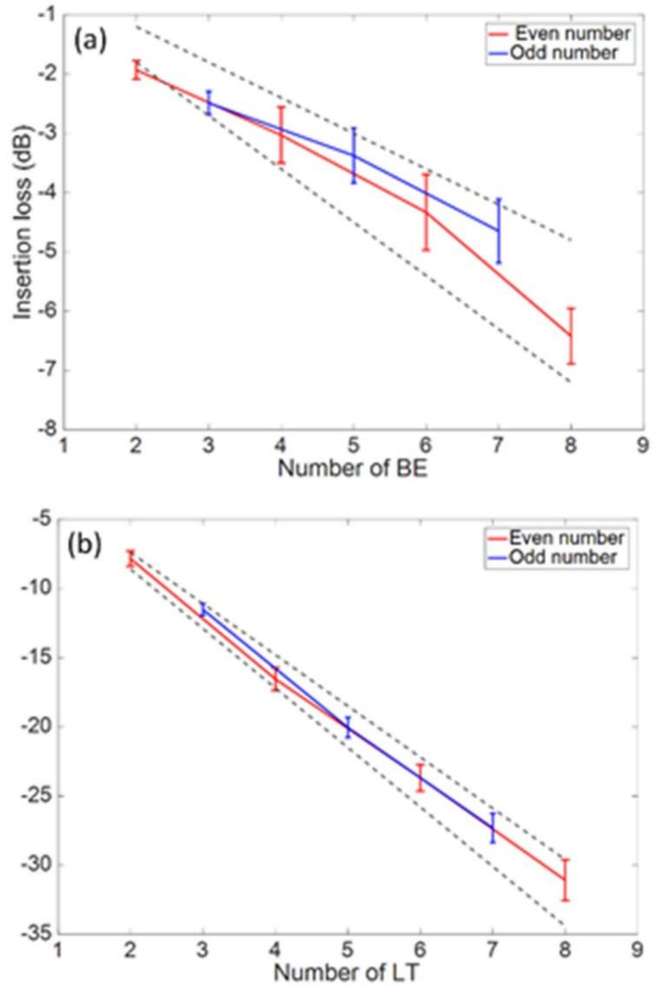

Fig. 4.17. Experimental measurements showing average insertion loss and error bars over a 50 nm bandwidth in (a) the BE in which the dotted limit lines showing 0.6 and o.9 dB limits and (b) linear taper the dotted limit lines showing 3.7 and 4.3 dB limits

The BE structure is fabricated on an SOI wafer with a 2 µm buried oxide layer and a 260 nm top silicon layer. It is patterned employing a JEOL JBX-6300FS high-resolution e-beam lithography system operating at 100 keV on a 120-nm-thick XR-1541-006 hydrogen-silsesquioxane (HSQ) negative e-beam resist. The pattern is transferred to the silicon layer via an Oxford Plasmalab 100 ICP etcher, using an $HBr+Cl_2$ based chemistry for vertical and smooth sidewalls. To compare the

Table 4.2. Normalized Expansion ratio (NER) comparison for different mode size converters.

BE design	Length (μm)	NER	Ref
segmented-stepwise MSC	20	1.71	[99]
Horizontal SSC	60	0.89	[98]
Irregular mode converters	20	1.89	[100]
Lens assisted	20	1.53	[102]
Adiabatic taper	120	0.30	[106]
Linear Taper	9.5	1.24	Measurement
BE	9.5	2.8	Measurement

performance of the BE with the linear taper and other designs, we introduce a normalized expansion ratio (NER) as a Figure of merit, considering the length of taper, both waveguide widths, and the transmission. An ideal BE delivers most of the optical power in the shortest length between two waveguides with large width difference. This Fig. of merit is defined in (2), where W_{out}/W_{in} is the output over input waveguide width ratio, L_{Taper}/λ_0 is the normalized BE length to the center transmission wavelength and T_{avg} is the average transmission in a linear scale. The NER is calculated for, horizontal spot size converter [98], segmented stepwise mode size converters [99], irregular mode converter [100], lens assisted spot size converter [102], 120 μm length adiabatic taper [106], 9.5 μm linear taper, and the designed BE and displayed in Table II. The NER merit for BE is more than 9 times greater than adiabatic taper.

$$NER = \frac{W_{out}/W_{in}}{L_{Taper}/\lambda_0}.T_{avg} \tag{4.4}$$

4.5 Conclusion

We show that mode-order-preserving waveguide expansion can be achieved through a composite adiabatic and non-adiabatic structure in an extremely short length comparable to the final width. We aim to design an adiabatic mode-width expansion structure. The structure consists of multiple segments; each following a power-law width profile, and the width is required to be continuous at the interfaces between segments. Then we search for an optimal structure with the lowest loss in a large design space using an advanced optimization algorithm. Surprisingly, the optimized structure practically breaks the width-continuity condition. It produces a composite structure mixed with adiabatic and non-adiabatic segments.

Chapter 5. Conclusions and suggestions for future work

5.1 Conclusions

Si photonics can play promising role in short range interconnects applications, because of its potential for low power, low cost and high volume manufacturing capability and ease of integration with CMOS electronic circuits. Also, the demand for more power efficient, compact devices is endless which fuel lots of research efforts to realize such devices in which, the nanobeam photonic crystals, grating coupler and mode converters are among those attractive devices.

In this dissertation, we have designed a fully etched grating coupler, as a mode coupling device from optical fiber to silicon chip. The designed subwavelength grating structure has been experimentally tested with our proposed surface measurement setup. The grating coupler enables coupling TE mode light from the surface with 45 nm bandwidth around c-band communication wavelength with measured insertion loss of around 3 dB per grating. The second part of the thesis is dedicated to a new design for high contrast mode filter on dual nanobeam photonic crystal platform. We have shown through numerical simulations and experimental measurements a high purity symmetrical mode filter. The proposed structure is capable of the control of excitation symmetry modes for even an odd TE mode in DNB resonator structures utilizing mode symmetry transforming MZCs. The designed DNB allow us to selectively excite the odd mode with a contrast >27 dB over the background modes separately into even, odd, or a mixture of the two modes. The third part of the thesis is dedicated to designing an ultra-compact mode converter device by direct curvature control in a segmented beam expander. Numerical optimization is used to explore novel design possibilities for nonadiabatic beam expanders. Assisted by the particle swarm optimization algorithm, we search for an optimal curvature-controlled multi-segment taper that maintains width continuity. Through spatial phase and parametrized analysis, a semi-lens feature is revealed that helps to flatten the wavefront at the output end to achieve -0.85 dB coupling efficiency for entire c-band wavelength.

5.2 Suggestions for future work

Fully etched grating coupler bandwidth can be increased by utilizing apodized gratings in the development of efficient mode coupler devices. The same procedure can be applied to design fully etched grating coupler for TM mode operation even though the GC device is optimized to couple TE mode. The footprint of the device can be reduced by designing an efficient, short mode converter. The surface coupling setup that has been developed to characterize our devices have the potential to be fully automated, which will potentially reduce the characterization time.

High purity modes in single mode cavity of DNBs and moderate Q-factors make this device an interesting platform for implementing all optical devices utilizing the Kerr effect in mixed mode configuration. Through this, the pump and probe signals can excite each mode in DNB and interact in the cavity region for modulation purposes. This device can be applied as an electro-optic modulator for further development if a graphene layer is patterned at the cavity region as the absorber layer that can be controlled electronically. For using this in sensing application, then DNB high purity mode filter in the mixed mode scheme can be operated as a novel optical sensing device in which the sensing and manipulating of nanoparticles passing through the microfluidic channel can be done concurrently if a microfluidic channel is incorporated on top of the nanobeam.

The compact BE that has been developed in planar silicon can be implemented with any transparent material at c-band such as InP and SiN. The idea of wavefront curvature control can be utilized to construct high performance mode couplers in plasmonic structures. The BE device can be optimized in such a way that the input light is coupled to higher order modes instead of fundamental mode, this can be useful for certain applications such as mode division multiplexing. As a design constraint, the thickness of Si waveguide was kept constant; by adding the shallow etch capabilities and having greater design space, more efficient BEs can be implemented.

Bibliography

[1] Cisco "The zettabyte era: Trends and analysis", white paper, (2016).

[2] A. Biberman and K. Bergman, "Optical interconnection networks for high-performance computing systems," Rep Prog Phys. 75(4):046402, (2012).

[3] L. W. Luo, N. Ophir, C. P. Chen, L. H. Gabrielli, C. B. Poitras, K. Bergman, M. Lipson, "WDM-compatible mode-division multiplexing on a silicon chip, " Nat. Commun. 5, 3069, (2014).

[4] J. S. Orcutt, A. Khilo, C. W. Holzwarth, M. A. Popović, H. Li, J. Sun, T. Bonifield, "Nanophotonic integration in state-of-the-art CMOS foundries, " Optics Express 19 2335-2346, (2011).

[5] D. Miller, "Device requirements for optical interconnects to silicon chips, " Proc. IEEE, vol. 97, no. 7, pp. 1166–1185, (2009).

[6] D.A.B. Miller, H.M. Ozaktas, "Limit to the Bit-Rate Capacity of Electrical Interconnects from the Aspect Ratio of the System Architecture, " Journal of Parallel and Distributed Computing, Vol. 41, Issue 1, 25, (1997).

[7] L. Kimerling, "Silicon Microphotonics: High Volume Manufacturing," Advanced Photonics 2015, OSA Technical Digest OSA, paper IT1A.3, (2015).

[8] D. Thomson and A. Zilkie and J. E Bowers and T. Komljenovic and G. T Reed and L. Vivien and De. Marris-Morini and E. Cassan and L. Virot and J.-M. Fédéli and J.-M. Hartmann and J. H Schmid and D.-X. Xu and F. Boeuf and P. O'Brien and G. Z Mashanovich and M. Nedeljkovic, "Roadmap on Silicon photonics" SP- 073003, Journal of Optics, Vol- 18, Is.- 7, (2016).

[9] J. Miller, J. Psota, G. Kurian, N. Beckmann, J. Eastep, J. Liu, M. Beals, J. Michel, L. Kimberling, and A. Agarwal "ATAC: A manycore processor with on-chip optical network, " Massachusetts Institute of Technology, Cambridge, MA, USA, MIT-CSAIL-TR-2009–018, (2009).

[10] K. Yamada, T. Tsuchizawa, H. Nishi, R. Kou, T. Hiraki, K. Takeda, H. Fukuda, Y. Ishikawa and K. Wada, T. Yamamoto, "High-performance silicon photonics technology for telecommunications applications, " Science and Technology of Advanced Materials, Vol 15, No. 2, (2014).

[11] E. Agrell, M. Karlsson, A R Chraplyvy, D. J Richardson, P. M Krummrich, P. Winzer, K. Roberts, J. Karl Fischer, Seb J Savory, B. J Eggleton, M. Secondini, F. R Kschischang, A. Lord, J. Prat, I. Tomkos and J. E Bowers, S. Srinivasan, M. Brandt-Pearce and N. Gisin, "Roadmap of optical communications, " Journal of Optics, Vol 18 sp. 063002, (2016).

[12] R. Soref and J Larenzo. "All-silicon active and passive guidedwave components for λ= 1.3 and 1.6 um, " Quantum Electronics, IEEE Journal of, 22(6):873-879, (1986).

[13] Y. Arakawa, T. Nakamura, Y. Urino and T. Fujita, "Silicon photonics for next generation system integration platform," in *IEEE Communications Magazine*, vol. 51, no. 3, pp. 72-77, (2013).

[14] C. J, Poitras, K. Preston, L. Chen and M. Lipson, "Low loss etchless silicon photonic waveguides, " Opt. Express 17 4752–7, (2009).

[15] S. Abaslou and V. Ahmadi, "Compact all-optical switch for WDM networks based on Raman effect in silicon nanowavegide," Opt. Lett. **37**, 40-42, (2012).

[16] J. E. Bowers, T. Komljenovic, M. Davenport, J. Hulme, A. Y. Liu, C. T. Santis, A. Spott, S. Srinivasan, E. J. Stanton, C. Zhang, "Recent advances in silicon photonic integrated circuits, " Proc. SPIE 9774, Next-Generation Optical Communication: Components, Sub-Systems, and Systems V, 977402, (2016).

[17] D. Kucharski, S. Abdalla, B. Analui, C. Bradbury, P. D. Dobbelaere, D. Foltz, S. Gloeckner, D. Guckenberger, M. Harrison, S. Jackson, M. Mack, G. Masini, A. Mekis, A. Narasimha, M. Peterson, T. Pinguet, S. Sahni, W. Wang, B. Welch, and J. Witzens, "40Gb/s optical active cable using monolithic transceivers implemented in silicon photonics enabled 0.13 um SOI CMOS technology, " Hot Chips, vol. 21, (2009).

[18] B. R. Koch, A. Alduino, L. Liao, R. Jones, M. Morse, B. Kim, W. Lo, J. Basak, H. Liu, H. Rong, M. Sysak, C. Krause, R. Saba, D. Lazar, L. Horwitz, R. Bar, S. Litski, A. Liu, K. Sullivan, O. Dosunmu, N. Na, T. Yin, F. Haubensack, I. Hsieh, J. Heck, R. Beatty, J. Bovington, and M. J. Paniccia, "A 4x12.5 Gbps CWDM Si Photonics Link using Integrated Hybrid Silicon Lasers," in *CLEO:2011 - Laser Applications to Photonic Applications*, OSA Technical Digest, (2011).

[19] F. E. Doany, B. G. Lee, A. V. Rylyakov, D. M. Kuchta, C. Jahnes, C. Baks, F. Libsch, C. L. Schow, "Terabit/sec 48-channel fiber-coupled optical module based on holey CMOS transceiver IC", Electronic Components and Technology Conference (ECTC) 2012 IEEE 62nd, pp. 1499-1504, (2012).

[20] C. R. Doerr, L. Chen, D. Vermeulen, T. Nielsen, S. Azemati, S. Stulz, G. McBrien, X. Xu, B. Mikkelsen, M. Givehchi, C. Rasmussen, and S. Y. Park, "Single-Chip Silicon Photonics 100-Gb/s Coherent Transceiver," in *Optical Fiber Communication Conference: Postdeadline Papers*, OSA, (2014).

[21] M. Lipson, "Guiding, modulating, and emitting light on silicon-challenges and opportunities," J. Light. Technol. 23 4222–38, (2005).

[22] B. G. Lee et al. "Ultrahigh-bandwidth silicon photonic nanowire waveguides for on-chip networks, " IEEE Photon. Technol. Lett. 20 398–400, (2008).

[23] Y. A. Vlasov and S. J. McNab, "Losses in single-mode silicon-on-insulator strip waveguides and bends," Opt. Express 12, 1622-1631, (2004).

[24] Xu F, Poon A W, "Silicon cross-connect filters using microring resonator coupled multimode-interference-based waveguide crossings, " Opt. Express 16 8649–57 (2008).

[25] R. Beausoleil et al, "A nanophotonic interconnect for high-performance many-core computation, " HOTI ’08: 16th IEEE Symp. on High Performance Interconnects, pp 182–9, (2008).

[26] A. Biberman, P. Dong, B G Lee, J D Foster, M Lipson and K Bergman, "Silicon microring resonator-based broadband comb switch for wavelength-parallel message routing" LEOS 2007: The 20th Annual Meeting of the IEEE Lasers and Electro-Optics Society pp 474–5, (2007).

[27] K. Yamada, H. Fukuda, T. Tsuchizawa, T. Watanabe, T. Shoji and S. Itabashi, "All-optical efficient wavelength conversion using silicon photonic wire waveguide," in IEEE Photonics Technology Letters, vol. 18, no. 9, pp. 1046-1048, (2006).

[28] J. N. Milgram, J. Wojcik, P. Mascher, and A. P. Knights, "Optically pumped Si nanocrystal emitter integrated with low loss silicon nitride waveguides, " Optics Express, vol. 15, pp. 14 679–14 688, (2007).

[29] Fang Q, Song J F, Tao S H, Yu M B, Lo G Q and Kwong D L, "Low loss (6.45 Db/cm) sub-micron polycrystalline silicon waveguide integrated with efficient waveguide coupler” Opt. Express 16 6425–32, (2008).

[30] S. Macnab, N. Moll an Y. Vlasov, "Ultra-low loss photonic integrated circuit with membrane type photonic crystal waveguides, " Optics Express, 11 22 pp. 2927-2939, (2003).

[31] W. S. Zaoui, A. Knuze, W. Vogel, "Bridging the gap between optical fibers and silicophotonic integrated circuits, " Optics Express, 22 2 pp. 1277-1286 (2014).
[32] R. Baets, "Off-chip beam steering with a one-dimensional optical phased array on silicon-on-insulator," Opt. Lett. 34, 1477-1479, (2009).
[33] A. Hajimiri, "Nanophotonic projection system," Opt. Express 23, 21012-21022 (2015) .
[34] H. Hashemi, "Monolithic optical phased-array transceiver in a standard SOI CMOS process," Opt. Express 23, 6509-6519, (2015).
[35] L. Chrostowski and M. Hochberg, *Silicon photonic Design*, Cambridge University Press, (2016).
[36] X. Xu, H. Subbaraman, J. Covey, D. Kwong, A. Hosseini, and R.T. Chen, "Complementary metal–oxide–semiconductor compatible high efficiency subwavelength grating couplers for silicon integrated photonics, " Appl. Phys. Lett. 101, 031109 (2012).
[37] X. Xu, H. Subbaraman, J. Covey, D. Kwong, A. Hosseini, and R.T. Chen, "Colorless grating couplers realized by interleaving dispersion engineered subwavelength structures," Opt. Lett. 38, 3588, (2013).
[38] X. Chen, C. Li, C.K.Y. Fung, S.M.G. Lo, and H.K. Tsang, "Apodized waveguide grating couplers for efficient coupling to optical fibers," Photonics Tech. Lett., IEEE 22 (15), 1156-1158 (2010).
[39] D. Taillaert, H. Chong, P. I. Borel, L. H. Frandsen, R. DeLa Rue, and R. Baets, "A compact two-dimensional grating coupler used as a polarization splitter," IEEE Photonics Technol. Lett. 15,1249–1251, (2003).
[40] S. M. Rytov, "Electromagnetic properties of a finely stratified medium," Sov. Phys. JETP 2, 466, (1956).
[41] R. Halir, P. Cheben, J. H. Schmid, R. Ma, D. Bedard, S. Janz, D.-X. Xu, A. Densmore, J. Lapointe, and Í. Molina-Fernández, "Continuously apodized fiber-to-chip surface grating coupler with refractive index engineered subwavelength structure," Opt. Lett. 35, 3243-3245 (2010).
[42] D. Taillaert, "Grating couplers for coupling between optical fibers and nanophotonic waveguides, " Jpn. J. Appl. Phys. 45, 6071-6077, (2006).
[43] W. Song, R. Gatdula, S. Abbaslou, M. Lu, A. Stein, W. Y.-C Lai, J. Provine, R. Fabian W. Pease, D. N. Christodoulides, W. Jiang, "High-Density Waveguide Superlattices with Low Crosstalk" Nat. Commun. 6, 7027, (2015).
[44] R. Gatdula, S. Abbaslou, and W. Jiang, "Silicon based waveguide-to-freespace coupler," IEEE Optical interconnects conference, (2015).
[45] Y. A. Vlasov, "Silicon CMOS-integrated nano-photonics for computer and data communications beyond 100G, Communications Magazine, " IEEE 50, s67-s72 (2012).
[46] B. Jalali and S. Fathpour, “Silicon photonics" Lightwave Technology, Journal of, 24(12):4600 4615, (2006).
[47] W. Bogaerts, P. De Heyn, T. Van Vaerenbergh, K. De Vos, S. Kumar Selvaraja, T. Claes, P. Dumon, P. Bienstman, D. Van Thourhout and R. Baets, "Silicon microring resonators" Laser & Photon. Rev., 6: 47–73 (2012).
[48] K. Padmaraju, K. Bergman, "Resolving the thermal challenges for silicon microring resonator devices," Nanophotonics (2013).
[49] M. Notomi, "Manipulating light with strongly modulated photonic crystals," Rep. Prog. Phys. 73, 096501, (2010).
[50] B.-S. Song, S. Noda, T. Asano, and Y. Akahane, "Ultra high Q photonic double heterostructure nanocavity," Nature Material, vol. 4, pp.207–210, (2005).
[51] M. W. Pruessner, T. H. Stievater, and W. S. Rabinovich, "Integrated waveguide Fabry-Perot microcavities with silicon/air Bragg mirrors," Opt. Lett. 32, 533-535, (2007).
[52] M. Soltani, S. Yegnanarayanan, A. Adibi, "Ultra-high Q planar silicon microdisk resonators for chip-scale silicon photonics," Opt. Express 15, 4694-4704, (2007).

[53] Q. Xu, B. Schmidt, J. Shakya, and M. Lipson, "Cascaded silicon microring modulators for WDM optical interconnection," Optics Express, Vol. 14, pp. 9431–9436, (2006).

[54] Judson D. Ryckman, and S.M. Weiss, "Low mode volume slotted photonic crystal single nanobeam cavity, " Applied Physics Letters, 101, 071104, (2012).

[55] R. Halir, P. J. Bock, P. Cheben, A. Ortega-Moñux, C. Alonso-Ramos, J.H. Schmid, J. Lapointe, D.X. Xu, J.G. Wangüemert-Pérez, I. Molina-Fernández and S. Janz, "Waveguide sub-wavelength structures: a review of principles and applications, " Laser & Photonics Reviews, 9: 25–49, (2015).

[56] Z. Han, X. Checoury, L.-Daniel Haret, and P. Boucaud, "High quality factor in a two-dimensional photonic crystal cavity on silicon-on-insulator," Opt. Lett. 36, 1749-1751, (2011).

[57] J. D. Joannopoulos, S. G. Johnson, J. N. Winn, and R. D. *Meade*, *Photonic Crystals: Molding the Flow of Light*, Princeton University Press, Princeton, NJ, (2011).

[58] Lumerical Solutions, Inc. http://www.lumerical.com/tcad-products/fdtd/

[59] Comsol Inc. https://www.comsol.com/

[60] P. R. Villeneuve, S. H. Fan, J. D. Joannopoulos, K. Y. Lim, G. S. Petrich, L. A. Kolodziejski, and R. Reif, "Air-bridge microcavities, " Applied Physics Letters, 67(2):167–169, (1995).

[61] J. S. Foresi, P. R. Villeneuve, J. Ferrera, E. R. Thoen, G. Steinmeyer, S. Fan, J. D. Joannopoulos, L. C. Kimerling, H. I. Smith, and E. P. Ippen. "Photonic-bandgap microcavities in optical waveguides, " Nature, 390(6656):143–145, (1997).

[62] P. B. Deotare, M. W. McCutcheon, I. W. Frank, M. Khan, and M. Loncar, "High quality factor photonic crystal nanobeam cavities, " Appl. Phys. Lett. 94 (12), 121106 (2009).

[63] P. Lalanne and J. P. Hugonin. “Bloch-wave engineering for high-q, small-v microcavities,”. IEEE Journal of Quantum Electronics, 39(11):1430–1438, (2003).

[64] P. B. Deotare, L.C. Kogos, I. Bulu and M. Lončar, "Photonic Crystal Nanobeam Cavities for Tunable Filter and Router Applications," IEEE J. Sel. Topics Quantum Electron., vol. 19, no. 2, pp. 3600210-3600210, (2013).

[65] Q. Quan, P. B. Deotare, and M. Loncar, "Photonic crystal nanobeam cavity strongly coupled to the feeding waveguide," Appl. Phy. Lett., no. 96, p. 203102, (2010).

[66] Y. Gong, B. Ellis, G. Shambat, T. Sarmiento, J. Harris, and J. Vuckovic, "Nanobeam photonic crystal cavity quantum dot laser," Opt. Exp., vol. 18, no. 9, pp. 8781-8789, (2010).

[67] G. Shambat, B. Ellis, J. Petykiewicz, M. A. Mayer, T. Sarmiento, J. Harris, E. E. Haller, and J. Vuckovic, "Nanobeam photonic crystal cavity light-emitting diodes," Appl. Phy. Lett., no. 99, p. 071105, (2011).

[68] S. Meister, H. Rhee, A. Al-Saadi, B. A. Franke, S. Kupijai, C. Theiss, L. Zimmermann, B. Tillack, H. H. Richter, H. Tian, D. Stolarek, T. Schneider, U. Woggon, and H. J. Eichler, "Matching p-i-n-junctions and optical modes enables fast and ultra-small silicon modulators," Opt. Exp., vol. 21, no.13, pp. 16210-16221, (2013).

[69] Q. Biao, Y. Ping, L. Yubo, J. Xiaoqing, Y. Mei, and Y. Jianyi, "Analysis of Electrooptic Modulator with 1-D Slotted Photonic Crystal Nanobeam Cavity," IEEE Photon. Technol. Lett., vol. 23, no.14, pp.992-994 (2011).

[70] D. Yang, P. Zhang, H. Tian, Y. Ji, and Q. Quan, "Ultrahigh-Q and Low-Mode-Volume Parabolic Radius-Modulated Single Photonic Crystal Slot Nanobeam Cavity for High-Sensitivity Refractive Index Sensing," IEEE Photon. J., vol. 7, no.5, pp.1-8, (2015).

[71] M. Belotti, M. Galli, D. Gerace, L. C. Andreani, G. Guizzetti, A. R. Md Zain, N. P. Johnson, M. Sorel, and R. M. De La Rue, "All-optical switching in silicon-on-insulator photonic wire nano-cavities," Opt. Exp., vol. 18, no. 2, pp. 1450-1461, (2010).

[72] M. Li, W. H. P. Pernice, and H. X. Tang, "Tunable bipolar optical interactions between guided lightwaves," Nature Photon., vol. 3, pp. 464-468, (2009).

[73] M. Eichenfield, R. Camacho, J. Chan, K. J. Vahala, and O. Painter, "A picogram- and nanometre-scale photonic- crystal optomechanical cavity," Nature 459, pp. 550–555, (2009).

[74] C. V. Poulton, X. Zeng, M. T. Wade and M. A. Popovic, "Channel add–drop filter based on dual photonic crystal cavities in push–pull mode," Opt. Lett. 40, 4206-4209, (2015).

[75] P. B. Deotare, I. Bulu, I. W. Frank, Q. Quan, Y. Zhang, R. Ilic and M. Loncar, "All optical reconfiguration of optomechanical filters," Nature Commun., Vol. 3, no. 846, (2012).

[76] I. W. Frank, P. B. Deotare, M. W. McCutcheon, and M. Lončar, "Programmable photonic crystal nanobeam cavities," Opt. Exp., vol. 18, no. 8, pp. 8705-8712, (2010).

[77] A. Rundquist, A. Majumdar, and J. Vuckovic, "Off-resonant coupling between a single quantum dot and a nanobeam photonic crystal cavity," Appl. Phys. Lett., vol. 99, no. 25, p. 251907, (2011).

[78] P. B. Deotare, M. W. McCutcheon, Ian W. Frank, M. Khan, and M. Lončar, "Coupled photonic crystal nanobeam cavities," Appl. Phy. Lett., 95, p. 031102, (2009).

[79] C.V. Poulton, Z. Xiaoge, M. T. Wade, J. M. Shainline, J. S. Orcutt, M. A. Popovic, "Photonic Crystal Microcavities in a Microelectronics 45-nm SOI CMOS Technology," IEEE Photon. Technol. Lett., vol. 27, no.6, pp.665-668, (2015).

[80] P.B. Deotare, M.W. McCutcheon, I.W. Frank, M. Khan, and M. Lončar, "Coupled photonic crystal nanobeam cavities," Appl. Phys. Lett., vol. 95, no. 3, p. 031102, (2009).

[81] J. Hendrickson, R. Soref, J. Sweet, and W. Buchwald, "Ultrasensitive silicon photonic-crystal nanobeam electro-optical modulator: Design and simulation," Opt. Exp., vol. 22, no. 3, pp. 3271-3283, (2014).

[82] X. Ge, Y. Shi, and S. He, "Ultra-compact channel drop filter based on photonic crystal nanobeam cavities utilizing a resonant tunneling effect," Opt. Lett., vol. 39, no. 24, pp. 6973-6976, (2014).

[83] W. Fegadolli, J. Oliveira, V. Almeida, and A. Scherer, "Compact and low power consumption tunable photonic crystal nanobeam cavity," Opt. Exp., vol. 21, no. 3, pp. 3861-3871, (2013).

[84] N. Vukovic, N. Healy, F. H. Suhailin, P. Mehta, T. D. Day, and J. V. Badding, A. C. Peacock, "Ultrafast optical control using the Kerr nonlinearity in hydrogenated amorphous silicon microcylindrical resonators," Sci. Rep., vol. 3, no. 2885, (2013).

[85] B. E. A. Saleh, M. C. Teich, Fundamentals of Photonics; Wiley-VCH (2007).

[86] J. Tan, M. Lu, A. Stein, and W. Jiang, "High-purity transmission of a slow light odd mode in a photonic crystal waveguide," Opt. Lett., vol. 37, no. 15, pp. 3189-3191, (2012).

[87] W. Song, R. A. Integlia, and W. Jiang, "Slow light loss due to roughness in photonic crystal waveguides: An analytic approach," Phy. Rev. B, vol. 82, no. 23, p. 235306, (2010).

[88] A. Milton, W.K. Burns, "Mode coupling in optical waveguide horns," IEEE J. Quantum Electron., vol.13, no.10, pp.828-835, (1977).

[89] T. Ye, Y. Fu, L. Qiao, and T. Chu, "Low-crosstalk Si arrayed waveguide grating with parabolic tapers," Opt. Express 22, 31899-31906 (2014).

[90] C. Sheng, R. Bekenstein, H. Liu, S. Zhu, M. Segev, "Wavefront shaping through emulated curved space in waveguide settings, " Nat. Commun. 7, 10747, (2016).

[91] V. R. Almeida, R. R. Panepucci, M. Lipson, "Nanotaper for compact mode conversion," Opt. Lett. 28, 1302-1304, (2003).

[92] T. Mizuno, T. Kitoh, M. Itoh, T. Saida, T. Shibata, Y. Hibino, "Optical spotsize converter using narrow laterally tapered waveguide for planar lightwave circuits," J. of Lightwave Technol., vol. 22, no.3, 833, (2004).

[93] Q. Fang, J. Song, X. Luo, M. Yu, G. Lo, Y. Liu, "Mode-size converter with high coupling efficiency and broad bandwidth," Opt. Exp. 19, 21588 (2011).

[94] H.T. Chen, K. J. Webb, "Silicon-on-insulator irregular waveguide mode converters," Opt. Lett. 31, 2145-2147, (2006).

[95] T. Nakamura, C.L Xu, X. Li, W.-P. Huang, "A spot-size transformer based on mode interference," IEEE Photonics Technol. Lett. 3 325, (1998).

[96] B. Luyssaert, P. Bienstman, P. Vandersteegen, P. Dumon, R. Baets, "Efficient Nonadiabatic Planar Waveguide Tapers," J. Lightwave Technol. 23 2462, (2005).

[97] B. Luyssaert, P. Vandersteegen, D. Taillaert, P. Dumon, W. Bogaerts, P. Bienstman, D. Van Thourhout, V. Wiaux, S. Beckx, R. Baets, "A compact photonic horizontal spot-size converter realized in silicon-on-insulator," IEEE Photonics Technol. Lett. 1 73, (2005).

[98] J. Zou, Y. Yu, Mengyuan Ye, L. Liu, S. Deng, X. Xu, X. Zhang, "Short and efficient mode-size converter designed by segmented-stepwise method," Opt. Lett. 39 6273, (2014).

[99] E. Khoo, A. Liu, J. Wu, "Nonuniform photonic crystal taper for high-efficiency mode coupling," Opt. Exp. 13, 7748, (2005).

[100] A. Oskooi, A. Mutapcic, S. Noda, J. D. Joannopoulos, S. P. Boyd, S. G. Johnson, "Robust optimization of adiabatic tapers for coupling to slow-light photonic-crystal waveguides," Opt. Exp 20, 21558-21575, (2012).

[101] K. Van Acoleyen, R. Baets, "Compact lens-assisted focusing tapers fabricated on silicon-on-insulator," in Proceedings of IEEE Conference on Group IV Photonics, pp. 157–159, (2011).

[102] P.-H. Tichit, S. N. Burokur, and A. de Lustrac, "Waveguide taper engineering using coordinate transformation technology," Opt. Express 18, 767-772, (2010).

[103] M.M. Spuhler, B.J. Offrein, Gian-Luca Bona, R. Germann, I. Massarek, D. Erni, "A very short planar silica spot-size converter using a nonperiodic segmented waveguide," J. Lightwave Technol. 9, pp.1680-1685, (1998).

[104] C. Wei, F. Groen, M. K. Smit, I. Moerman, P. Van Daele, R. Baets, "Integrated optical elliptic couplers: modeling, design, and applications," *J.* Lightwave Technol., vol. 15, no. 5, pp. 906-912, (1997).

[105] Y. Fu, T. Ye, W. Tang, T. Chu, "Efficient adiabatic silicon-on-insulator waveguide taper," Photon. Res. 2, A41-A44, (2014).

[106] Q. Wu, J. P. Turpin, D. H. Werner, "Integrated Photonic Systems Based on Transformation Optics Enabled Gradient Index Devices," Light Sci. Appl. 1, e38, (2012).

[107] A. Di Falco, S. C. Kehr, and U. Leonhardt, "Luneburg lens in silicon photonics," Opt. Express **19**, 5156-5162 (2011).

[108] A. L. Mikaelian, “Application of stratified medium for waves focusing,” Dokl. Akad Nauk SSSR 81, 569–571, (1951).

[109] M. I. Kotlyar, Y. R. Triandaphilov, A. A. Kovalev, V. A. Soifer, M. V. Kotlyar, and L. O'Faolain, "Photonic crystal lens for coupling two waveguides," Appl. Opt. **48**, 3722-3730, (2009).

[110] Q. Bai, "Analysis of Particle Swarm Optimization Algorithm," Computer and Information Science, vol. volume 3 No 1, (2010).

[111] Y. Zhang, S. Yang, A. E. Lim, G.Q. Lo, C. Galland, T. Baehr-Jones, M. Hochberg, "A compact and low loss Y-junction for submicron silicon waveguide," Opt. Exp. 21 1310, (2013).

[112] C. M. Lalau-Keraly, S. Bhargava, O. D. Miller, E. Yablonovitch, "Adjoint shape optimization applied to electromagnetic design," Opt. Exp. 21 21693, (2013).

[113] W. Winkler, R. Schilling, K. Danzmann, J. Mizuno, A. Rüdiger, K. A. Strain, "Light scattering described in the mode picture," Appl. Opt. 33, 7547-7550, (1994).

[114] J.-M. Verdiell, M. A. Newkirk, T. L. Koch, R. P. Gnall, U. Koren, B. I. Miller, L. L. Buhl, "Aspheric waveguide lenses for photonic integrated circuits," Appl. Phys. Lett., 62, 808–810, (1993).

[115] J. W. Goodman. *Introduction to Fourier Optics*. McGraw-Hill, New York, (1996).

[116] D. F. G. Gallagher, T. P. Felici, "Eigenmode expansion methods for simulation of optical propagation in Photonics- Pros and cons", in Proc. SPIE, 4987, 69–82, (2003).

[117] S. Johnson, P. Bienstman, M. Skorobogatiy, M. Ibanescu, E. Lidorikis, J. Joannopoulos, "Adiabatic theorem and continuous coupled mode theory for efficient taper transitions in photonic crystals," Phys. Rev. E 66 (066608), (2002).

[118] J. D. Love, W. Henry, W. Stewart, R. J. Black, S. Lacroix, F. Gonthier, "Tapered single-mode fibres and devices. I. Adiabaticity criteria," in *IEE Proceedings J - Optoelectronics*, 5, 343-354, (1991).

Appendix A

Device Fabrication Procedure on SOI platform

The fabrication procedure including time and temperature of reach step are listed in the table below this includes grating coupler, nanobeam photonic crystal and beam expander fabrications

Process Description	**Time**
(1) Begin with a Silicon-On-Insulator (SOI) wafer with a 260 nm device layer (Silicon) thickness.	[N/A]
(2) Clean the wafer using RCA process [34], [35]:	
- Acetone with sonication	[10 minutes]
- H_2SO_4+H_2O_2 (1:1)	[10 minutes]
- NH_4OH+H_2O_2+H_2O (1:1:5) in a water bath @ 80°C	[10 minutes]
- HCl+H_2O_2+H_2O (1:1:5) in a water bath @ 80°C	[10 minutes]
- 10% HF	[5 minutes]
- Deionized water (DIW) rinse and blow dry with N_2 gas	[N/A]
H_2SO_4 Sulfuric Acid H_2O_2 Hydrogen Peroxide NH_4OH Ammonium Hydroxide HF Hydrofluoric Acid HCl Hydrochloric Acid	
(3) Spin XR-1541-006 (HSQ) e-beam lithography resist:	
- Dehydration bake on a hotplate @ 150°C	[10 minutes]
- Spin HSQ @ 4000 RPM	[60 seconds]
- Softbake on a hotplate @ 80°C	[4 minutes]

(4) Expose with e-beam lithography: - Base dose range: 5000 $\frac{\mu C}{cm^2}$ to 8000 $\frac{\mu C}{cm^2}$ - $t_{expose} \approx \frac{Area^2 \times Dose}{Current}$	[t_{expose}]
(5) Develop and clean: - NaOH+NaCl+DIW (1:4:95 %wt) - DIW rinse - Acetone - Isopropyl alcohol (IPA) - DIW rinse and blow dry with N_2 gas	 [4 minutes] [5 minutes] [5 minutes] [5 minutes] [N/A]
(6) Etch with ICP etcher: - HBr + Cl based recipe @ 20°C - High anisotropy and smooth sidewalls - Selectivity of Si:SiO_2 is approximately 50:1 (Note that cured HSQ has similar properties to SiO_2) - $t_{etch} = etch\,rate \times 260nm$	[t_{etch}]
(7) Spin and thermally cure HSQ for thin cladding and planarization (2 coatings): - Spin HSQ at 4000 RPM - Bake on a hotplate @ 90°C - Bake on a hotplate @ 150°C - Bake on a hotplate @ 225°C - Bake on a hotplate @ 400°C - Repeat spinning and baking for 2nd coating - Bake on a hotplate @ 400°C	 [45 seconds] [2 minutes] [2 minutes] [2 minutes] [10 minutes] [16 min. 45 sec.] [10 minutes]
(8) Final cladding with PECVD SiO_2: - Low flow deposition @ 400°C - $t_{dep} = dep.rate \times 200nm$	[t_{dep}]

As the photonic crystal are suspended a separate undercut process is required

DNB BOX layer undercut process

(1) Clean with Acetone Clean with IPA Clean with DI water	[5 min.] [5 min.] [5 min.]
(2) Spin "Az 5214-E" -Dehydration bake @110 C -Spin @ 4 Krpm -Soft-bake @110 C	[5 min.] [40 sec.] [1min]
(3) Optical Lithography Process	Time : 20 sec
(4) Develop in "AZ327-MIF" Rinse in DI water	[45 sec.]
(5) Hard bake @ 150 C	[2 min]
(6) Undercut BOX layer with BOE (30:1) Rinse in DIW twice	[10 min]
(7) Strip photoresist -Piranha etch [H2So4+H2O2(1:1)] Rinse in DIW twice O2 plasma IPC machine clean W barrel etch Pirhana etch Rinse in DIW twice	 [10 min] [10 min] [10 min]

Appendix B

Adiabatic taper length calculation

Among different adiabatic taper profiles parabola is the most efficient. It has been proven through assisting light ray model by Burns [89]. In this appendix we will tend to derive relation 2.3 by considering three assumptions: A light ray model, an eigenmode expansion model with forward mode beating and a Gaussian beam model are applied which enable us to simplify the calculations.

Based on the ray model and take a random section in parabolic taper with width w, shown in Fig. B.1. The ground mode of a straight waveguide with this width can be written as:

$$\psi(x,z) = \cos(\mathrm{k}_x \mathrm{x}) \times \exp(-j\beta\,\mathrm{z}) \qquad \text{(B.1)}$$

assuming hard waveguide boundary conditions, the electric field in the cladding boundary become zero. Using the relations: cos(α) = cosh(jα) and $k_x^2 + \beta^2 = k^2$ this formula can be rewritten as:

$$\psi(x,z) = \frac{1}{2} \times \left(\exp\left[-j(\cos\theta.\mathrm{z} + \sin\theta.\mathrm{x}\right] + \exp(-\mathrm{j}(\cos\theta.\mathrm{z} - \sin\theta.\mathrm{x})) \right) \qquad \text{(B.2)}$$

with $\cos\theta = \beta / k$ and $\sin\theta = k_x / k$.

This way one can think of a waveguide mode as a spatially distributed sum of rays propagating at angles θ and $-\theta$ with respect to the propagation axis which we will call

θ_m. Assume now that a taper will be adiabatic if the local modal angle is bigger than the local taper angle, or $\theta_m > \theta$. Again using the hard boundary condition approximation, the wave vector of the ground mode becomes:

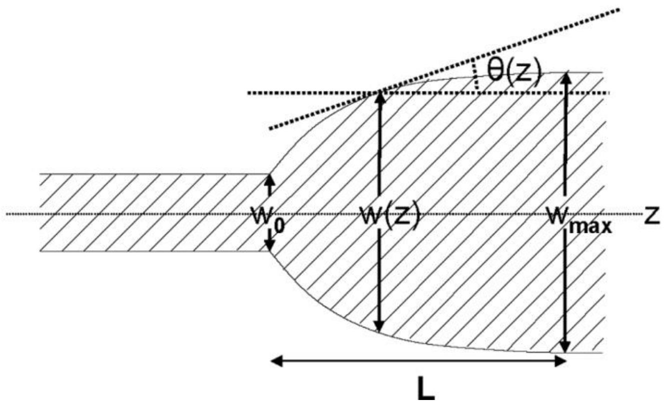

Fig. B.1. A schematic parabolic taper with defined local angle

$k_{x,0} = \frac{\pi}{\omega}$ and for waveguides with w >> λ the mode angle can be approximately:

$$\theta_m \approx \sin\theta_m = \frac{k_{x,0}}{k} = \frac{\lambda}{2\omega n_{core}} \tag{B.3}$$

So the adiabatic condition becomes:

$$\theta = \frac{\alpha_1 \lambda}{2\omega n_{core}} \tag{B.4}$$

In which α_1 a constant smaller than or equal to unity.

The next approximate we are going to make is that the local taper mode by a Gaussian beam with full ($1/e^2$) beam width of w/2 [117]. Considering this assumption, a taper is adiabatic if the divergence angle of the local Gaussian beam is bigger than the local taper angle, or $\theta_g > \theta$. The (half) divergence angle of a Gaussian beam with (half) waist d_0 can be written as [118]:

$$\theta_g = \frac{2}{k.d_0} = \frac{4\lambda}{\pi.\mathrm{n}_{core}.w} \tag{B.5}$$

as $d_0 = w_0/4$. And $\theta < \theta_g$ The assumption now translates to: $\theta = \dfrac{\alpha_2 \lambda}{2wn_{core}}$

with α_2 smaller than or equal to $8/\pi$. Using eigenmode expansion, the adiabatic criterion can now be written as follows. A taper is adiabatic if the local taper length is bigger than the local coupling length between the ground and the first even mode. For this section, Fig. A.1 should be looked at from right to left, so as a taper between a broad and a narrow waveguide. This criterion is also known as Love's criterion [119]. The local taper length is defined as:

$$L_{local} = \frac{w/2}{\tan\theta} \approx \frac{w}{2\theta} \tag{B.6}$$

and the coupling between the two modes is:

$$L_{coupling} = \frac{\pi}{\beta_0 - \beta_2} \tag{B.7}$$

Again using the hard boundary condition approximation yields for the betas:

$$\beta_i = \sqrt{k^2 - k_{x,i}^2} \approx k(1 - \frac{1}{2}\frac{k_{x,i}^2}{k^2}) = \mathrm{k} - \frac{k_{x,i}^2}{2k} \tag{B.8}$$

$$k_{x,i} = \frac{(\mathrm{i}+1)\omega}{\pi} \tag{B.9}$$

$$\beta_0 - \beta_2 = \frac{\pi\lambda}{4n_{core}w^2}(3^2 - 1^2) = \frac{2\pi\lambda}{n_{core}w^2} \tag{B.10}$$

Using the above relations, the adiabatic criterion can be rewritten as:

$L_{local} > L_{coupling}$ we get the following relations:

$$\frac{w}{2\theta} > \frac{\pi}{\beta_0 - \beta_2} = \frac{n_{core}w^2}{2\lambda} \tag{B.11}$$

Then θ is $\theta = \dfrac{\alpha_3\lambda}{2wn_{core}}$ in with α_3 smaller than or equal to 2.

Minimum length for Parabolic taper profile

Equations B.5, B.10 and B.11 are identical except for the numerical values of α_1, α_2 and α_3. From Fig. B.1 the next relation is visibly clear:

$$\theta \approx \tan\theta = \frac{1}{2}\frac{dw}{dz}$$

(B.12)

which combines with equations B.5, B.11 and B.12 to:

$$\frac{dw}{dz} = \frac{\alpha\lambda}{w(z)n_{core}} \;\; Then \;\; w(z) = \sqrt{\frac{2\alpha\lambda}{n_{core}}z + Ct} \tag{B.13}$$

and with the right boundary condition $Ct = w_0^2$

From equation B.13 it can be inferred that the tangent line will be vertical if the width of the taper goes to zero, proving that the above parabola has the z-axis as symmetry axis. Setting z = L and w(z) = w_L in B.13 and isolating L leads to:

$$L = \frac{(w_L^2 - w_0^2).n_{core}}{2\alpha\lambda_0} \tag{B.14}$$

In which $\alpha \leq 1$ this is a very useful relation to estimate the minimum taper length needed for adiabatic operation. Inversely, using the length and the input and output width of an existing taper, one can calculate the adiabaticity parameter.